Neutron and X-Ray reflectometry on complex biological systems on solid surfaces

Philip-Harald Böhm

München 2018

NEUTRON AND X-RAY REFLECTOMETRY ON COMPLEX BIOLOGICAL SYSTEMS ON SOLID SURFACES

PHILIP-HARALD BÖHM

DISSERTATION

Fakultät für Physik
der
Ludwig-Maximilians-Universität

vorgelegt von
Philip-Harald Böhm
aus München

München, den 28. Mai 2018

ERSTGUTACHTER: PD Dr. Bert Nickel
ZWEITGUTACHTER: Prof. Jan Lipfert
TAG DER MÜNDLICHEN PRÜFUNG: 28. Juni 2018

2018
Gedenkjahr
75 Jahre

Weiße Rose

18. Februar. Sophie Scholl, 21 Jahre alt, und ihr Bruder Hans Scholl, 24 Jahre, werden in der Ludwig-Maximilians-Universität beim Verteilen des sechsten Flugblattes der Weißen Rose, entworfen von Professor Kurt Huber, entdeckt und von der Geheimen Staatspolizei verhaftet. FREIHEIT hatten sie mit weißer Farbe an die Wände geschrieben, mit unendlichem Mut trotz Ausgangssperre Parolen an Gebäuden in der Ludwigstraße, am Marienplatz und Viktualienmarkt angebracht, immer wieder gegen den Nationalsozialismus und Imperialismus aufgerufen. Zusammen mit Christoph Probst, 23 Jahre alt und Vater von drei Kindern, werden sie am 22. Februar wegen Vorbereitung zum Hochverrat und Feindbegünstigung zum Tode verurteilt. Am selben Tage werden die Freunde hingerichtet. Hans soll, bevor er starb, gerufen haben: Es lebe die Freiheit! In Sophies Zelle im Untersuchungsgefängnis findet ihre Mitgefangene Else Gebel auf der Rückseite der Anklageschrift mit Bleistift geschrieben: „Freiheit. Freiheit.“ Dieses Blatt gibt es noch. FREIHEIT. Freiheit.

Der Oberreichsanwalt
beim Volksgerichtshof

Berlin, den 21.Februar 1943

An die

Verwaltung des Hausgefängnisses der Geheimen
Staatspolizei, Staatspolizeileitstelle

München,
Briennerstr.50.

In der Anlage erhalten Sie Anklageschrift des Oberreichsanwalts beim Volksgerichtshof Berlin vom 22. Februar 1943 gegen Hans S c h o l l, Sophia S c h o l l und Christoph P r o b s t zur Zustellung an die Genannten durch den Urkundsbeamten der Geschäftsstelle des Oberlandesgerichts München, Justizinspektor Huber.

Die Angeschuldigten sind darauf hinzuweisen, dass sie bis Montag, den 22. Februar 1943, 8 Uhr vorm. Einwendungen gegen die Anordnung der Hauptverhandlung erheben und Beweisanträge stellen können.

Termin zur Hauptverhandlung ist für Montag, den 22. Februar ds. vorgesehen, 10 Uhr vorm.

I. V.
Weyersberg

An Angeschuldigte Sophia Scholl.

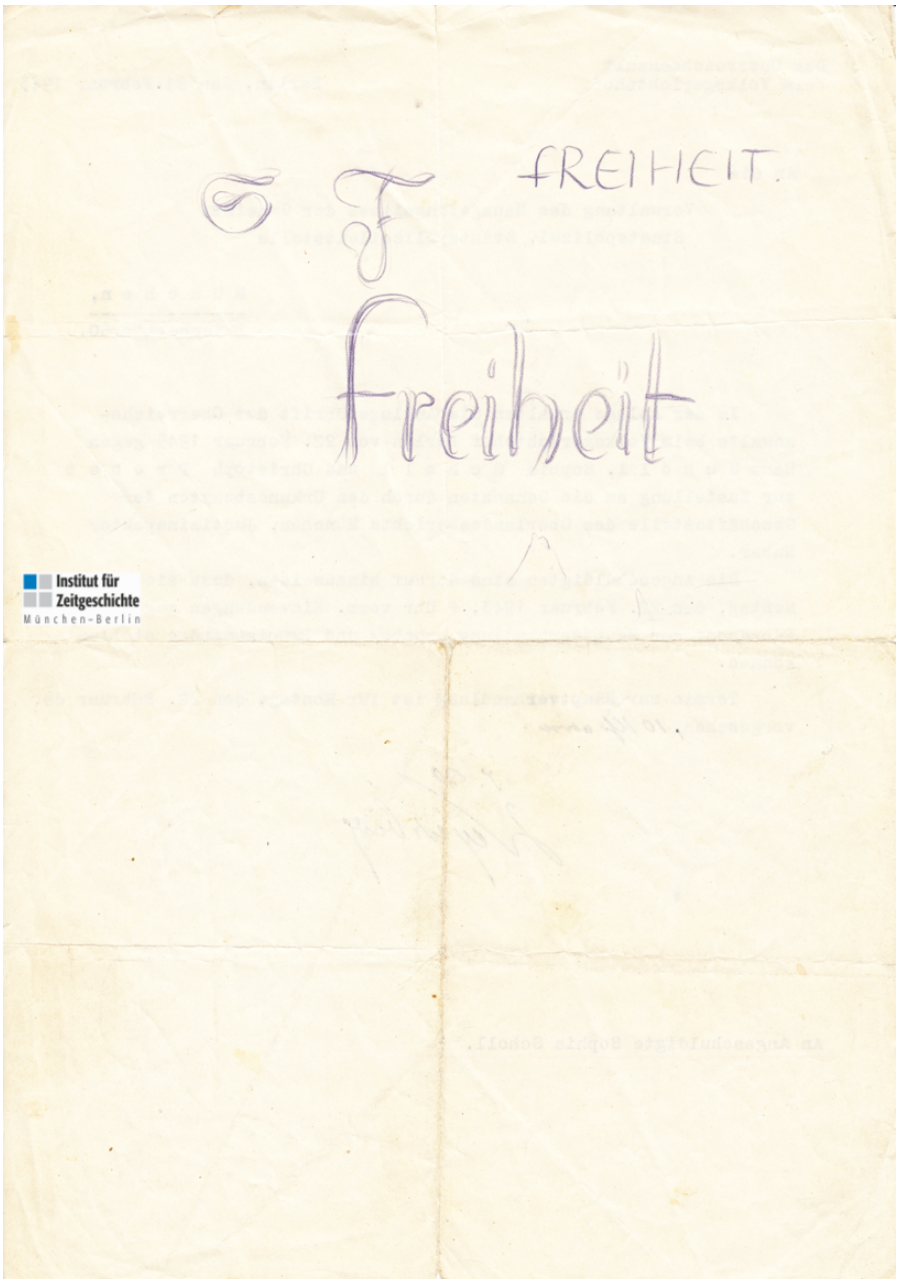

ZUSAMMENFASSUNG

Die Zellmembran ist ein einzigartiges Gebilde - es gibt in der Natur wohl keine größere, sich selbst anordnende Konstruktion aus Molekülen. Sie dient als Abgrenzung zur Außenwelt und ermöglicht einen kontrollierten Austausch mit dieser. Sie hat eine hohe Ordnung, ihre Bausteine sind zugleich in hohem Maße heterogen. Lipide sind die am häufigsten vorkommenden Bauteile in der Zellmembran. Die hydrophobe Wechselwirkung zwischen ihnen und der Umgebung ist der Hauptgrund für die Selbstanordnung. Die Zellmembran fungiert außerdem als Vermittler der Adhäsion. Die Zelladhäsion ist ein sehr komplexer Prozess. Dieser Prozess sowie die Struktur und die Funktionalität der Zellmembran sind Voraussetzungen für das Leben, wie wir es kennen. Ein tieferes Verständnis dieser ist von hoher biologischer und pharmazeutischer Relevanz. Im Rahmen der vorliegenden Arbeit wurde die Grenzfläche zwischen harten Substraten und Membranen mit Röntgen- und Neutronenreflektometrie analysiert.

Für zukünftige Anwendungen von Biosensoren, die auf Lipid-benetzten Feldeffekttransistoren basieren, welche in wässriger Lösung betrieben werden, ist die Bestimmung der Struktur, die Lipide auf Graphen bilden, eine Voraussetzung. An einem eigengefertigten Röntgenreflektometer mit einer Röntgenröhre mit Molybdänanode wurden Messungen an Lipid-benetztem Graphen durchgeführt. Das Reflektometer wurde umgebaut, um die sich ergebenden Anforderungen an Messdauer und Signal-Rausch-Verhältnis zu erfüllen. Es konnte gezeigt werden, dass sich eine Lipid-Einzellage der Dicke von etwa 20 Å ausbildet. Diese Beobachtung stimmt mit der Interpretation einer durchgeführten elektrischen Charakterisierung und Spreit-Experimenten überein. In weiteren Experimenten wurde gezeigt, dass Feldeffekttransistoren geeignet sind, das Ausbilden von Lipidlagen zu beobachten. Das Ausbilden der Lagen konnte in-situ in Echtzeit aufgelöst werden. Außerdem wurde der Einfluss von verschieden-geladenen Lipidschichten auf die Kennlinien des Transistors untersucht.

Die Zelladhäsion auf Siliziumsubstraten wurde mit Neutronen- und Röntgenreflektometrie untersucht. Die Neutronenreflektometriemessungen wurden am FRM II durchgeführt. Um die nötigen Bedingungen zu schaffen, die es ermöglichen, in vitro Messungen an Zellen durchzuführen, wurden Messkammern entwickelt. Sie erlauben es, Messungen unter sterilen und temperaturstabilen Bedingun-

gen durchzuführen, sowie den Austausch von Zellmedium. An Epithelzellen wurden Neutronenreflektometriemessungen in Medium mit verschiedenen Streukontrasten durchgeführt. Die Zellen adhärierten auf einem Siliziumsubstrat und bildeten einen konfluenten Zellrasen. Kontrastvariationen verringern die Mehrdeutigkeit in der Analyse der Neutronendaten. Die durchschnittliche Dicke und der durchschnittliche Grad der Hydrierung der Grenzfläche zwischen den Zellen und dem Substrat konnten bestimmt werden. Aus den Messergebnissen ergibt sich ein Drei-Schichten-Modell, das eine konsistente Interpretation aller Messungen erlaubt. Eine sehr dichte, 70 - 120 Å dicke Proteinschicht auf dem Silizium bildet die erste Schicht. Dieser folgt eine hydrierte, 180 - 280 Å dicke Lage. Die dritte, mehrere Hundert Å dicke Schicht kann der weniger hydrierten Verbundmembran zugeschrieben werden. Dieses Ergebnis stimmt mit der Theorie für Zelladhäsion mit immobilen Rezeptoren überein. Die Streudaten deuten darauf hin, dass die Proteinschicht auf dem Substrat als eine bioanaloge Schicht von den Zellen selber geformt wird. Um weitere Einblicke zu erhalten, wurden Röntgenreflektometriemessungen durchgeführt. Mit dem zur Verfügung stehenden eigengefertigten Röntgenreflektometer ergaben sich jedoch keine tieferen Einblicke in den Prozess der Zelladhäsion, was auf von den Röntgenstrahlen induzierte Strahlenschäden zurückgeführt wird. Es wurden jedoch Vorraussetzungen geschaffen, welche es erlauben, diesen Ansatz weiter zu verfolgen.

ABSTRACT

Cell adhesion is a fascinating albeit very complex process. It is mediated by the perhaps most abundant self-assembling molecular system in nature: the highly ordered, heterogeneous and immensely diverse cell membrane. Lipids are the main constituents of the cell membrane. The hydrophobic interactions between them and the surrounding are the main driving force for the self-assembly. The cell adhesion process and the structure and functionality of the cell membrane are a prerequisite for life. A deeper understanding is of high biological and pharmaceutical relevance. In the scope of this thesis, the interface between solid substrates and membranes was studied with X-ray and neutron reflectometry.

Resolving the lipid structure on graphene is a prerequisite for future applications of lipid decorated solution-gated graphene field-effect transistor based biosensors. X-ray reflectometry measurements on lipid coated graphene were performed on a custom-built molybdenum-anode-based in-house reflectometer. It was reconstructed during this thesis to meet the requirements regarding measurement time and signal-to-noise ratio. An around 20 Å thick lipid monolayer formation was revealed. The interpretation of the results from an electrical characterization of the lipid graphene interface and lipid spreading experiments correspond to the results of the reflectometry experiments. Solution-gated graphene field-effect transistors were applied to monitor the formation of lipid layers and to investigate the influence of differently charged lipid layers. In-situ monitoring of the formation of lipid layers in real time was demonstrated.

Cell adhesion on a silicon surface has been studied in neutron and X-ray reflectivity experiments. The neutron reflectometry experiments were conducted at FRM II. Sample chambers were developed, which provide the required sterile and temperature-stable sample environment for performing in-vitro reflectometry experiments on cell layers. Furthermore they allow for an exchange of the cell medium hence ensuring the necessary medium exchange for cell culturing and contrast variation. Neutron reflectivity experiments with confluent layers of epithelial cells adhering to silicon in cell medium with different scattering contrasts were performed. This contrast variation reduces the ambiguity of modelling the neutron data. The average thickness and degree of hydration of the interface between the adherent cells and the substrate were determined. A three-layered

interfacial organization is suggested, consisting of a very dense 70 - 120 Å thick protein film bound to the silicon surface interface, followed by a highly hydrated, 180 - 280 Å thick layer. The third, several hundred Å thick layer is attributed to the less hydrated composite membrane. This layer structure is in agreement with the theory of cellular adhesion and immobile receptors. It is further suggested that the bottom dense protein layer is formed by the cells to generate a bioanalogue tissue film. Additionally, X-ray reflectometry measurements were performed. The measurements did not provide more insight, what is attributed to beam damage in the sample. Nevertheless, the prerequisites for continuative measurements were created.

CONTENTS

ACRONYMS

CAM	cell adhesion molecule
CCD	charge-coupled device
CM0	cell medium dissolved in 0 % D_2O and 100 % H_2O
CM15	cell medium dissolved in 15 % D_2O and 85 % H_2O
CM30	cell medium dissolved in 30 % D_2O and 70 % H_2O
CM50	cell medium dissolved in 50 % D_2O and 50 % H_2O
CM75	cell medium dissolved in 75 % D_2O and 25 % H_2O
CM90	cell medium dissolved in 90 % D_2O and 10 % H_2O
CV	cyclic voltammetry
CNP	charge neutrality point
CVD	chemical vapor deposition
DLS	dynamic light scattering
DOTAP	1,2-dioleoyl-3-trimethylammonium-propane
DPTAP	1,2-dipalmitoyl-3-trimethylammonium-propane
ECM	extracellular matrix
EIS	electrochemical impedance spectroscopy
FLIC	fluorescence interference contrast microscopy
FRAP	fluorescence recovery after photobleaching
NR	neutron reflectometry
PBS	phosphate buffered saline
POPC	1-palmitoyl-2-oleoyl-sn-glycero-3-phosphocholine
POPG	1-palmitoyl-2-oleoyl-sn-glycero-3-phospho-(1'-rac-glycerol)
RICM	reflection interference contrast microscopy
SAIM	scanning angle interference microscopy
SAXS	small-angle X-ray scattering

SGFET	solution-gated field-effect transistor
SLB	supported lipid bilayer
SLD	scattering length density
TIRFM	total internal reflection microscopy
TxsRd DHPE	Texas Red 1,2 Dihexadecanoyl-sn-Glycero-3-Phosphoethanolamine, Triethylammonium Salt
XRR	X-ray reflectometry

Part I

INTRODUCTION

1

MOTIVATION

The interface between hard and soft matter has been a central element in scientific experiments for ages since putting soft matter on a substrate is in many cases a fundamental precondition for studying it. Students are already confronted with the particularities of this interface. In biology class, an onion skin is fixed on a cover glass to study it with a microscope. The fixation enables probing it by keeping it parallel to the focal plane of the objective. Put simply, viewing a whole onion under the microscope will not reveal much - whereas studying just a slice of onion fixed on a solid substrate, i.e. reducing the complexity of the problem, gives amazing insight.

The thesis at hand focuses on the structure of the interface between a solid substrate and a cell membrane. Every cell is surrounded by a membrane and it is perhaps the most abundant self-assembling molecular system in nature [1]. The total surface of membranes in the animal body covers an area of roughly five soccer fields [2]. In the epithelia, which line the inner and outer surfaces of the body, they form large assemblies; the skin and the lungs are prominent examples. Since the structural dimensions of a cell membrane and its components are in the nanometer and subnanometer range, the interaction with the interface of the selected substrate has to be considered and its effect becomes more prominent than for structures of larger dimensions.

The importance of cell membranes can hardly be overestimated. Their structure and functionality are a prerequisite for life. The membrane fulfills a multitude of different tasks and is highly complex and diverse. Unsurprisingly, membranes and their functions are directly linked to drug and gene delivery, a constantly relevant field of research. Many cell membranes are encountered along the different delivery routes before the drug meets the target [3]. The membrane also mediates cell adhesion. No multicellular life would exist without this highly complex and dynamical process. Its malfunction can cause severe diseases [4].

The understanding of the complexity of living cells is one of the challenges of physics in the 21st century [5]. Due to the enormous complexity of the membrane and the adhesion process, model systems are critical. They enable studying the structure of the cell membrane as well as processes like cell adhesion and the interactions of bio-

logically and pharmaceutically-relevant membrane components. Producing a good, biologically-relevant model membrane is very challenging [2]. The dimensions of its components, such as lipids and proteins, are in the nanometer and subnanometer range. Lipids are the main structure giving constituent of the cell membrane. Their self-organization in aqueous environments due to hydrophobic interactions is exploited in nearly all model systems, such as lipid vesicles and supported lipid layers. A huge insight into the molecular structure of membranes and details of the cell adhesion process was already gained using various sophisticated model systems on surfaces, and they are indispensable in many fields of research [6].

Artificial cell membranes are not only of interest to gain insight into cell membranes and cell adhesion. Furthermore, they also can be used as a coating or bio-functionalization of inorganic solids like semiconductors, gold covered surfaces, and optoelectronic devices, as well as of artificial organs and implanted medical devices [5]. They play a role in the development of biosensors, nanotechnology, and bioinspired material science [7].

An introduction to lipids, the cell membrane, model membranes and cell adhesion is given in CHAPTER 2.

The structural determination of the interface between adhering cells and an interface is the key to understanding the fundamentals of the adhesion process, just as the determination of the structure of the cell membrane is a fundamental prerequisite to understanding its function [5]. The structural analysis of these only a few nanometer thick, soft, and dynamic systems is very challenging. Such experiments are reaching the limits of currently available tools and methods [7], especially in a natural, aqueous environment.

Structural analysis of the cell, i.e. soft matter in the µm range, started with the invention of the microscope. The angular resolution d of a standard light microscope is given by the Abbe diffraction limit:

$$d = \frac{\lambda}{2NA} \quad , \tag{1.1}$$

with the wavelength of light λ and the numerical aperture NA of the objective of the microscope. For an immersion oil objective with a maximum NA of 1.40 and light with an average wavelength of 550 nm, the smallest structures that can be resolved have dimensions of around 200 nm. The resolution of light microscopy can be improved immensely by exploiting, for instance, the interference of light, and particularly by using fluorescence. For resolving structures with light microscopy, exploiting fluorescence becomes inevitable at some point.

STORM[1], PALM[2], and STED[3] microscopy are some of the techniques using fluorescence to resolve structures down to the nanometer range. The Nobel Price in Chemistry in 2014 was awarded for the development of super-resolved fluorescence microscopy [8], illustrating the importance of of high resolution. A second way to overcome the resolution limit of light microscopy is to go to smaller wavelengths. X-rays, electromagnetic waves with a wavelength from about 10 pm to 10 nm and neutrons with the wavelength of a few Å allow for the determination of structures within the subnanometer range, also in an aqueous environment. However, X-ray and neutron microscopy is hard to implement. For neutrons and X-rays the refractive index of most materials is close to 1, thus optics are immensely complicated to manufacture and far from being competitive to optics for visible light. Optical microscopy techniques allow performing direct measurements with a resolution in the nanometer range, and each real space techniques offers a particular perspective on the interface. Nonetheless, scattering experiments using X-rays or neutrons, the so-called Fourier space techniques, offer unique and particular properties that make them indispensable in modern physics nowadays.

The first Nobel Price in Physics was awarded in 1901 to Röntgen for the discovery of the X-rays. In 1912, here at LMU Munich, the first X-ray scattering experiment was performed by Friedrich and Knipping. Von Laue, who postulated the diffraction of X-rays on crystals, was awarded the Nobel Price in Physics in 1914 [9]. Neutrons, which interact differently with matter than electromagnetic waves, have unique properties which make them highly attractive, especially for soft matter. The Nobel Price in Physics in 1935 was awarded to Chadwick for the discovery of the neutron [10]. Neutron scattering has been linked to Munich since 1957, when Germany's first research neutron source was built just outside the city. The founding father of the neutron source, Meier-Leibnitz, also invented neutron guides, which are essential for today's scattering experiments.

Since the early days of X-ray and neutron scattering, manifold scattering methods have evolved. The method that lends itself to probing the interface between hard and soft matter is reflectometry, i.e. recording the specular reflection from interfaces. While averaging in-plane over structural features, the reflected signal yields one-dimensional information about the thickness and scattering length density profile of interface structures along the surface normal. This profile depends on the density and chemical composition of the interfacial layers. It is a versatile method to resolve structural aspects that influence

1 stochastic optical reconstruction microscopy
2 photo activated localization microscopy
3 stimulated emission depletion

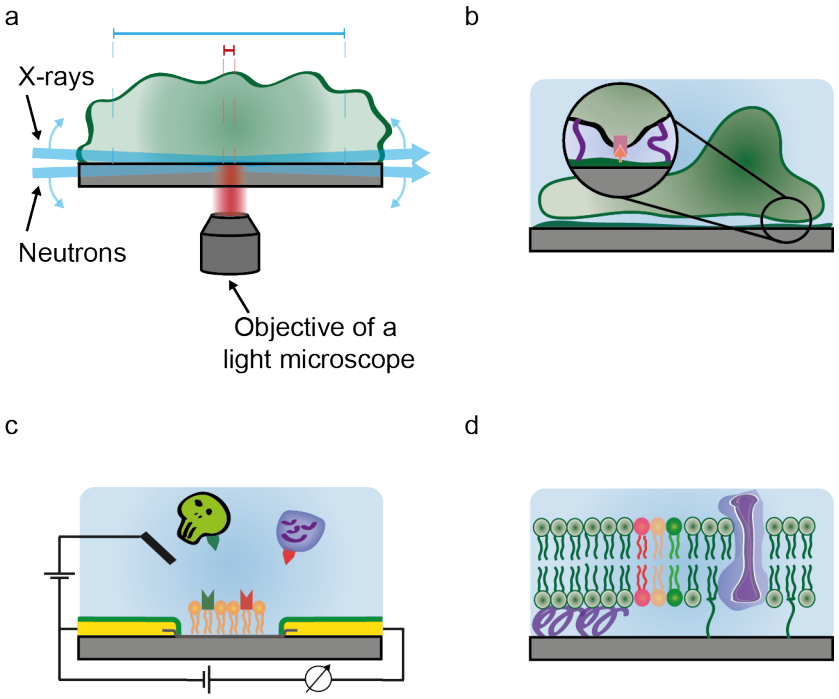

FIGURE 1.1: THE INTERFACE BETWEEN A SOLID SUBSTRATE AND A CELL MEMBRANE. **a** The interface between hard and soft matter can be investigated locally with real space techniques such as optical microscopy (red scale bar). Reflectometry averages in-plane over areas up to tens of square centimeters (blue scale bar) with a Å resolution perpendicular to the interface. X-rays travel through the sample and reflect on the interface. Neutrons, which interact weakly with matter and thus have the ability to penetrate deeply into many materials, can travel through, for instance, silicon substrates and reflect on the solid-liquid interface. This property enables probing buried interfaces. **b** A cell, depicted in green, on a solid substrate, depicted in grey. The hard matter - soft matter interface permits studying fundamental processes of the cell. The zoom-in gives an exemplary illustration of cell adhesion, one of the fundamental processes. **c** Model membranes are highly interesting as biofunctionalizations of sensing devices. **d** Model systems on surfaces, such as the shown supported lipid bilayer, are heavily used to deepen the understanding of cell membranes and cell adhesion.

the function of biomembranes and their components [7] and enables studying buried interfaces. Reflectometry is a popular technique for characterizing the structure of supported lipid layers and newly developed biomimetic membranes and is applicated to problems related to drug and gene delivery [1, 3]. The development of the instrumentation, specialized sample environment equipment, and analysis techniques has resulted in its application to complex interfaces and environments and in the study of complex multi-component systems such as surfactant and polymer adsorption, thin polymer films and model membranes [11]. Neutrons offer several significant differences compared to optical techniques in their capability to study soft matter at interfaces [3]. Although deuterium and hydrogen scatter light similarly, they scatter neutrons very differently. This distinct scattering behaviour can be exploited by varying the D_2O content in the liquid subphase or by selective deuteration in order to obtain different isotopic contrasts of the same system. Recording multiple neutron reflectivity profiles in different contrasts but in the same environment increases the reliability of the data analysis and allows for the determination of hydration profiles, giving structural and compositional insights in biophysical membranes [1]. Unlike X-rays, cold neutrons cause no beam damage in the sample, partly because they are less concentrated and thus the local dose is less intense. X-ray reflectometry (XRR), on the other hand, allows to perform experiments on smaller samples with a higher resolution due to a better signal-to-noise ratio than neutron reflectometry (NR). Furthermore, X-rays are much easier accessible since they can be generated with laboratory sources. An introduction to X-ray and neutron reflectometry, reflectometers and scattering theory will be given in Chapter 3. Figure 1.1 illustrates XRR, NR and optical microscopy on the interface between a solid substrate and soft matter as well as different aspects of cells and lipid layers on solid substrates.

In this thesis, the unique features of reflectometry were exploited to investigate the interface between a solid substrate and membranes. Two projects, out of two different fields of interest regarding this interface, were realized:

I Artificial cell membranes on substrates with the goal of creating bio-functionalized devices which enable the sensing of cell activity, cellular processes and molecules.

The structure of lipid layers on graphene, a complex functional material with many sensing applications, was analyzed with XRR. Resolving this structure is a prerequisite for future applications of lipid decorated graphene solution-gated field-effect transistor (SGFET) biosensors.

Graphene is biocompatible and a highly promising biosensing material. Its discovery was awarded the Nobel Price in Physics in 2010 [12]. Supported lipid membranes [6] are a widely-used model system because they are easy to prepare and to manipulate [1]. Although several studies on lipid layers on graphene were published, the lipid structure on graphene was still under debate. Quenching of light by the graphene prevents studying the lipid formation with light microscopy. Therefore, we studied the structure of charged lipid layers on graphene with XRR. Successive XRR measurements after each preparation step allowed to reveal a lipid monolayer structure. Due to the in-plane averaging over an area of around $12\,mm^2$ small inhomogeneities and defects did not affect the results. The XRR measurements were performed on the custom-built molybdenum-anode-based in-house reflectometer. Since high data quality and short measurement times were required for the experiments, the reflectometer was reconstructed within this thesis , see CHAPTER 4. In close cooperation with Benno Blaschke and Jose Garrido (Walter Schottky Institut und Physik-Department, Technische Universität, München) the formation of charged lipid layers on solution-gated field-effect transistors in real time was observed and the electrostatic screening of electrolyte ions quantified. A model that explains the influence of charged lipids on the ion sensitivity of solution-gated graphene field-effect transistors was derived and validated using the structural information from the X-ray reflectometry measurements. Detection of cationic lipids by self-exchange of lipids and measurements of the kinetics of layer formation induced by vesicle fusion or spreading from a reservoir with solution-gated graphene field-effect transistors was demonstrated. The results are presented in detail in CHAPTER 5.

II Living cells or cell-mimetic model systems adhering to a surface to study the structure and functionality of the cell membrane and cell adhesion.

The adhesion of a layer of epithelial cells was probed with NR, revealing a three-layered structure.

Insights into the dynamics of cell adhesion could be gained by the use of model systems, especially using functionalized lipid vesicles and reflection interference contrast microscopy. XRR and NR contributed significantly to the analysis of the structure of cell membranes. The suitability of neutrons for studying the process of cell adhesion is apparent. Nevertheless, only very few neutron reflectometry experiments on living cells have been reported so far. Especially, none of the reported experiments used contrast variation. The main reason for this is the high complexity of cells compared to model systems. The cell is a highly complex dynamic system. Living organisms make high demands on the sample environment, the infrastructure and also the data treatment. To be able to probe cell adhesion with the NR in the scope of this thesis, a concept for a sample chamber was developed, which provides the necessary sample environment for experiments with living cells. Sample chambers for NR and XRR measurements were constructed and further equipped with a holographic inline microscope, which allows for optical control during scattering experiments. Successful NR experiments on epithelial cells adhering to a silicon substrate were performed, allowing the study of a cell layer consisting of around 10^7 cells during one measurement, a number that can hardly be realized with any real space technique in a comparable time frame. Contrast variation made it possible to reveal a three-layered structure. XRR measurements gave no further insight into the structure. In CHAPTER 6 the sample chambers and the reflectometry measurements are presented and discussed.

The results of the experiments performed during this thesis and future applications are summarized and discussed in CHAPTER 7.

2 THE CELL MEMBRANE AND CELL ADHESION

2.1 INTRODUCTION

Cellular life requires compartmentalization. Separation from the harmful environment on the outside as well as localization of reagents resulting in higher efficiencies of reactions on the inside is a necessity. Cell adhesion, i.e. the ability of the cell to specifically coalesce, allows for building three-dimensional tissues. No animal life could exist without this ability. In tissues, cells are surrounded by a network of macromolecules, which form the so-called extracellular matrix (ECM). In fact, a considerable part of the volume of tissue is extracellular and filled with this organized hydrated network. As shown in previous publications the mechanical characteristics, such as the stiffness, and the chemical characteristics of the ECM have a direct influence on many processes inside the cell [13–18] and even inside the nucleus [19, 20]. The study of the behaviour of cells in different matrices today is an important field in the research of tumor growth [18, 21] as well as in the research field of drug delivery [22].

Exchange of material and interaction with the surrounding likewise are a prerequisite for life. The interface between extracellular and intracellular space thus has to be more than just a separating structure. Its functions include: sorting what enters and exits the cell, molecule transportation by way of ion pumps and channels and carrier proteins, hosting receptors that allow chemical messages to be exchanged between cells and systems, anchoring of the cytoskeleton to provide the shape of the cell, and participation in enzyme activity [5]. Therefore, producing a biologically relevant model membrane is very challenging. Ideally, the model should fulfil the following requirements: its composition should match the content of the real cell membrane under investigation as close as possible, it should be hydrated, i.e. stable in aqueous environment, it should be able to interact with other biological entities such as peptides, proteins, and DNA, and it should be free enough to allow for bilayer fluctuations and free movement of the lipid molecules [7]. Understanding membrane structure and how this relates to the biological function of membrane components represents one of the big challenges in structural biology research. Knowing the exact structure and its impact on the functionality could open the door for manipulation for, e.g., medical purposes [23].

In 1925, Gorter et al. found out that blood cells of different animals

are covered by a two molecules thick layer of amphiphilic molecules [24]. Today we know that the amphiphilic molecules, the so-called lipids, are the primary structure-giving component of the cell membrane. In SECTION 2.2 lipids and lipid bilayers will be introduced in more detail. Since then, the model of the cell membrane has evolved. The presence and importance of proteins were realized. First, the proteins only were associated peripherally with the membrane. In 1972, Singer et al. proposed the fluid-mosaic model of the cell membrane. It describes the lipid layer as a low-dimensional fluid where proteins are incorporated in the lipid bilayer and also peripherally associated [25]. In 1978, Israelachvili included heterogeneity in thickness and pore formation [26]. Sackmann et al. showed that a full picture of a cell membrane has to include the glycocalyx and the cytoskeleton [27]. The heterogeneous lipid-protein layer, the glycocalyx, and the cytoskeleton together build the so-called composite membrane. FIGURE 2.1 illustrates the elaboration of the model of the cell membrane from the lipid bilayer to the composite membrane.

Supported lipid layers are a highly attractive and variable model system for studying lipid layers and model cell membranes. Supported lipid layers can be used to build model cells [28, 29], to study ion channel activity [30], and to design highly selective biosensors [31]. An introduction to supported lipid layers will also be given in SECTION 2.2. In SECTION 2.3 an introduction to the composite membrane and in SECTION 2.4 an introduction to cell adhesion will be given. The focus will be on epithelial cells since the experiments in this thesis were done with this cell line. A brief introduction to epithelial cells is given in SECTION 6.4.

Since during this thesis, supported lipid layers and cell membranes were studied with X-ray and neutron reflectometry, a focus in this chapter will be on the structural analysis of supported membranes using these two methods. XRR and NR allow for analyzing the structure of fully hydrated lipid layers [32] and probing buried interfaces with a resolution of a few nm to Å. Therefore they are highly suited for analyzing membranes on and cell adhesion to surfaces. A detailed introduction to reflectometry is given in CHAPTER 3.

2.2 LIPIDS AND LIPID LAYERS

2.2.1 *Definition*

Lipids are molecules that are soluble in organic solvents but not in water [33]. The percentage by weight of lipids in membranes varies from 79 % in the myelin membrane (myelin can electrically insulate the nerve cell from its environment because of the high phospho-

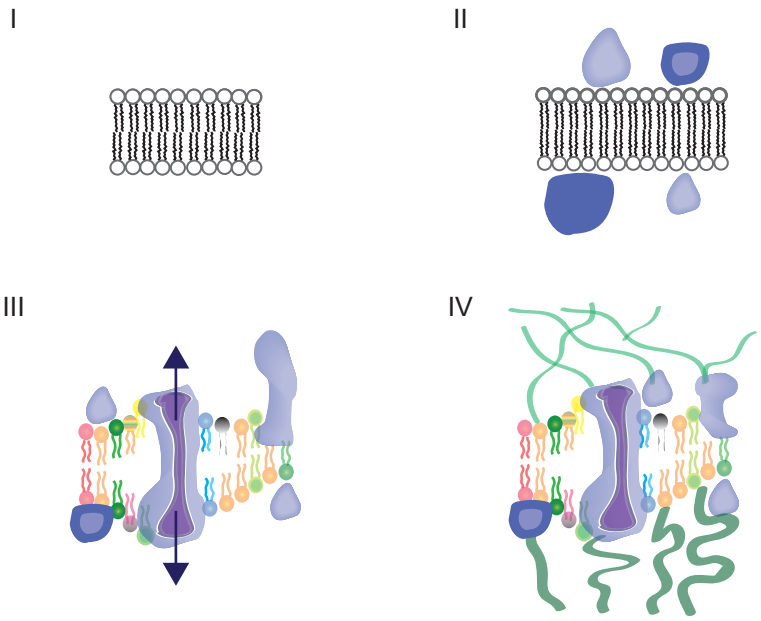

FIGURE 2.1: THE ELABORATION OF THE MODEL OF THE CELL MEMBRANE.
The elaboration of the model of the cell wall illustrated in four steps. Starting from the lipid bilayer, peripheral proteins were associated with the membrane in a second step. The model elaborated as incorporated proteins and asymmetry were included. The composite membrane takes into account the importance of the glycocalyx (dark green) and the actin cortex (light green).

lipid content) to 24 % in the mitochondrial inner membrane. In the plasma membrane it is around 50 % [7]. Prominent subgroups are triglycerides (the main constituent of fat in humans, animals, and plants) and steroids (like the sex hormone testosterone). Another important subgroup in the family of lipids, the so-called membrane lipids, is formed by phospholipids, glycolipids, and cholesterol. These molecules are amphiphilic, meaning they have a hydrophobic and a hydrophilic end, and are the major building blocks of the cell membrane. In aqueous environments, lipids express a polymorphism, depending on the ration of head to tail volume - the so-called packing parameter. The amphiphilicity and the packing parameter of membrane lipids lead to a double layer formation, as can be seen in FIGURE 2.2. Phospholipids are the major constituent of every eukaryotic cell membrane, and they are generally used in experiments with lipid layers.

2.2.2 *Phospholipids*

Phospholipids are divided into sphingolipids and glycerophospholipids. Two of the three lipids used in this thesis are glycerophospholipids, which are widely used for preparing bilayers [5]. Phos-

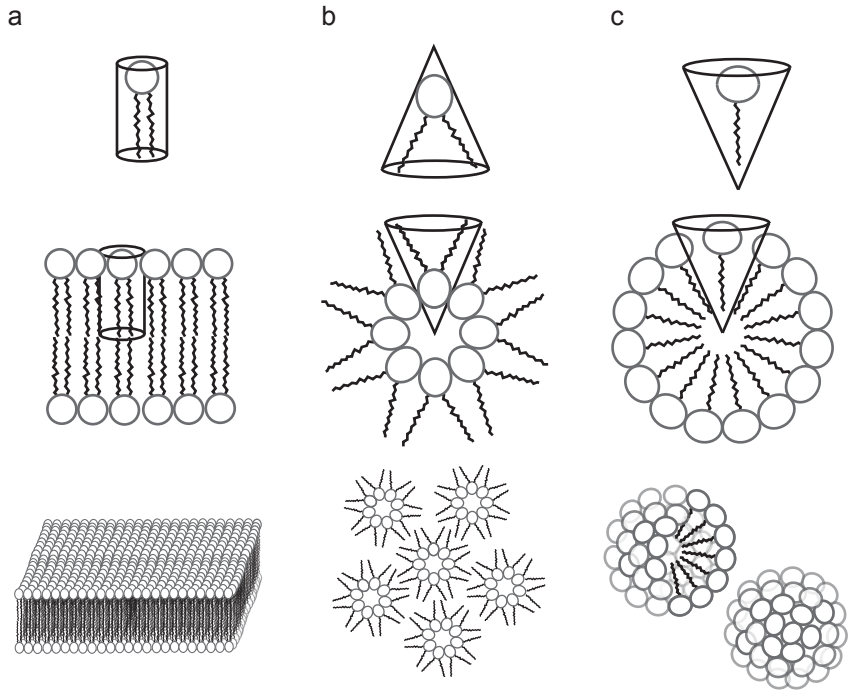

FIGURE 2.2: POLYMORPHISM OF LIPIDS WITH DIFFERENT PACKING PARAMETERS.
a Cylindrical lipids (packing parameter = 1) form a lamellar phase. The lipid bilayer is the basic structure giving element of a cell membrane. **b** and **c** Conoidal lipids (packing parameter < 1 or > 1) tend to build micelles in aqueous environment. They can have spherical or tubular shapes.

pholipids are categorized according to their different head groups and their two tails. The head groups can have a positive, negative or neutral (zwitterionic) net charge. Each head group can be combined with tails of different length. Fatty acids are hydrocarbon chains, connected either by single bonds (saturated) or single and double bonds (unsaturated). The fatty acids can have different lengths and a different number of double bonds, mostly one or two. 16 or 18 carbons long chains are often used in experiments, since they are dominant in nature [7]. The chain length can be varied to study the effect of chain length or parity. Molecules with a smaller chain length than 15 are usually soluble in water, so that the lipid layer is no more stable. The effect of head size, type or charge can be investigated by varying the head group.

Two to three letters for the head group combined with two representing the tail build the short name for the most common glycerophospholipids. The four most important headgroups of phospholipids in eukaryotes are phosphatidylcholine (PC, zwitterionic), phosphatidylethanolamine (PE, zwitterionic), phosphatidylserine (PS, negative) and phosphatidylinositol (PI, negative). In plants phosphatidylglycerol (PG, negative) additionally plays an important role.

Glycerophospholipids consist of a hydrophobic tail, composed of two fatty acid chains, and a hydrophilic head group. Glycerol connects the tail to the head. Each of the two hydrophobic/non-polar fatty acid chains is connected to one of the three OH-groups of the glycerol. The third OH-group is linked to phosphate which is connected to the headgroup.

FIGURE 2.3 shows the structure of the lipids used in the reflectometry experiments presented in CHAPTER 5, namely POPC, POPG, and DOTAP. Note that DOTAP has no phosphate and therefore is not a glycerophospholipid but a glycerolipid. Its trimethylammonium-propane (TAP) headgroup has a positive charge.

2.2.3 *The lipid bilayer - a complex two-dimensional fluid*

Hydrophobic interactions are the main driving force behind the spontaneous association of lipids to lipid bilayers - the entire membrane is held together by the non-covalent interaction of hydrophobic tails [5]. Lipid bilayers are the primary structural confinement unit of the cell membrane. They can be regarded as a complex two-dimensional fluid [6, 34]. A typical bilayer has a thickness of around 40 Å, the volume per lipid molecule is about 20 Å $\cdot$ 50 Å^2 [35]. Together with the embedded proteins, lipid bilayers form the so-called plasma membrane. FIGURE 2.4 shows the main movements of lipids in a natural lipid bilayer.

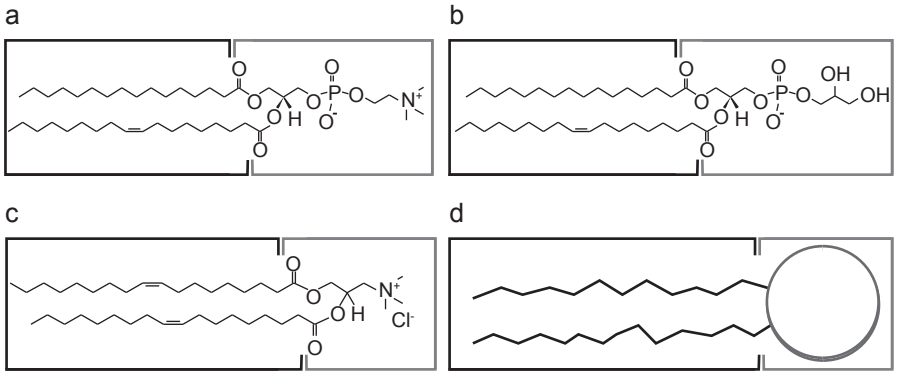

FIGURE 2.3: LIPID STRUCTURES.
The structure of **a** the zwitterionic glycerophospholipid POPC, **b** the negatively charged glycerophospholipid POPG, and **c** the positively charged glycerolipid DOTAP. The schematic for lipids used in this thesis is shown in **d**. The hydrophobic tail region is indicated by the black frame and the hydrophilic head group by the grey frame, respectively.

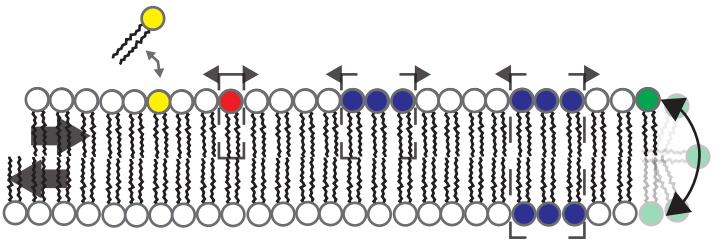

FIGURE 2.4: LIPID MOVEMENTS IN A BILAYER.
In a fluid lipid bilayer, the two monolayers can move independently, as indicated by the grey arrows. Single lipids can move individually in their layer (red), they can transfer to the other layer (green) and exchange (yellow). An important biological aspect have lipid domains that can form and move independently (blue).

Lipids play an active role. The function of many membrane proteins depends on the membrane composition and lipids serve the formation of local functional lipid-protein domains. These domains are important for regulating some signaling pathways [7]. The arrangement of lipids in the membrane is controlled by dynamical sorting and lateral phase separation [27]. It has been shown that, based on dynamic liquid-liquid immiscibility, the membrane can laterally segregate its constituents forming so-called lipid rafts. Lipid rafts are domains of sphingolipid, cholesterol, and proteins in the nanoscale that provide platforms for membrane signaling and trafficking [36]. The plasma membrane is a highly complex and dynamic system that consists of a large variety of lipids different in size, shape, and charge.

2.2.4 *Supported lipid layers*

2.2.4.1 *Overview*

The high complexity of biological membranes has motivated the development and application of a wide range of model membrane systems. When their geometry and composition can be tailored with great precision, they enable studying many aspects of membranes under well-defined conditions. The duplication of cell membranes in the laboratory and their investigation is very challenging. The need for biomimetic models has caused the revival of the classical approach: the use of lipid bilayers [7]. Supported lipid layers are a highly attractive and variable model system for a variety of scientific interests [6]. Lipid bilayers are probably the most natural substrate on which to test lipid–peptide or lipid-protein interactions [5]. On SiO_2 lipids form bilayers, whereas, on hydrophobic substrates, they tend to form monolayers [37–39]. FIGURE 2.5 shows some examples for different supported lipid layers and different applications. Supported lipid layers are a very easy to prepare and stable model system; they can be formed from a variety of lipids and be prepared to be of asymmetric composition [40]. They can be used as a workbench to study membrane processes and as a framework for, e.g., membrane proteins. In a supported lipid bilayer (SLB) the diffusion of lipids is not hindered. Lipid layers on a substrate, for instance, permitted the determination of the diffusion constants of different membrane ingredients [41], mostly with methods exploiting fluorescence like fluorescence recovery after photobleaching (FRAP) [42]. Enlarging the distance from the lipid layer to the surface avoids constraining effects that the solid may have on lipids and proteins in supported membranes. A larger distance can be achieved by tethering of the membrane, i.e. docking a free lipid bilayer onto the surface by sparsely spaced molecular anchors that penetrate the lipid layer [1], and with polymer cushions [43, 44]. Those two approaches allowed for reconstituting integral membrane proteins in a laterally mobile form [42], incorporating

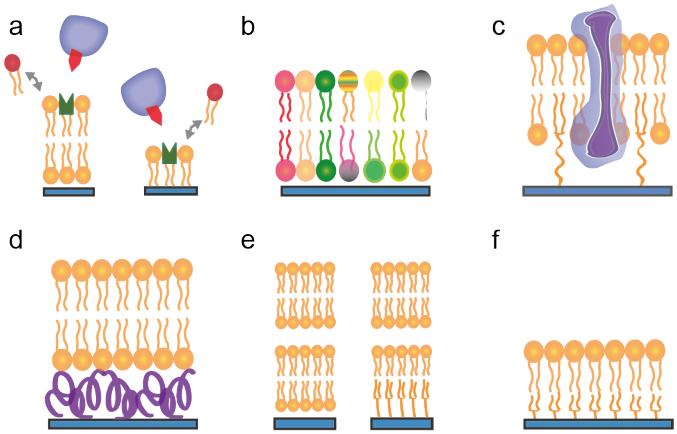

FIGURE 2.5: SUPPORTED LIPID LAYERS.
a On hydrophilic surfaces, lipids tend to form bilayers (left), whereas on hydrophobic surfaces they form a monolayer (right). Supported lipid layers can be functionalized and be used to study, e.g., self-exchange of lipids. **b** They can be of asymmetric lipid composition and be composed out of a natural composition of membrane lipids extracted from cells. Enlarging the distance from the lipid layer to the substrate by **c** tethering of the membrane or **d** a polymer cushion attenuates constraining effects from the solid substrate and allows for incorporating membrane proteins. **e** A floating bilayer also experiences weak interaction with the substrate, and can, e.g., be unbound by an applied electric field. **f** Hybrid bilayers have a nearly complete surface coverage.

trans-membrane proteins such as ion channels [30, 45, 46] and modeling the polymeric interface of the cytoskeleton or extracellular matrix, which has been shown to have an effect on the morphology of membrane domains and protein mobility [47]. Floating bilayers, lipid bilayers that float on top of a solid-supported lipid layer have proven to be very useful to probe bilayer-bilayer interactions [48, 49]. Lipid monolayers on top of a self-assembled alkyl monolayer are so-called hybrid bilayers. One of their advantages is that the lipids generally have a surface coverage close to 100 % [1]. Such high coverages are difficult to achieve in bilayers physisorbed on hydrophilic surfaces.

Reflectometry has played a significant part in revealing the structure of lipid layers and model membranes on surfaces. The first NR experiments started with supported lipid bilayers composed of one kind of lipid [50] to determine the structure of the bilayer. More and more complex membranes followed, like tethered SLBs [51] or floating bilayers [48, 52]. Reflectometry on a supported layer of lipids extracted from a bacterium [53] is a step towards more realistic lipid composure of the model membrane. The interaction of membranes with proteins as well has been studied intensively with reflectometry, like the binding of actin filaments to charged lipid monolayers [54] and the interaction of bilayers with peptides [55]. Recently, also the interaction

between nanoparticles and lipid bilayers [56, 57] has been probed. Reflectometry also allows for studying the formation of lipid layers by vesicle fusion [58]. Deuteration of lipids and contrast variation allowed for analyzing asymmetric arrangement of lipids in supported lipid bilayers with NR [59, 60], the effect of natural antioxidants on the structure of SLBs [61] and the pore formation in lipid membranes [62]. Reflectivity techniques are as well suited for studies of lipid monolayers at the air/liquid interface [63]. They are prepared by spreading a solution of lipids on the surface of water in a Langmuir trough [64] and are commonly referred to as Langmuir monolayers.

2.2.4.2 *Preparation methods*

The preparation methods for well-defined supported lipid layers can be divided into two categories [1]: in situ preparation by self-assembly or self-spreading in solution and ex situ spreading of the membrane onto the substrate surface, e.g., by the so-called Langmuir–Blodgett or Langmuir–Schäfer techniques [65]. Here, a short overview of the methods, which were used in this thesis, to coat substrates with lipids is given. They are in situ preparation methods. FIGURE 2.6 illustrates those methods, namely lipid spreading and vesicle fusion. The fusion of vesicles can be accelerated by inducing osmotic shock. When a lipid reservoir is deposited on a substrate (e.g., by stamping as described in more detail in CHAPTER 5) and immersed under aqueous solution, a lipid layer starts to spread over the bare surface. On hydrophilic surfaces, two different spreading mechanisms are possible, the sliding of a single bilayer on a thin lubricating water film and the rolling of two juxtaposed bilayers in a tank tread type motion [66]. Diffusion coefficients for spreading depend heavily on the lipid and the surface characteristics. On hydrophilic glass, typical diffusion coefficients for POPC at room tempeature are 2 - 4 $\mu m^2 s^{-1}$ and on hydrophobic n-octadecyltrichlorosilane (OTS) 0.5 - 1.5 $\mu m^2 s^{-1}$ [37]. The formation of a lipid layer from vesicle fusion involves spontaneous vesicle adhesion on the surface, rupture of the vesicles and fusion of the lipid layer patches.

2.3 THE COMPOSITE MEMBRANE

A significant step in the evolution of the model of the cell membrane was the recognition of the importance of the glycocalyx and the cytoskeleton, especially for cell motility and cell adhesion. The composite membrane can be divided into three layers. The center is the lipid-protein bilayer, also known as the plasma membrane, as described before. A lot of proteins that are essential for the cell, like ion channels, different enzymes, and proteins that act as anchors for the cytoskeleton, are embedded in the plasma membrane. On the intracellular side densely packed and cross-linked actin filaments form a cor-

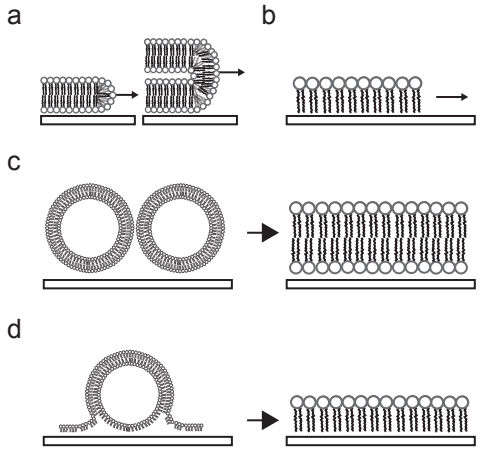

FIGURE 2.6: PREPARATION METHODS FOR SUPPORTED LIPID LAYERS.
Lipid spreading: **a** On hydrophilic substrates like SiO_2 lipids tend to form bilayer. The sliding of a single bilayer on a thin water film (left) and the rolling of two juxtaposed bilayers in a tank tread type motion (right) are possible. **b** On hydrophobic substrates a monolayer is spreading. **c** and **d** Vesicle adhesion and rupture results in a bilayer or monolayer, depending on the hydrophilicity of the substrate.

tex, the second layer. These filaments are coupled to the inner leaflet of the bilayer by various coupling proteins, also called actin-binding proteins [67]. The cortex ensures flexibility and mechanical stability of the bilayer. On the outside, the cell is coated with carbohydrate-rich molecules covalently bonded to the cell membrane's proteins and lipids. They form the third layer, the glycocalyx [68]. The 10 - 40 nm thick glycocalyx [27] mediates the contact to other cells or a substrate and protects the cell from parasites and contaminants. The right schematic in FIGURE 2.1 shows the three-layered composite membrane.

2.4 ADHESION OF EPITHELIAL CELLS

2.4.1 *Cell adhesion*

Epithelial cells adhere to the basal lamina, a thin, planar layer composed of extracellular matrix proteins. It supports all epithelia, muscle cells, and nerve cells. Adhesion of cells is a highly complex process, mediated by a variety of specific cell adhesion molecules (CAMs) (ligand-receptor pairs) [69]. Integrins are the main receptors used by animal cells to bind to the extracellular matrix. They are transmembrane linkers that mediate bidirectional interactions between the ECM and the actin cytoskeleton [33]. The basal lamina is composed of a homogenous, macromolecular network formed by collagens. Fi-

bronectin is an important extracellular matrix protein; it helps cells attach to the matrix. Many studies on cell adhesion are performed with cells adhering to surfaces. On solid surfaces, the cells flatten locally and establish initial contacts. Due to membrane fluctuations they are intermittent [70–72]. A model for the specific adhesion of cells was described by Bell [73], and the theory was vindicated for cells [69] and using cell-mimetic giant vesicles [74].

The specific adhesion of the epithelial cells on the basal lamina is controlled by short-range lock-and-key forces formed between cell adhesion molecules, such as integrins (exposed by the cell plasma membrane), and specific ligands exposed by the basal membrane [69, 75, 76]. These short-range forces act within the typical range of around 15 nm [76]. They form specific links with the proteins of the basal lamina such as collagen V and VI. The cell adhesion is also modulated by nonspecific forces, which govern the cohesion of colloids and the bending elastic modulus of the cell envelope. The elasticity is controlled by the competition between short-range attraction lock-and-key forces and long-range repulsions mediated by glycoproteins of the glycocalyx [75, 77]. The long-range repulsive forces act within the typical range of about 40 nm [76]. A variety of short- and long-range nonspecific forces which include attractive van der Waals and electrostatic interactions, repulsive undulation forces due to thermally excited flickering of the lipid-protein bilayer and a manifold of polymer induced forces also influence adhesion [75, 78, 79]. The polymers can apply strong repulsive forces between the adhering interfaces. Cell adhesion can be described as a competition between bond formation and cell-body deformation [80]. An illustration of the forces involved in cell adhesion is shown in FIGURE 2.7 A.

The adhesion of vesicles on different surfaces has been studied for decades with the motivation to understand and mimic cell adhesion. Vesicles on surfaces are ideal as a proof-of-principle approach as vesicles spreading on surfaces are a simpler model, which yet captures many aspects of cell adhesion [72]. According to Sackmann et al., cell adhesion can be understood as a wetting transition [75]. When a bare lipid vesicle is given on a substrate, nonspecific interaction of the membrane with the bare substrate result in high proximity of two surfaces and strong non-specific interaction [68]. The adhesion behaviour changes dramatically for vesicles where the glycocalyx is mimicked. Bruinsma et al. show in experiments with thermally excited bending undulations of multicomponent lipid vesicles with embedded lipid-anchored molecules, that the effective potential has two minima [81]. They show that the membrane switches between weak and strong adhesion states, suggesting that adhesion is determined by a double-well interfacial potential with minima at short (d_1) and

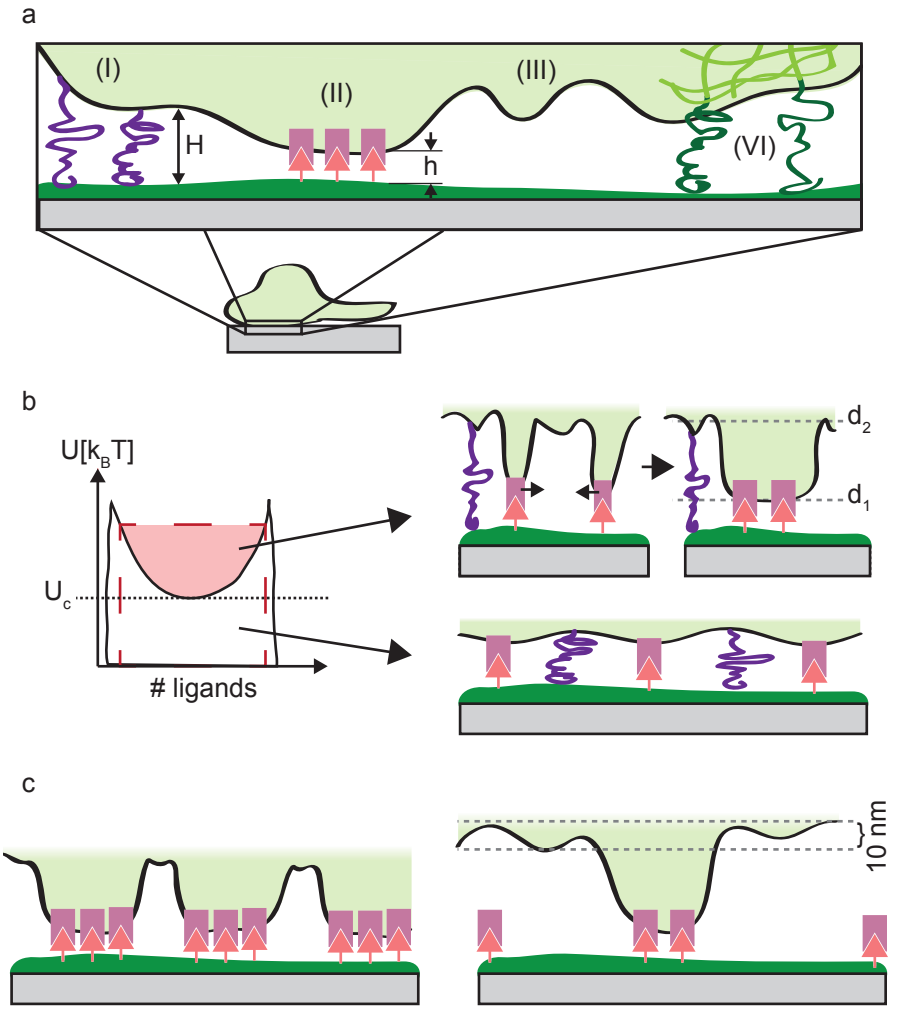

FIGURE 2.7: MECHANISMS OF CELL ADHESION. ADAPTED FROM [75] AND [76].
a Cell adhesion is controlled by an interplay of receptor-mediated specific forces, generic interfacial forces, and membrane elasticity. The figure illustrates a zoom in on the adhesion of a cell on a biofunctional surface, controlled by (I) repulsive forces from polymers and proteins, which act within the typical range H of 40 nm; (II) attractive lock-and-key forces mediated by CAM molecules, which act within the typical range h of 15 nm; (III) repulsive undulation forces due to thermally excited bending undulations of the plasma membrane; and (IV) polymer-induced attractive forces. **b** Membrane elasticity influences the adhesion. The left panel shows the phase diagram of adhesion, depending on the normalized bending energy U (y-axes) and the volume fraction of ligands (x-axes). In the miscibility gap (light red), micro-domains are formed by the accumulation of isolated CAM - CAM pairs. d_1 and d_2 denote the minima of the double-well interfacial potential. Below U_c a homogeneous state appears, i.e. very low local CAM concentration and d_2 - $d_1 \approx 0$. **c** Left panel: Many adhesion domains can be observed when the receptors are mobile, allowing for their accumulation. The receptors cannot accumulate when they are immobile (right panel). Adhesion points can only be observed at spots where the receptor density is high enough. The free membrane exhibits large fluctuations of around 10 nm.

long (d_2) distance from the surface. The typical distance d_2 is found 60 - 100 nm away from substrate. This minimum is gravity dominated. The mean-square amplitude of membrane fluctuations around d_2 can be up to 20 nm at room temperature. The minimum at d_1 is in a distance of around 5 - 10 nm from the substrate and dominated by van der Waals forces. In these adhesion domains, the fluctuations are suppressed. The wetting process results in the spontaneous formation of adhesion domains. Stable and weak non-specific adhesion can be achieved by passivating the substrate by, e.g., adsorbing a film of bovine serum albumin, fat-free milk or a lipid bilayer [68]. If the screening is only partial, the transition between the two states eventually will take place. Marx et al. show in studies of adhered complex membranes, that even this weak non-specific minimum can decompose into two minima [82]. The spontaneous formation of adhesion domains allows for cell adhesion at very low receptor densities. The concentration of receptors is essential for the formation of these adhesion domains. It can be influenced by membrane elasticity. The left panel of FIGURE 2.7 B shows a schematic of the phase diagram for cell adhesion depending on the volume fraction of ligands and the normalized bending energy. In the miscibility gap, micro-domains are formed by the accumulation of isolated CAM - CAM pairs. U_c marks the lower critical point of the miscibility gap. Below this point a homogeneous state appears, i.e. very low local CAM concentration and a small difference in height between the free and the bound membrane parts [76]. Smith et al. show that the mobility of the receptors also influences cell adhesion. They study an RGD-integrin vesicle-substrate system, where the integrin mobility gets varied [74]. Giant unilamellar vesicles with mobile RGD-peptide-carrying lipids interact with a SLB doped with $\alpha_{IIb}\beta_3$ integrins. Adhesion domains form at spots of locally elevated integrin concentration. For immobile receptors, the amount of adhesion domains is significantly lower. This might be relevant for cells adhering to solid substrates like SiO_2, as will be discussed in CHAPTER 6. The unbound parts of the membrane exhibit relatively strong fluctuations of around 10 nm. FIGURE 2.7 C shows the difference in the adhesion behaviour between the case of mobile and immobile receptors.

Pronounced short wavelength bending of about 10 nm root mean square amplitudes also have been observed in composite envelopes of nucleated cells [70]. The fluctuations impede strong adhesion due to entropic repulsion forces. The membrane fluctuations and the density of receptors are one of the leading environmental factors that affect the nucleation and the effective binding affinity of vesicles. It remains to be revealed how the cell uses and controls this affinity. In the context of cells, the fluctuations might have an important role too,

as they strongly influence the early stage of the cell adhesion [70–72].

2.4.2 *Techniques for studying vesicles and cells on substrates*

In the following, a short overview of the techniques, which are used to study vesicles or cells on surfaces is presented. Most of the studies are based on optical microscopy. All of these studies are single- or few-cell or respectively single- or few-vesicle approaches. These real space methods provide localized images of structures on surfaces. This is a central difference to NR, where snapshots of large areas - the number of probed cells is in the order of 10^6 - are averaged. NR has proven invaluable for looking at large areas [5]. In CHAPTER 6, NR experiments with cells will be presented.

The majority of studies on vesicles on surfaces was done using RICM (reflection interference contrast microscopy) [66, 83–85]. This method has a lateral resolution of about 0.2 nm and about 1 nm in the vertical plane [84]. With this method, the vesicle is illuminated by visible light through a transparent glass substrate. The light gets partially reflected from different interfaces on its way through the semi-transparent sample [86, 87]. The interference pattern of the reflected light beam is recorded. The review by Limozin et al. provides a comprehensive introduction to this technique [88]. Cells on surfaces also were studied intensively with this technique [86, 89–93]. The results of these studies, which are relevant for this thesis, are discussed in detail in this chapter and CHAPTER 6.

The distance of membranes to a substrate was furthermore measured with fluorescence interference contrast microscopy (FLIC) [94–96]. This fluorescence technique has a lateral resolution of a few nm [96]. Here, standing modes of light in front of the reflecting surface of silicon modulate the excitation and emission of fluorescent dyes. This technique was developed largely by Fromherz et al. with the focus to resolve the distance of the substrate to the cell membrane. The structural analysis of the cleft between the substrate and the cell is the key to understand the electrical coupling between cells and semiconductor chips. Fromherz et al. pioneered in the field of 'cells on a chip' by demonstrating the first electrical coupling between nerve cells and semiconductor microstructures [97–99]. Silicon is suitable as an electronically conductive substrate because the technology to fabricate microscopic semiconductor devices is well established, a layer of SiO_2 prevents silicon corrosion and cell damage from chemical processes with the silicon and SiO_2 coated silicon is a very suitable surface for the culture of nerve cells [100]. The efficiency of the electrical coupling depends on the resistance of the cleft and the current flow through

the attaching cell membrane.

The review of Parthasarathy et al. gives an overview of optical techniques for imaging membrane topography including RICM and FLIC [96].

A cell membrane labeled with a fluorescent dye can also be imaged with total internal reflection microscopy (TIRFM); the dye is excited by an evanescent wave of a totally reflected light beam [101–103]. The evanescent wave has an identical frequency to that of the incident light, and decays exponentially with increasing distance from the surface.

Paszek et al. presented a very promising elaboration in 2012. They developed scanning angle interference microscopy (SAIM), a combination of FLIC and TIRFM. Their approach eliminates the requirement for knowledge of the orientation of fluorescence dipoles in the labeled structure and allows for imaging with nanoscale axial precision [104]. They used this technique to reveal that metastatic tumours upregulate expression of bulky glycoproteins [105].

One study of NR with epithelial cells has been published so far [4], the results will be discussed in CHAPTER 6.

3

NEUTRON AND X-RAY REFLECTOMETRY

3.1 INTRODUCTION

X-ray and neutron reflectometry probe layered structures with sub-nanometer resolution. The specular reflection contains information about the thickness and scattering length density (SLD) profile of structures along the surface normal z. The SLD of each layer depends on its density and chemical composition [106, 107]. Since X-rays mostly scatter on the electron shell of an atom and neutrons mainly interact with the nuclei, the two techniques can give complementary information. Due to higher flux, XRR, in general, allows for measuring to higher q values. The momentum transfer q describes the change in momentum of the incident beam after reflecting from a surface and is defined as

$$q = \frac{4\pi}{\lambda} \sin\theta \ , \tag{3.1}$$

with the wavelength λ of the incident wave and the angle of incidence θ. Due to similar electron densities, the scattering contrast between most molecules and water is very small for X-rays. Neutrons often provide a much larger SLD contrast. Joint X-ray (for resolution) and neutron (for composition) experiments have a great potential for analyzing the structure of membranes and membrane interactions [5]. For the study of soft matter systems, the most distinct value of NR lies in the substitution of H_2O ($SLD_{H_2O} = -0.561 \cdot 10^{-6}$ Å^{-2}) with D_2O ($SLD_{D_2O} = 5.759 \cdot 10^{-6}$ Å^{-2}) in the solvent or deuteration, i.e. the specific exchange of H (scattering length = $-0.37 \cdot 10^{-12}$ cm) and D (scattering length = $0.67 \cdot 10^{-12}$ cm) in molecules. This can reduce the ambiguities resulting from the loss of phase information that is characteristic of all scattering experiments and can allow determining the hydration of the layers. The distinct interaction of neutrons with different isotopes of the same atom can be exploited to extract more detailed information out of a soft matter system by varying the scattering contrast of the solution. It is further possible to accentuate or annihilate the scattering from individual parts of a macromolecular complex by specific deuterium labeling. In general, all the reflectivity curves measured at different contrasts or isotopic compositions of the same physical system should allow for self-consistent modelling. According to Fragneto, experience suggests that the measurement of reflectivity curves from three or more contrasts, combined with standard physical hypotheses, are necessary and sufficient for extracting a unique model of the interface [7]. Nevertheless, it has to be kept

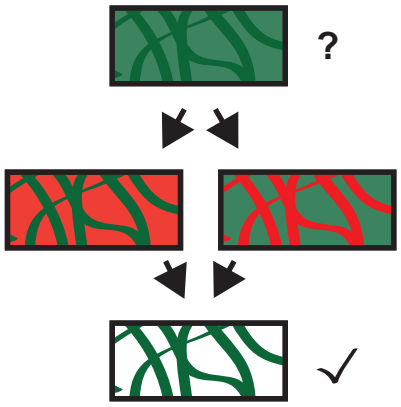

FIGURE 3.1: CONTRAST VARIATION AND DEUTERATION.
The different interaction of neutrons with different isotopes of the same atom enable to extract more detailed information from hydrated soft matter systems, by either varying the scattering contrast in the solution (left) or by deuteration of the molecules (right).

in mind that in highly complex systems, varying the contrast can change the layer structure due to, for instance, different intrinsic hydration behaviour and exchange efficiencies of each layer. FIGURE 3.1 illustrates the gain of information that can be achieved with contrast variation and deuteration.

3.2 INSTRUMENTS

A reflectometer requires an X-ray or neutron source, a monochromator or wavelength selector, a collimation system, a sample stage and a detector [7]. The detector can be zero-, one-, or two-dimensional. Only the amplitudes of the scattered waves can be measured while the phase shifts cannot be determined directly.

In the laboratory, X-rays can be generated with a laboratory X-ray source by accelerating electrons and shooting them at a metal target. The spectrum of X-rays generated from electrons impinging on a metal anode has two components. Electrons which get decelerated and eventually stopped in the target cause the continuous *Bremsstrahlung*. The maximum energy of the *Bremsstrahlung* corresponds to the voltage applied for acceleration of the electrons. If an incident electron removes an atomic electron from one of the inner shells, the vacancy is filled up by an electron from the outer shells of the atom. This process produces a photon with characteristic energy equal to the difference in energy between the two shells involved in this process. This sharp line spectrum is superimposed on the broad spectrum of the *Bremsstrahlung* [106]. X-rays further can be generated in a synchrotron. In this case, the electrons are accelerated to relativistic energy (in the

order of 4 GeV) and their direction is changed periodically. The emitted electromagnetic radiation is in the X-ray regime. Although the brilliance of synchrotrons beats those of laboratory sources by magnitudes, in-house X-ray setups are indispensable. The possibility to perform in-house X-ray measurements allows not only for proper preparation and test measurements for synchrotron experiments. Since the brilliance of laboratory X-ray sources such as sealed tubes, rotating-anode generators or liquid metal sources evolved remarkably [108], it is possible to record data of soft matter systems in-house in a satisfying quality. The spatial resolution of XRR is limited by the signal-to-noise ratio. The transmission of the sample is an important factor for the intensity of the signal. Especially for measurements in an aqueous environment, the transmission is relevant since the X-rays have to travel through the water reservoir. Scattering from the air, and from the window material are the biggest factors for the background radiation. All material which is in the beam path, except the sample itself, is defined as window material. This includes the windows in the casing of the source and vacuum tube and sample chamber windows. A detailed description of the in-house XRR setup used in this thesis is given in CHAPTER 4.

Neutrons are produced either by nuclear fission or spallation, i.e. either at nuclear reactors or at accelerator-based sources. Accelerator-based sources can provide a pulsed peak flux that is much higher than at a reactor. Compared to photons, neutrons are not created but have to be 'mined' from atomic nuclei where they are tightly bound, and a significant amount of energy is involved in the process of extracting them. The spatial resolution of NR is limited by the high background signal and the resulting signal to noise ratio [7], with the incoherent scattering by the bulk liquid subphase being the main source of background [1]. Instrumental contributions like air scattering and scattering from windows in the beam increase the background further. Since the angle of incidence is equal to the angle of reflection and the radiation source cannot be moved, the sample and the detector must be mobile to record the specular reflectivity at different angles. The reflectivity can be measured in two modes: the monochromatic mode and the time-of-flight mode [1, 3, 5]. In the monochromatic mode, the angle of incidence is scanned at a constant wavelength. The time-of-flight mode measures at a few fixed angles of incidence, using a polychromatic neutron beam that is analyzed for the wavelength λ by determining the velocity of each neutron at a single angle. These two modes are frequently combined in practice [3].

3.3 THEORY OF SPECULAR REFLECTIVITY

3.3.1 *Refractive index and scattering length density*

When neutrons or photons hit the surface of a layer with refractive index n, they are either reflected or transmitted. The refractive index n of a medium is defined as

$$n = 1 - \delta + i\beta \ , \tag{3.2}$$

with the dispersion δ and the absorption β.
For X-rays, the dispersion is

$$\delta = \frac{\lambda^2}{2\pi}\rho r_0 \ , \tag{3.3}$$

with the wavelength λ of the incident wave, the electron density ρ of the medium and the classical electron radius r_0. The absorption β is given by

$$\beta = \frac{\lambda}{4\pi}\mu \ , \tag{3.4}$$

with the absorption coefficient μ.
The SLD of a material with j different atoms can be approximated by

$$SLD_{X-ray} = \frac{\sum_{k=1}^{j}(Zr_0)_k}{V_m} \ , \tag{3.5}$$

where the atomic scattering factor is approximated by the atomic number Z, and V_m is the volume of the material [109, 110].
For neutrons, the dispersion is given by

$$\delta = \frac{\lambda^2}{2\pi}Nb \ , \tag{3.6}$$

and the absorption by

$$\delta = \frac{\lambda}{4\pi}\sigma_a N \ . \tag{3.7}$$

Here, N is the atomic number density, b the bound coherent scattering length, λ the neutron wavelength, and σ_a the absorption cross section.
The SLD of a material interacting with neutrons is given by

$$SLD_{neutron} = \frac{\sum_{k=1}^{j} b_k}{V_m} \ , \tag{3.8}$$

b_k denotes the coherent scattering length of the k_{th} atom in the material [110].

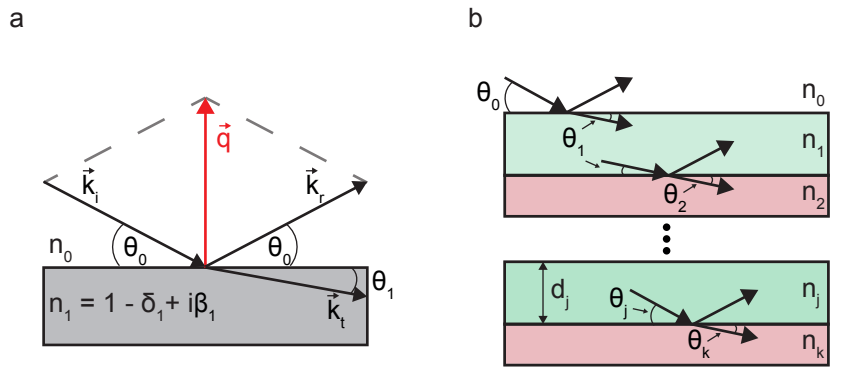

FIGURE 3.2: REFLECTION AND TRANSMISSION AT AN INTERFACE.
a An incoming beam, denoted by the wave vector $\mathbf{k_i}$ hits the surface of a infinitely thick layer with refractive index $\mathbf{n_1}$ at an angle θ_0. The reflected beam and the transmitted beam are denoted by $\mathbf{k_r}$ and $\mathbf{k_t}$, respectively. The momentum transfer vector $\mathbf{q}$ perpendicular to the surface ($|\mathbf{q}| = 4\pi \sin\theta_0/\lambda = |\mathbf{k_i} - \mathbf{k_r}|$) is shown in red. **b** Reflection and transmission of an incoming beam on a multilayer system with layers of finite thickness d.

3.3.2 *Reflection and transmission at an interface*

FIGURE 3.2 A shows an incoming beam $\mathbf{k_i}$ that hits a layer with refractive index n_1 at the angle θ_0 and is reflected ($\mathbf{k_r}$).

Following Snell's law,

$$n_0 \cos\theta_0 = n_1 \cos\theta_1 \quad . \tag{3.9}$$

The critical angle of total reflection θ_c can be determined by setting $\theta_1 = 0$,

$$\cos\theta_c = \frac{n_1}{n_0} \quad . \tag{3.10}$$

The reflected intensity R for $\theta > \theta_c$ from an indefinitely thick layer is obtained from the Fresnel equation,

$$R = \left| \frac{n_0 \sin\theta_0 - n_1 \sin\theta_1}{n_0 \sin\theta_0 + n_1 \sin\theta_1} \right|^2 \equiv |r_{01}|^2 = |r_{jk}|^2 \quad . \tag{3.11}$$

r_{jk} is defined as the Fresnel coefficient on the jk interface. Reflection and transmission of an incoming beam at a multilayer system is sketched in FIGURE 3.2 B. In this thesis, the data evaluation is done with Motofit [111]. The measured system is approximated with a multilayer model. Each layer is defined by a thickness, a SLD, and a roughness or diffuseness, respectively. An error function accounts for the roughness or respectively the diffuseness of each interface [112],

$$r_{j,j+1} = \left(\frac{n_j q_j - n_{j+1} q_{j+1}}{n_j q_j + n_{j+1} q_{j+1}} \right) exp\left(-\frac{q_j q_{j+1} \langle\sigma\rangle^2_{j,j+1}}{2} \right) \quad . \tag{3.12}$$

$\langle\sigma\rangle$ is the root mean square roughness of the interface and q_j is the momentum transfer perpendicular to the surface. It is defined as

$$q_j = \frac{4\pi}{\lambda}\sin\theta_j \quad . \tag{3.13}$$

The program calculates the reflectivity using the Abeles matrix method [113]. For each layer, a characteristic matrix C_j is calculated:

$$C_j = \begin{bmatrix} e^{i\beta_{j-1}} & r_j e^{i\beta_{j-1}} \\ r_j e^{-i\beta_{j-1}} & e^{-i\beta_{j-1}} \end{bmatrix} \quad . \tag{3.14}$$

β_j is the optical path length in the j-th layer and is defined by:

$$\beta_j = \frac{2\pi}{\lambda} n_j d_j \sin\theta_j \quad . \tag{3.15}$$

The matrix elements M_{11} and M_{21} of the resultant matrix M,

$$M = \prod_{j=1}^{k} C_j \quad , \tag{3.16}$$

are used to calculate the reflectivity R:

$$R = \left|\frac{M_{21}}{M_{11}}\right|^2 \quad . \tag{3.17}$$

The decrease of the reflected intensity ($R(q)$) with q can be estimated as follows. We will consider the case of the reflection at an infinitely thick layer as shown in FIGURE 3.2 A. Using the small-angle approximation $\sin(\theta) \approx \theta$, we can assume for the reflected intensity R:

$$R(\theta) = \left|\frac{n_0\sin(\theta_0) - n_1\sin(\theta_1)}{n_0\sin(\theta_0) + n_1\sin(\theta_1)}\right|^2 \approx \left|\frac{n_0\theta_0 - n_1\theta_1}{n_0\theta_0 + n_1\theta_1}\right|^2 \quad . \tag{3.18}$$

Using the definition for the critical angle θ_c given in EQUATION 3.10 and the small-angle approximation for $\cos\theta \approx 1 - \theta^2/2$ we get

$$\cos\theta_0 = 1 - \frac{\theta_0^2}{2} \tag{3.19}$$

$$= \frac{n_1}{n_0}\cos\theta_1 = \cos\theta_c\cos\theta_1 \tag{3.20}$$

$$= (1 - \frac{\theta_c^2}{2})(1 - \frac{\theta_1^2}{2}) = 1 - \frac{\theta_c^2}{2} - \frac{\theta_1^2}{2} + \frac{\theta_c^2\theta_1^2}{2} \quad . \tag{3.21}$$

As $\theta_c^2\theta_1^2/2$ is very small we neglect it. Thus we get:

$$\theta_1 = \sqrt{\theta_0^2 - \theta_c^2} \quad . \tag{3.22}$$

Transforming EQUATION 3.9 gives $\cos(\theta_0) = n_1/n_0\cos(\theta_1)$. Now we can write EQUATION 3.18 as

$$R(\theta) \approx \left| \frac{\theta_0 - (n_1/n_0)\theta_1}{\theta_0 + (n_1/n_0)\theta_1} \right|^2 \tag{3.23}$$

$$\approx \left| \frac{\theta_0 - \sqrt{\theta_0^2 - \theta_c^2}}{\theta_0 + \sqrt{\theta_0^2 - \theta_c^2}} \right|^2 \tag{3.24}$$

$$= \left| \frac{1 - \sqrt{\theta_0^2 - \theta_c^2}/\theta_0}{1 + \sqrt{\theta_0^2 - \theta_c^2}/\theta_0} \right|^2 \tag{3.25}$$

$$= \left| \frac{1 - \sqrt{1 - (\theta_c/\theta_0)^2}}{1 + \sqrt{1 - (\theta_c/\theta_0)^2}} \right|^2 \quad . \tag{3.26}$$

Applying the Taylor series for $\sqrt{1-x}$ and the approximation $2 - \frac{1}{2} \cdot \frac{{\theta_c}^2}{{\theta_1}^2} \approx 2$ for incident angles above the critical angle of total reflection, we get:

$$R(\theta) \approx \left| \frac{1 - 1 + \frac{1}{2} \cdot \frac{{\theta_c}^2}{{\theta_1}^2}}{1 + 1 - \frac{1}{2} \cdot \frac{{\theta_c}^2}{{\theta_0}^2}} \right|^2 \approx \left| \frac{1}{4} \cdot \frac{{\theta_c}^2}{{\theta_0}^2} \right|^2 \sim \left| \frac{\theta_c}{\theta_0} \right|^4 \quad . \tag{3.27}$$

Since θ_c is constant and with $q \sim \theta_0$ in small-angle approximation, we can see the q^{-4} dependence of R(q):

$$\left| \frac{\theta_c}{\theta_0} \right|^4 \sim \left| \frac{1}{q} \right|^4 = \frac{1}{q^4} \quad . \tag{3.28}$$

In the case of a thin, smooth layer on the surface, the rapid decrease of the intensity is modulated by oscillations, the so-called Kiessig fringes [114]. They result from constructive and destructive interference of the beam reflected from the two interfaces. Their period is determined by the thickness d of the layer:

$$d = \frac{2\pi}{\Delta q} \quad . \tag{3.29}$$

FIGURE 3.3 A shows the normalized reflectivity of Si with a 200 Å thick SiO_2 layer, where Kiessig fringes can be seen. They can hardly be resolved for thicker layers, as shown in FIGURE 3.3 B in the case of a 2000 Å thick SiO_2 layer.

3.4 DATA ANALYSIS

In the following a short overview of reflectometry data evaluation, as it has been performed in this thesis, is presented. The first step is to assume a SLD profile. This profile is transformed to a reflectivity

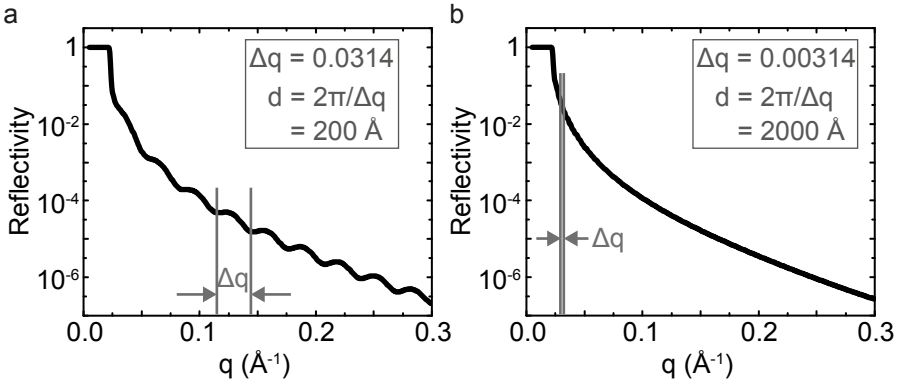

FIGURE 3.3: KIESSIG FRINGES.
a In the normalized reflected intensity of Si with a 200 Å thick SiO_2 layer, the oscillations clearly can be seen. **b** In the normalized reflected intensity of Si with a 2000 Å thick SiO_2 layer, they hardly can be resolved.

curve. The most common formalisms are the Abeles matrix method [3], which is explained in the previous section, and Parratt's recursive method [115]. The parameters of all layers involved in the problem are adjusted until the modeled reflectivity matches the measured reflectivity as good as possible. Since the phase of the reflected beam cannot be measured, and the phase information is lost, the reflectivity curves cannot directly be converted to the real space SLD profile. Consequently, the conversion is ambiguous. It is therefore per se unclear, whether or not an obtained SLD profile is realistic at all. In NR, the ambiguity can be reduced by variation of the scattering contrast.

Consequently, it is essential to use a realistic and well-thought-out model as the base for data analysis. In simplest terms, this means for, e.g., a lipid layer that there is a physically realistic relationship between the areas occupied by the lipid headgroups and tails [1]. It is much easier to verify that a physically reasonable model is used and the fitting is much more stable in reaching a defined minimum if only a few parameters are required in the physical description of the system [3]. In the reflectometry data analysis presented in this thesis, simple models with a low number of layers, i.e. parameters, are always chosen to avoid overparametrisation.

Part II

RECONSTRUCTION OF THE CUSTOM-BUILT MOLYBDENUM-ANODE-BASED IN-HOUSE REFLECTOMETER

4

RECONSTRUCTION OF THE CUSTOM-BUILT MOLYBDENUM-ANODE-BASED IN-HOUSE REFLECTOMETER

The X-ray reflectivity measurements presented in this thesis were performed at a custom-built molybdenum-anode-based in-house reflectometer. It was reconstructed within this thesis for two reasons. Firstly, to optimize the photon flux by reducing the distance from source to detector. Secondly, to create more space around the sample position, so that a larger variety of sample environments can be used. In this thesis, reflectometry experiments were performed on supported lipid layers and cells, and for both samples, it is beneficial to have as short measurement times as possible. Lipid layers can be degraded, e.g., by exposure to air that enters the measurement chamber over time. The importance of short measurement times when doing experiments with cells will be discussed in detail in CHAPTER 6. Since some of the experiments presented in this thesis demand a sophisticated sample environment, more space on the sample position than provided in the old configuration of the setup was required.

About five times higher photon counts per second are measured at the detector position after the distance between the X-ray source, and the sample was halved from about 70 cm to 35 cm. The higher photon flux shortens the measuring time around a factor of five. A supported lipid bilayer in H_2O for example, including a background measurement, can now be measured overnight compared to two full days before the reconstruction. The free space that was gained on the optical table by reducing the distance from source to detector was used to build up a small-angle X-ray scattering (SAXS) setup which is described in more detail in the master thesis of Martina Ober [116].

More space around the sample position was achieved by replacing the Euler cradle by motorized stages. The removal enables to reach a larger $\theta/2\theta$ range (40°/80° compared to 30°/60°). The ability to move around the other rotational axes, namely around the χ and ϕ angle, as well as along the translational axes x and y, was preserved. A new sample stage, designed to hold different types of sample chambers was installed. The sample now is moved by an X-Y stage (5102, Huber, Rimsting, Germany), a 2-circle element (5203, Huber, Rimsting, Germany) and a Z stage (VSR20A-T3, Zaber, Vancouver, Canada). The 2-circle element has smaller angular ranges than the Euler cradle, but for the planned reflectometer experiments the range is fully

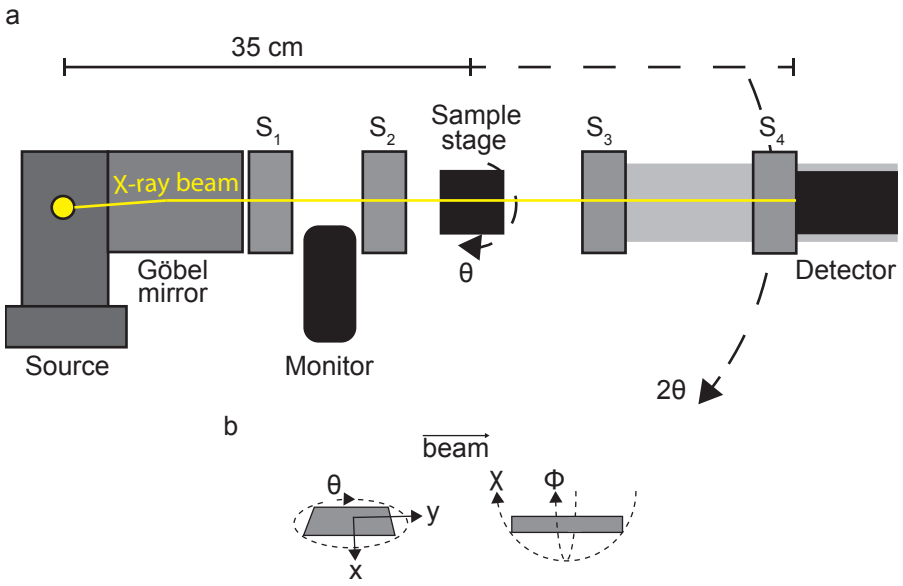

FIGURE 4.1: THE MOLYBDENUM-ANODE-BASED IN-HOUSE REFLECTOMETER.
a Schematic top view of the reconstructed molybdenum-anode-based in-house reflectometer. The X-ray source has a line focus. The slits S_1 - S_3 are motorized. The source-sample distance is 35 cm, the distance from the sample to the detector can be adjusted according to the sample environment. **b** illustrates the rotational and translational axis of the sample stage.

adequate. The detector (2θ) and the θ angle still are moved by a 2-circle goniometer (424, Huber, Rimsting, Germany). In FIGURE 4.1 A the reconstructed setup is sketched from the top view, in B the rotational and translational axes of the sample stage are illustrated. The space that was gained around the sample position allows for performing a larger variety of experiments, e.g., in the heatable custom-built sample chamber that is presented in more detail in CHAPTER 6. It was used, e.g., for measurements with cells in this thesis (also presented in CHAPTER 6), as well as by Christina Dirscherl for experiments, which required heating, on light-switchable lipid membranes during her Master thesis [117].

The X-ray source is a molybdenum line focus X-ray tube (Seifert DX MO 10x0.15, GE, Boston, USA). A Göbel multilayer mirror (Rigaku, Tokyo, Japan) delivers a monochromatic beam with an energy of 17.4 keV. Additionally, the slit behind the Göbel mirror was replaced by a motorized slit (3002.30M, Huber, Rimsting, Germany), which allows for better control of the beam shape and more precise adjustment. The stages, as well as the new slit, are controlled by a new motor controller (phyMOTION, Phytron, Gröbenzell, Germany). Data is recorded by a NaI scintillator (0 D) (Seifert, GE, Boston, USA). A second NaI scintillator (0 D) (Seifert, GE, Boston, USA) is used as monitor. This allows for taking account of intensity fluctuations of

the direct beam. The horizontal divergence of the beam is 0.51 mrad and the vertical divergence 72 mrad [116].

In FIGURE 4.2 A the normalized reflected intensity of a Si (001) die with a 200 nm thick SiO_2 layer before (green) and after reconstruction is shown (red). Now, normalized intensity data can be recorded up to 10^{-7}, around two orders of magnitude more than before the reconstruction (10^{-5}). Subtraction of a background measurement ($2\theta_{bg} = 2\theta + 0.2$) further increases the normalized intensity data range to around 10^{-8}. The data is shown in black. FIGURE 4.2 B shows a measurement of the 004 peak of silicon. The splitting of $K_{\alpha 1}$ and $K_{\alpha 2}$ can be seen. The q values for the $K_{\alpha 1}$ and the $K_{\alpha 2}$ peak can be calculated from Bragg's law,

$$n\lambda = 2d_{hkl}\sin(\theta) \quad , \tag{4.1}$$

with an integer n, the wavelength λ, the distance of the lattice planes d_{hkl} and the angle of incidence θ. For cubic systems we can express d_{hkl} by the Laue indices hkl and the lattice constant a_0,

$$d_{hkl} = \frac{a_0}{\sqrt{h^2 + k^2 + l^2}} \quad . \tag{4.2}$$

For silicon, a_0 = 5.431 Å and as we probe the 004 peak, $\sqrt{h^2 + k^2 + l^2}$ = 4. For calculating the theoretical peak positions we can solve EQUATION 4.1 for θ,

$$\theta = \sin^{-1}\left(\frac{4\lambda}{2a_0}\right) \quad . \tag{4.3}$$

For $K_{\alpha 1}$ the wavelength is $\lambda_{K\alpha 1}$ = 0.7093 Å, yielding $2\theta_{\alpha 1}$ = 30.28°. For $K_{\alpha 2}$ the wavelength is $\lambda_{K\alpha 2}$ = 0.7136 Å, yielding $2\theta_{\alpha 2}$ = 30.46°. This is in reasonable agreement with the fitted peak positions $\theta_{\alpha 1}$ = 30.26° and $\theta_{\alpha 2}$ = 30.44° of the shown data confirming a successful alignment.

Data that demonstrates the eligibility of the setup for measuring membranes on substrates in H_2O is presented in FIGURE 4.3. For typical slit settings and a beam size of 10 mm · 0.35 mm after collimation, the flux is 1.1×10^8 photons/s. The specular reflectivity of a POPC bilayer (with 0.5 % TxsRd DHPE) on $SiO_2$is shown in FIGURE 4.3 A. The data before and after subtraction of the background is shown. The inset of FIGURE 4.3 A shows the reflected intensity of a bare Si die with a 200 nm thick SiO_2 layer in water. Experiments were performed as $\theta - 2\theta$ scans of sample and detector angle, the background measurement with an offset for θ of $-0.05°$. The effective beam height was corrected as described by Salah et al. [118]. FIGURE 4.3 B shows the SLD profiles used for modelling the reflectivity curves for the supported bilayer and the bare substrate. An illustration of the bilayer

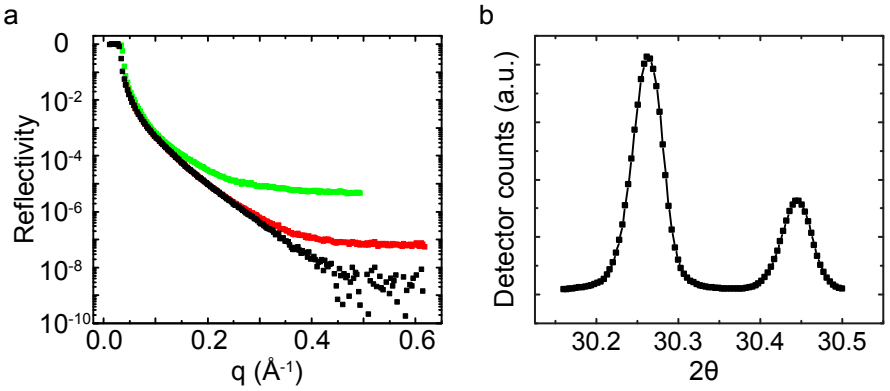

FIGURE 4.2: COMPARISON OF THE REFLECTIVITY OF A SiO_2/H_2O INTERFACE RECORDED BEFORE AND AFTER RECONSTRUCTION AND MEASUREMENT OF THE SI 004 PEAK.

a Normalized reflected intensity of a Si die with a 200 nm thick SiO_2 layer before (green) and after (red) reconstruction of the reflectometer. The black curve shows the background corrected data recorded on the reconstructed setup. **b** Measurement of the 004 peak of silicon, confirming the correct alignment of reconstructed setup. The splitting of $K_{\alpha 1}$ (left) and $K_{\alpha 2}$ (right) can clearly be seen.

is shown, too. The reflectivity curves resulting from the SLD profiles are shown in FIGURE 4.3 A. The reflectivity of the lipid bilayer before and after background subtraction was fitted with the same model; only the background level was shifted from $9.76 \cdot 10^{-7}$ to $3 \cdot 10^{-8}$ to account for its subtraction. All fitting parameters can be found in TABULAR 4.1 at the end of this chapter.

In summary, improving the in-house instrument resulted in an increase in the intensity and shorter measuring times, a better signal-to-noise ratio and a higher accessible q-range.

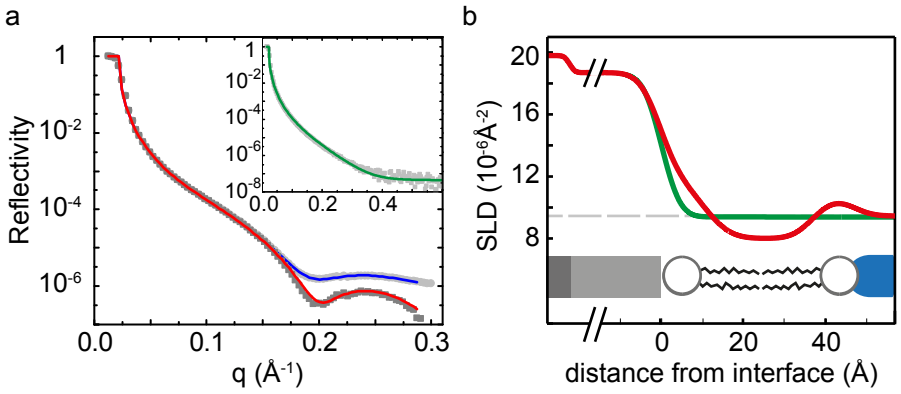

FIGURE 4.3: REFLECTIVITY OF BARE SUBSTRATE AND SUPPORTED LIPID BILAYER, AND SLD PROFILES.

a The specular reflectivity of a POPC lipid bilayer (0.5 % TxsRd DHPE) on a Si die with a 200 nm thick SiO_2layer. The light grey circles show the recorded data before subtraction of the background, the grey squares show the data corrected for background. The inset shows the reflected intensity of a bare Si die with a 200 nm thick SiO_2layer in water. Solid lines show reflectivity of the bare substrate (green), the bilayer before (blue) and after (red) background subtraction; resulting from the SLD profiles shown in b. The same model was assumed for the lipid bilayer before and after background correction; only the background level was shifted from $1 \cdot 10^{-6}$ to $3 \cdot 10^{-8}$ to account for its subtraction. **b** The SLD profiles used for modelling of the reflectivity curves for the supported bilayer (red) and the bare substrate (green) and an illustration of the lipid bilayer on the substrate. The dashed line indicates the SLD of water ($9.45 \cdot 10^{-6}$ Å^{-2}).

Layer description	**Thickness** (Å)	**Roughness** (Å)	**SLD** (10^{-6} Å^{-2})
Si with 200 nm thick layer of SiO_2			
Si	-	1.11	19.8
SiO_2	2000	4.67	18.7
H_2O	-	-	9.45
POPC bilayer with 0.5 % TxsRd DHPE on Si with 200 nm thick layer of SiO_2			
Si	-	1.036	19.8
SiO_2	2000	3.97	18.7
Lipid head region	10.93	4.97	11.93
Lipid tail region	26.2	3.97	8
Lipid head region	9.83	3.69	10.59
H_2O	-	-	9.45

Table 4.1: PARAMETERS FOR MODELLING REFLECTIVITY.
Parameters used for modelling the reflectivity data of the bare SiO_2 substrate and after deposition of a POPC bilayer with 0.5 % TxsRd DHPE.

Part III

THE STRUCTURE AND THE FORMATION DYNAMICS OF LIPID LAYERS ON GRAPHENE

5

THE STRUCTURE AND THE FORMATION DYNAMICS OF LIPID LAYERS ON GRAPHENE

The results presented in this chapter were obtained in strong collaboration with Benno Blaschke (Walter Schottky Institut und Physik-Department, Technische Universität München). Electrical characterizations as well as spreading experiments were performed by Benno Blaschke. Parts of this chapter are adapted from [119].

5.1 INTRODUCTION

Anionic and cationic lipids are key molecules involved in many cellular processes; their distribution in biomembranes is highly asymmetric and their concentration is well controlled. Solution-gated graphene field-effect transistors (SGFETs) exhibit high sensitivity towards the presence of surface charges.

Although several studies on lipid layers on graphene were published, fundamental questions such as the lipid structure of supported lipid layers on the hydrophobic graphene are still under debate. Both lipid monolayer and bilayer formation have been reported [120–123]. In SECTION 5.3 X-ray reflectometry data is presented, which provides direct structural evidence for the lipid monolayer formation on graphene. Reflectometry has been used successfully for decades for analyzing the structure of supported lipid layers going from simple to more and more complex systems, as explained in more detail in CHAPTER 2. This technique becomes even more relevant for lipid layers on graphene as a characterization of the layer on the graphene by fluorescence microscopy is not possible. Fluorescently labeled lipids remain dark on graphene. Apparently, the fluorescence of the dyes is quenched, as expected for a surface with metallic character [124]. Nevertheless, in very few reports fluorescence measurements of fluorescently labeled lipid layers on graphene are reported [120, 121]. These measurements of fluorescence could be related to transfer residues, which increase the separation between the fluorescence dye and the graphene, thus reducing the quenching effect [123, 125]. The lipid monolayer formation is verified by the results of specifically designed lipid spreading and electrochemical impedance spectroscopy (EIS) experiments, which are presented in SECTION 5.3 as well.

In SECTION 5.6, the electrostatic screening of electrolyte ions is quantified and an electrostatic model is derived and validated using the

structural information from XRR. We demonstrate the detection of cationic lipids by self-exchange of lipids with SGFETs. Furthermore, the observation of the formation of charged lipid layers on SGFETs in real time is shown. None of the published studies used graphene SGFETs to monitor the formation of lipid layers, although it is a key question of fundamental interest [126]. For instance, SGFETs could allow the study of single vesicle adsorption and spreading. This label-free detection of single lipid exosome adsorption and spreading is of great interest for cancer diagnostics [127]. Furthermore, SGFETs allow measuring the kinetics of layer formation induced by vesicle fusion or spreading from a reservoir. Characteristic conductance spikes that can be attributed to bouncing-off events of lipid aggregates from the SGFET surface are observed. The ability to see these spikes demonstrates a high potential of graphene SGFETs to measure the on-off kinetics of small aggregates interacting with supported lipid layers.

5.2 GRAPHENE

5.2.1 *Overview*

Graphene is a two-dimensional layer of carbon atoms arranged in a hexagonal lattice. In 2004, A. Geim and K. Novoselov isolated single layers of graphene by mechanical exfoliation, also famously known as the Scotch tape method, and characterized it electrically [128]. They were awarded the Nobel Prize in 2010 for their discovery [12]. Long before its first successful isolation, graphene or single layers of graphite have been the subjects of many investigations. Its band structure was described already in 1947 [129]. Graphene has no band gap, the charge carrier mobility is extremely high, and it is highly transparent for optical light [130]. These are just some of the reasons for why graphene is of such a high interest for many researchers. This chapter of my thesis mainly focuses on the resolving of the structure of lipid layers on graphene. A good introduction to the research on graphene, its properties and applications can be found in the review of Ferrari et al. [131].

5.2.2 *Fabrication and transfer*

Mechanical exfoliation produces graphene of highest crystal quality [132], but the size of the graphene is limited to patches of typically around $100\,\mu m^2$ [133] and the method hardly automatable. Other methods that allow producing larger areas of graphene have their drawbacks, e.g., in rather low mobility (liquid exfoliation of graphene oxide and reduction and liquid-phase exfoliation) or the strong electrical coupling to the substrate and the bad transfer to other substrates (epitaxial graphene). Ferrari et al. [131] also provide a good

overview of further fabrication methods. The graphene used in this thesis was grown on copper foil by chemical vapor deposition (CVD), so only this fabrication method will be discussed in more detail in the following. Graphene produced by CVD has two important properties that allow for the building of graphene transistors as biosensors. First, CVD graphene has decent charge carrier mobilities ($> 1000\,cm^2V^{-1}s^{-1}$) and second it is transferable to various substrates. CVD allows growing single-layer graphene up to several cm^2 with low content of multilayer areas [134]. In the following, a short description of the production of the graphene that was used in this thesis is given. A more detailed description and all parameters for the CVD process can be found in the paper from Blasche et al. [135]. An electropolished (to reduce the roughness) copper foil is exposed to a mixture of argon, methane, and hydrogen at different temperatures (heat up and annealing phase, growth and cool down) and pressures resulting in mainly single-layer graphene growth on the copper foil. The growth of small bilayer regions is observed. For most applications including SGFETs it is necessary to transfer the graphene to insulating substrates. For the transfer, the copper foil is removed from the growth reactor, and a polymer is spin coated on the graphene. Afterwards, the sample is placed in an etching solution to etch the copper. After copper etching is completed, the graphene/polymer film is placed in deionized water (DI) to remove residuals from etching. Subsequently, the graphene/polymer film is fished on a piece of SiO_2 or sapphire, a so-called die. As the last step, the polymer is removed with organic solvents. More detailed information on the growth of graphene can be found in the review from Li et al. [136].

5.3 STRUCTURAL ANALYSIS OF LIPID LAYERS ON GRAPHENE BY X-RAY REFLECTOMETRY

5.3.1 *Data and data analysis*

The XRR measurements were performed on the Mo-anode-based in-house reflectometer. A detailed description of the setup is given in CHAPTER 4. A measurement probes an area of around $8\,mm \cdot 15\,mm$ due to the large illumination spot by the incoming beam at low angles of incidence. The specular reflection of X-rays contains information about the SLD profile normal to the surface. The q range covered in the measurement extends up to $q_{max} \approx 0.5\,Å^{-1}$, which implies that the scattering length density distribution can be decomposed with a resolution of approximately 6 Å according to Fourier sampling theory [107].

In order to disentangle the different surface layers, the following XRR measurements of the same sample were performed. For all figures in

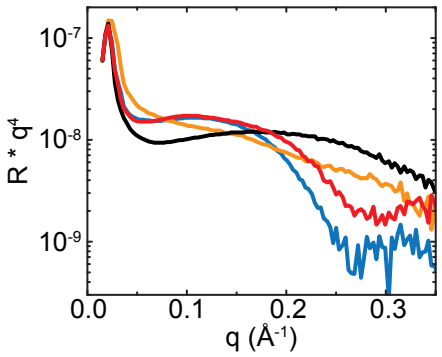

FIGURE 5.1: SUPERIMPOSED DATA OF THE CONSECUTIVE REFLECTIVITY MEASUREMENTS. A superposition of the reflected intensities of the bare substrate (orange), after graphene transfer (black), after DOTAP lipid layer deposition (red) and after self-exchange of POPC into the DOTAP layer (blue). Intensities are divided by the Fresnel reflectivity q^{-4}. All measurements performed in PBS buffer.

this chapter, the color code is identical. The corresponding color is shown in brackets.

- Bare Si substrate including its SiO_2 layer of around 200 nm thickness (**orange**).
- After graphene transfer (**black**).
- After formation of a DOTAP layer (**red**).
- After POPC insertion into the DOTAP layer (**blue**).

All measurements were carried out in phosphate buffered saline (PBS) buffer. For a detailed description of the sample preparation, please refer to SECTION 5.3.2 and to APPENDIX A.1. Performing these consecutive experiments is essential to provide proper reference measurements that allow for modelling of the X-ray intensities due to the layered SiO_2/graphene/lipid layer structure. FIGURE 5.1 shows a superposition of the recorded reflected intensities divided by the Fresnel reflectivity q^{-4}.

After the graphene transfer, the X-ray reflectivity curve shows a significant difference compared to the bare SiO_2 substrate. This underlines the sensitivity of the reflectometry measurements towards the graphene transfer. After depositing the DOTAP lipids, an even stronger change indicates the formation of a lipid layer. The recorded signal changes further after incorporation of POPC lipids, but it can be seen that the characteristics of the reflectivity curve of DOTAP layer are similar to the one of the DOTAP/POPG layer.

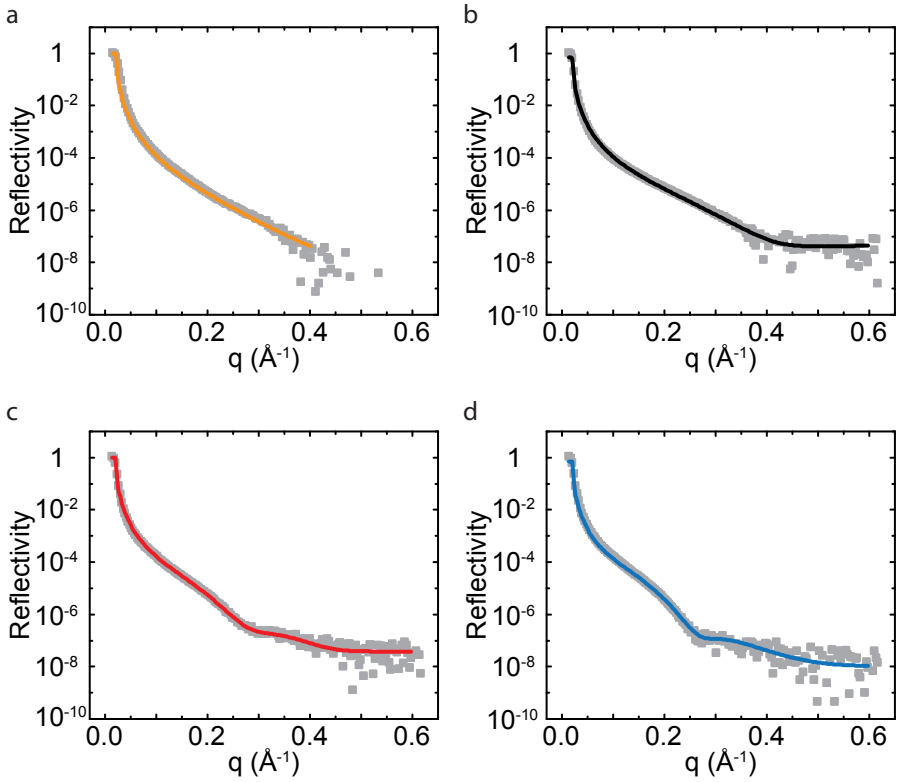

FIGURE 5.2: DATA AND MODELLING FOR ALL REFLECTIVITY MEASUREMENTS. Normalized X-ray reflectivity data (grey squares) and simulated intensities (solid lines) **a** for the Si wafer with SiO_2 layer, **b** after the graphene transfer, **c** with a DOTAP layer and **d** after POPG insertion.

The data was analyzed using MOTOFIT [111]. The minimal model to reproduce the data was always chosen. The program uses n numbers of discrete layers with constant SLD and thickness, the so-called boxes, to describe the system. At the interface of two adjacent boxes, an error function takes the roughness into account. The program converts the modeled SLD profile to a theoretical reflectivity curve using the Abeles formalism [113] (see CHAPTER 3 for more details). This theoretical reflectivity curve is then fitted to the data. The modelling yields the values of the thickness, roughness and SLD value of each layer. Models were iteratively applied to all four reflectivity curves to identify a consistent structure model in accordance with the data. The fits, shown as solid lines in FIGURE 5.2 are all in good agreement with the experimental data. The reflectivity data are shown as grey rectangles. The SLD profiles of the first three measurements are presented in FIGURE 5.3.

For the bare wafer, the fit reveals a roughness of 4.05 Å for the 200 nm thick oxide layer while the SLD of SiO_2 is $18.7 \cdot 10^{-6}$ Å^{-2}. The data recorded after the graphene transfer can be reproduced by one additional layer. Its thickness was determined to be 12.59 Å with a rough-

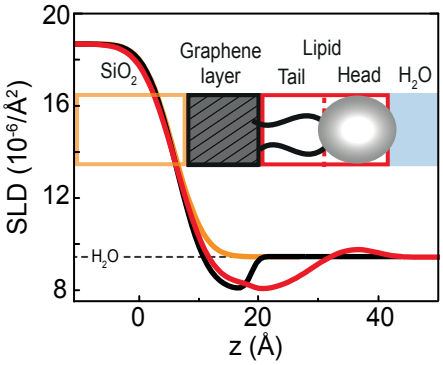

FIGURE 5.3: SLD PROFILES OF A SI DIE WITH SiO_2 LAYER, AFTER THE GRAPHENE TRANSFER AND WITH A DOTAP MONOLAYER. ADAPTED FROM [119].
Scattering length density depth profiles used to calculate the simulated intensities, same color code as in 5.2. The dashed line indicates the scattering length density of water.

ness of 1.11 Å and a SLD of $8.2 \cdot 10^{-6}$ Å^{-2}. The thickness is in good agreement with results of AFM measurements [137, 138]. These values indicate that the graphene is not entirely flat and might contain transfer residues [138]. All parameters used for modelling the data can be found in TABLE 5.1 at the end of this chapter.

To model the reflectometry data of the DOTAP layer, three layers on top of the Si/SiO_2 substrate were needed. In the modelling, a lipid monolayer requires one layer for the lipid tails next to one layer for the lipid head groups. Densely packed lipid tails have a SLD lower than the SLD of water ($SLD_{Water} = 9.45 \cdot 10^{-6}$ Å^{-2}). The lipid head groups have a SLD higher than water [35]. Note that the actual SLD, i.e. the electron density, of lipid tails and head groups varies linearly with the packing density of the lipids and the system's roughness. Only models where the hydrophilic lipid head groups face towards the buffer were considered. The SLD of water is shown as a reference (dashed line) in FIGURE 5.3. After the deposition of the lipid layer the thickness of the layer adjacent to the silicon oxide was fitted to be 12.66 Å with a roughness of 1.11 Å and a SLD of $8.28 \cdot 10^{-6}$ Å^{-2}. This is in good agreement with the values of the graphene layer of the measurement without lipids. Next to the graphene, a second layer with thickness of 9.92 Å, a roughness of 4.47 Å and a SLD of $7.99 \cdot 10^{-6}$ Å^{-2} and a third layer with thickness of 10.54 Å, a roughness of 2.71 Å and a SLD of $9.93 \cdot 10^{-6}$ Å^{-2} are present. The last two layers represent lipid tails and heads, respectively. Thus, the XRR experiments confirm the formation of a 20.5 Å thick DOTAP monolayer on graphene.

In FIGURE 5.4 the SLD profile of the lipid layer that formed after POPG incorporation to the DOTAP layer is compared to the SLD profiles of the first three measurements. The SLD profiles of the DOTAP mono-

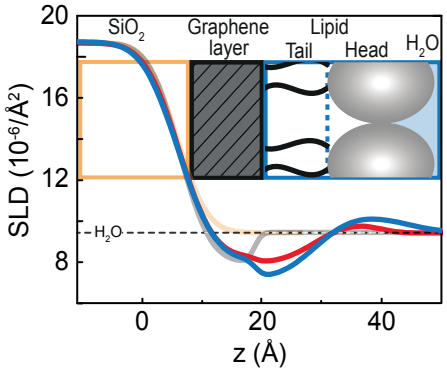

FIGURE 5.4: COMPARISON OF THE SLD PROFILES OF THE DOTAP MONOLAYER AND THE DOTAP/POPG MONOLAYER. ADAPTED FROM [119].
Scattering length density depth profile used to calculate the simulated intensities of the lipid layer after POPG incorporation compared to the one of the DOTAP monolayer. The dashed line indicates the scattering length density of water. Color code as in 5.2.

layer and of the DOTAP/POPG layer are highlighted. The protocol for the deposition of the POPG lipids can be found in APPENDIX a.1.4. The modelling reveals that the monolayer structure is preserved after adding the POPG lipids. The illustration in FIGURE 5.4 shows the different layers of the DOTAP/POPG monolayer. Lower SLD values for the tail region ($7.16 \cdot 10^{-6}$ Å^{-2}) and higher SLD values for the lipid head region ($10.26 \cdot 10^{-6}$ Å^{-2}) of the DOTAP/POPG layer than for the DOTAP layer suggest that the lipid monolayer is denser packed after incorporation of the oppositely charged lipids. The thickness of the lipid layer is 22.4 Å.

5.3.2 *Experimental details*

5.3.2.1 *Sample chamber*

FIGURE 5.5 shows a schematic of the sample chamber that was used for the XRR measurements presented in this chapter. It is a slightly modified version of a sample chamber our group previously reported about [139]. The dispensable material of the microfluidic chambers (μ-Slide I Luer, channel height 0.8 mm) in the beam path was milled out. Additionally, a notch for the die was milled. The die (wafer purchased from MicroChemicals GmbH, Ulm, Germany, with an oxide layer of 200 nm and size of 15 mm · 20 mm · 0.7 mm) was glued (Microset 101RF, Microset, Leicestershire, UK) to the chamber.

5.3.2.2 *Measurement details*

Experiments were performed as $\theta - 2\theta$ scans of sample and detector angle, background measurements with an offset for θ of $-0.05°$ and

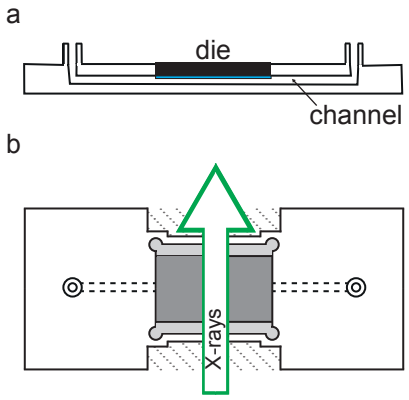

FIGURE 5.5: SCHEMATIC OF THE SAMPLE CHAMBER USED FOR THE XRR MEASUREMENTS. **a** Side view including Si die (black) with SiO_2 layer (blue). **b** Top view, notch for die (grey), direction of X-ray beam (green) and material that was milled out (dashed grey) is sketched.

corrected for by subtraction. As described by Salah et al. [118], the effective beam height was corrected by

$$I_{corr} = I_{exp}\theta_{so}/\theta \quad . \tag{5.1}$$

The corrections were applied below the spill-over angle

$$\theta_{so} = \arcsin(d_{en}/l) \quad , \tag{5.2}$$

i.e. the angle for which the complete sample in the scattering plane is illuminated by the full beam height. d_{en} is the slit opening and l the length of the sample in the scattering plane. The intensity of all measurements was normalized to 1 and converted to momentum transfer by $q = 4\pi/\lambda sin(2\theta/2)$. An introduction to the theory of reflectometry can be found in CHAPTER 3.

5.4 LIPID SPREADING ON GRAPHENE

5.4.1 *Lipid spreading on a macro scale graphene SGFET*

To investigate if lipids can spread on graphene, lipid spreading from a reservoir on graphene was studied. DOTAP lipids were stamped into one corner of a millimeter-sized graphene SGFET (channel dimension W = 2 cm, L = 1 cm). After stamping, buffer solution was added and the transistor transfer curves shown in FIGURE 5.6 A were recorded with evolving time. Details about preparing the stamp can be found in APPENDIX A.1. Already within a very short time after stamping a second minimum in the current-voltage curve can be observed at around -0.2 V. This is expected from a partially lipid covered transistor where a certain part of the graphene has a shifted charge neutrality point (CNP). With evolving time, the two minima converged

two a single, yet broad minimum around 0 V. This indicates increasing coverage of the active area of the graphene transistors with lipids; consequently, this confirms that lipids can spread on graphene, as indicated in the inset in FIGURE 5.6. The overall shift of around −200 mV is comparable to microscale SGFETs and cyclic voltammetry (CV). The shift of the second minimum from around −0.2 V towards 0 V is tentatively attributed to a reduction of the stamped lipids reservoir and a corresponding reduction of positive charges next to the graphene in this area.

5.4.2 *Lipid spreading on a SiO_2 substrate patterned with graphene obstacles*

Since spreading lipid layers do not cross hydrophobic/hydrophilic borders [34, 37], as depicted in FIGURE 5.7 A, the here presented experiment can give further insight into the lipid structure on graphene. To provide further evidence on the lipid monolayer structure on graphene, spreading experiments on SiO_2 patterned with graphene barrier structures were performed. For further information about lipid spreading, please refer to CHAPTER 2. FIGURE 5.7 B shows a schematic of the experiment. DOTAP lipids were stamped on a silicon dioxide surface. After addition of buffer, a lipid bilayer spreads on the surface [37]. Graphene domains forming rectangular obstacles are located on the SiO_2. The bold black regions in panel 1 of FIGURE 5.7 B correspond to the graphene domains and the inner white regions correspond to the SiO_2 domains. In FIGURE 5.7 B, panels (2) to (4) show fluorescence images of the spreading process. First, the lipid bilayer spreads evenly across the SiO_2 surface (2), as observed previously [34]. The lipids also spread through the SiO_2 channels formed in between the graphene obstacles, leading to a curved lipid front (3). Finally, the lipid front leaves the graphene obstacles behind; a continuous straight lipid front is visible again (4). Since no fluorescence was observed in the inner regions of the graphene domains, where a SiO_2 surface is exposed, we can conclude that the bilayer lipids do not spread across the graphene/silicon dioxide border in agreement with previous reports [140]. These findings underline the hydrophobicity of graphene structures on silicon dioxide [141] and support the results of the reflectometry measurements.

5.5 ELECTROCHEMICAL CHARACTERIZATION OF LIPID LAYERS ON GRAPHENE

5.5.1 *Electrical impedance spectroscopy*

The current response of a system to an externally applied voltage is measured with EIS. It is a prominent technique to study the mate-

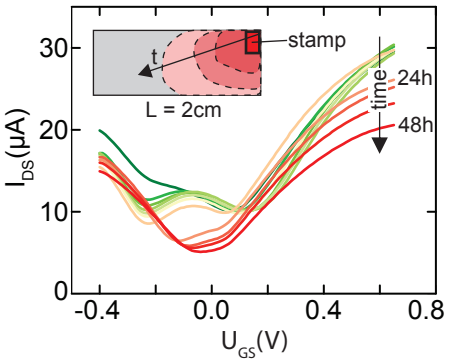

FIGURE 5.6: LIPID SPREADING ON GRAPHENE. ADAPTED FROM [119].
Time evolution of transfer curves (U_{DS} = 100 mV) of a macro scale graphene SGFET after stamping of lipids into the corner of the approximately 2 cm long channel region.

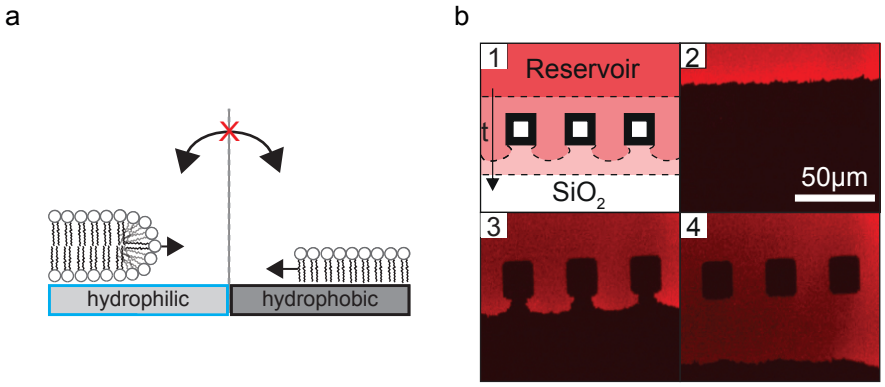

FIGURE 5.7: SPREADING OF LIPIDS ON A SiO_2 SUBSTRATE PATTERNED WITH GRAPHENE OBSTACLES. ADAPTED FROM [119].
a Spreading lipid layers do not cross hydrophobic/hydrophilic borders. **b** Spreading of lipids on a SiO_2 substrate patterned with graphene lines forming square obstacles. The scheme (panel 1) shows the front of the bilayer for increasing time (dashed lines). Panels 2-4 are fluorescence microscopy images at different times. Red fluorescence indicates the presence of the 0.5 % Texas Red labeled bilayer. Note that the SiO_2 patches inside the graphene frames remain uncovered, i.e. the bilayer does not cross the graphene barriers.

rial/electrolyte interface. It allows, e.g., to study biological systems and materials in their natural environment [6] and the ionic transport through as well as the dielectric properties of lipid bilayer membranes containing functional proteins [142, 143]. A sinusoidal potential U(t) is applied to the working electrode. This results in a response of the current I(t) across the graphene/electrolyte interface. The impedance Z is defined by

$$Z = |Z|e^{i\phi} = |Z|(\cos(\phi) + i\sin(\phi)) = \frac{U}{I} = \frac{|U|e^{i\omega t+\phi U}}{|I|e^{i\omega t+\phi I}} \quad . \quad (5.3)$$

Phase and magnitude of the impedance can be modeled using an appropriate equivalent circuit model. Equivalent circuit models try to approximate the electrical characteristics of a given system using basic electrical components [144]. Fitting can determine the values of these components, so they reproduce the frequency dependence of the phase and the magnitude of the impedance as good as possible. FIGURE 5.8 shows the complex electrical impedance $|Z|$ and phase angle ϕ of a bare graphene electrode (black) and with a DOTAP layer (red).

The capacitance of the graphene/electrolyte interface estimated from the fitting based on an equivalent circuit is in good agreement with literature [145–147]. The behaviour after the formation of the DOTAP layer can be attributed to a lipid layer on top of the graphene [148, 149]. The choice of the elements of the equivalent circuit to model the EIS data recorded after lipid formation was based on the results of the XRR measurements. A lipid layer capacitance of $3\,\mu F/cm^2$ is obtained. This value is higher than the expected value $1\,\mu F/cm^2$ for a lipid double layer and thus is a strong indication that the layer is a monolayer.

5.6 LIPID LAYERS ON GRAPHENE TRANSISTORS

5.6.1 *Graphene solution-gated field-effect transistors as biosensors*

Graphene SGFETs represent a promising biosensing platform. Their high transconductance and low intrinsic electronic noise result in high signal-to-noise ratio (SNR) [150]. Additionally, they provide excellent time resolution [151, 152] operating up to the MHz regime. They are stable in electrolyte environments [153, 154] and there are established surface functionalization schemes [155]. Graphene SGFETs have been used for recording of cell action potential [135, 156–158], and brain activity [159, 160], and for the detection of analytes such as neurotransmitters [161], DNA [152, 162] and prostate-specific antigen [163]. They also hold great potential to study supported lipid layers

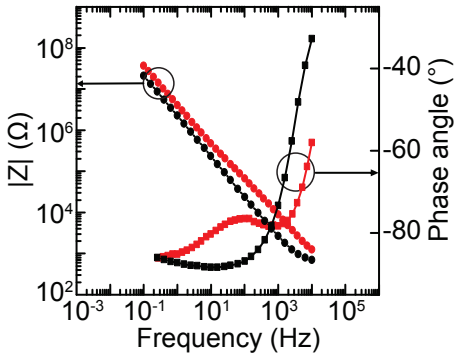

FIGURE 5.8: EIS MEASUREMENT OF GRAPHENE BEFORE AND AFTER FORMATION OF A DOTAP MONOLAYER. ADAPTED FROM [119].
Electrical impedance showing magnitude (circles) and phase (squares) of graphene before (black) and after formation of a DOTAP layer (red) (U = 400 mV vs. Ag/AgCl).

[123] as also shown in this chapter. For an introduction to fabrication, working principle, and ion sensitivity model of graphene SGFETs please refer to APPENDIX B.1.

5.6.2 *Static characterization*

The black curve in FIGURE 5.9 shows a transfer curve of a graphene transistor recorded at U_{DS} = 100 mV. It shows the typical characteristic V-shape of ambipolar graphene devices (see APPENDIX B.1.2 for more information). The CNP voltage U_{CNP} was shifted to 0 V. Figure 5.9 as well shows the effect of charged lipids on the CNP. After deposition of a cationic DOTAP layer, the U_{CNP} shifts to negative U_{GS} values (red transistor curve). This shift is in agreement with previously reported values [120] and also with the cyclic voltammetry measurements presented in [119]. The transistor curve (blue) shifted towards more positive values after anionic POPG vesicles were injected in order to allow for self exchange. The structure of the DOTAP/POPG layer is analyzed in SECTION 5.3. The negatively charged lipids could not be deposited on the graphene by vesicle fusion at zero bias. This can be due to the negative surface charge of graphene [150] preventing the formation of a negatively charged lipid layer due to electrostatic repulsion [164]. With a negative gate voltage it was possible to deposit the POPG layer on the graphene transistors, U_{CNP} shifts to positive values (green transistor curve), in agreement with previously reported results [120]. No significant shifts were observed for zwitterionic POPC lipids (data not shown).

To assess the surface charge of the lipid layers, also the ion sensitivity of graphene SGFETs was investigated. It is influenced by charges at the graphene/electrolyte interface, for more details about the model

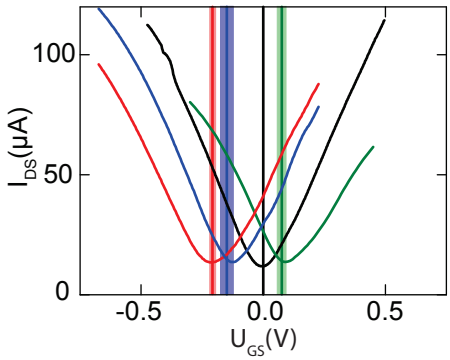

FIGURE 5.9: TRANSISTOR CURVES OF A BARE GRAPHENE SGFET, AND COVERED WITH A DOTAP, A DOTAP/POPG AND A POPG LAYER. ADAPTED FROM [119].
Exemplary transistor transfer curves (I_{DS} - U_{GS}) of bare graphene SGFET (black), and covered with DOTAP (red), DOTAP/POPG (blue) and POPG (green) monolayer. The vertical lines indicate the averaged charge neutrality point (CNP) voltage U_{CNP}, i.e. the voltage at minimum current. The colored areas indicate the standard deviation.

please refer to APPENDIX b.1.3. FIGURE 5.10 A shows the normalized shift of the charge neutrality point ΔU_{CNP} as a function of the ion concentration for bare graphene transistors (black) and transistors with a POPG monolayer (green). For bare graphene transistors, a shift of the CNP towards negative voltages for increasing sodium chloride concentration was observed. With a POPG monolayer the average ion sensitivity increased. FIGURE 5.10 B shows the normalized position of the charge neutrality point as a function of the salt concentration for a transistor with a DOTAP (red) and a DOTAP/POPG (blue) monolayer. The one for a bare graphene transistor is again shown in black. The positively charged DOTAP lipids are expected to (over)compensate the negative surface charge, and the ion sensitivity is expected to vanish or even inverse its sign. In fact, a slight upshift of the CNP upon increasing salt concentration is observed. The change in surface charge is in reasonable agreement with the experimentally measured surface charge of positively charged 1,2-dipalmitoyl-3-trimethylammonium-propane (DPTAP) lipids [165]. Note that the measured surface charge is significantly lower than a simple estimation based on one positive charge per lipid, i.e. per 0.9 nm^2, since ion-ion interactions have to be considered. Consequently, a hypothetically reduced packing density of DOTAP lipids might have a negligible effect. Adding anionic POPG lipids increased the ion sensitivity again. This increase indicates the deposition of negative charge at the graphene surface. Possible mechanisms are either the formation of a POPG layer upon the DOTAP monolayer or the incorporation of POPG lipids into the DOTAP layer. The XRR measurements presented in SECTION 5.3 show that the monolayer structure is preserved and no floating bilayer forms after adding POPG lipids. This result is supported by the observed complete recovery of the ion sensitivity.

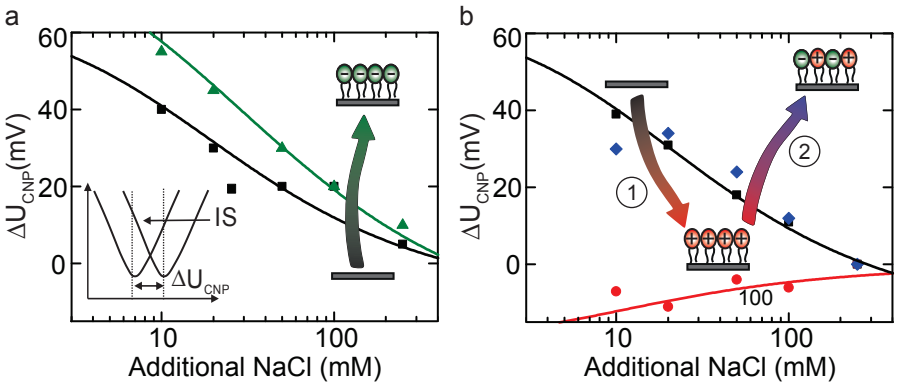

FIGURE 5.10: ΔU_{CNP} OF A BARE GRAPHENE SGFET AND WITH LIPID LAYERS FOR INCREASING IONIC STRENGTH. ADAPTED FROM [119].
a Shift of U_{CNP} (ΔU_{CNP}) of a graphene SGFET for increasing ionic strength (IS) in bare state and with a POPG layer shown as black squares and green triangles. The sequence of exposure to lipid vesicles for spreading and self exchange is indicated by the arrow. The inset shows exemplary transistor transfer curves for low and high ion concentration. **b** Shift of U_{CNP} (ΔU_{CNP}) for a bare transistor (black squares), after DOTAP layer deposition (red circles) and after self exchange with POPG vesicles (blue diamonds). Solid lines represent model fits. All ion sensitivity experiments were performed in 5 mM PBS buffer.

Based on these findings, surface charge and screening effects are proposed as an explanation for the changed ion sensitivity of DOTAP layer covered graphene SGFETs. A previous report suggested complete insulation of the graphene from the electrolyte by a lipid membrane [121] to explain the vanishing ion sensitivity. However, perfect insulation is very unlikely due to the defectiveness of supported lipid layers [166], especially in the case of millimeter-scale transistors used by Wang et al. [121]. Furthermore, such insulation could only explain the reduced ion sensitivity for DOTAP covered transistors, but not the increased sensitivity for POPG covered transistors. Besides, the increased ion sensitivity after incorporation of POPG lipids into the DOTAP layer is a strong argument supporting that the observed ion sensitivity is related to surface charge and screening and not due to the insulation induced by the lipid layer.

5.6.3 *The dynamics of the formation of lipid layers on graphene*

The dynamics of the lipid layer formation on graphene SGFETs was also investigated. First, sonicated DOTAP vesicles were incubated on graphene SGFETs. The transistor curves measured with evolving time (up to four hours) after vesicle fusion was induced by osmotic shock (see CHAPTER 2 for more details) are shown in FIGURE 5.11 A. A second CNP starts to form. Transistor curves with two pronounced CNPs were

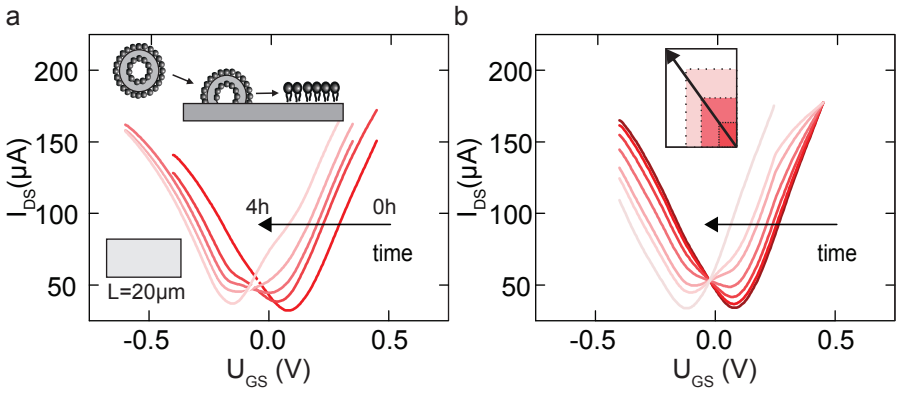

FIGURE 5.11: EVOLUTION OF TRANSISTOR TRANSFER CURVES WITH TIME DURING THE FORMATION OF A DOTAP MONOLAYER. ADAPTED FROM [119].
a Evolution of the transistor transfer curves (U_{DS} = 100 mV) with time during the formation of a DOTAP lipid layer by vesicle fusion as sketched in the inset. **b** Calculated transfer curves from the three-part model.

measured until the first CNP vanished almost completely. After completion of the layer formation only one major CNP (pink), shifted with respect to the original one, was measured. A simple three-resistor network consisting of a lipid-covered area increasing with time in parallel with an uncovered region and an uncovered region in series can closely reproduce the evolution of the transistor transfer curves, see FIGURE 5.11 B.

Furthermore, the drain-source current was measured with fixed gate voltage and drain-source voltage while 23 transistors were exposed to a solution of extruded DOTAP lipid vesicles (200 nm nominal pore size, see APPENDIX a.1 for more details on vesicles sizes). FIGURE 5.12 A shows the recorded drain-source current as a function of time. The green vertical line indicates the time when the lipid vesicle solution is added. For all transistors, the transistor current increases simultaneously. This indicates a high tension of the freshly extruded lipids that spread almost instantly on the device surface. As the coverage of the active transistor area with the positively charged lipid layer increases, the drain-source current increases further. The spreading process is qualitatively similar for all transistors, with comparable spreading time, if freshly extruded lipids were used. This is not the case for lipid vesicles stored for several weeks. FIGURE 5.12 B shows corresponding measurements with sonicated vesicles that were stored for several weeks; the lipid solution is added at t = 0 s and the result for five representative transistors is shown. In contrast to the measurements with freshly extruded lipids, the drain-source current does not increase instantly. This indicates a lower fusogenicity of the stored lipid vesicles compared to the freshly extruded. The spreading process starts at different times for different transistors, and duration and

speed vary from transistor to transistor. This different response of the transistor can be attributed to changes in the lipid vesicle with storage time [167]. FIGURE 5.12 C shows another experiment with stored lipids using a higher sampling rate. The green vertical line indicates the adding of the lipid solution. Three different time regions are indicated, before (1), during (2) and after (3) lipid layer formation. Interestingly, pronounced current fluctuations are visible during layer formation. A zoom-in on the recorded current of the transistor, before (1), during (2) and after (3) lipid layer formation is shown in FIGURE 5.12 D. During the time of the formation of the lipid layer, "up and down states" in the current are observed. No time correlation between the up and down state of different transistors was observed. These states can tentatively be attributed to the adsorption and desorption of lipid aggregates as sketched in the inset of FIGURE 5.12 D.

5.7 CONCLUSION AND OUTLOOK

In this chapter, the structure and formation dynamics of lipids on graphene produced by CVD were investigated. As shown in CHAPTER 2 lipids tend to form monolayers on hydrophobic substrates. Here, X-ray reflectivity measurements are presented, which clarify that this is also the case on graphene on SiO_2. Performing consecutive experiments, starting from the bare substrate, was the key to determine the monolayer structure. The SLD profile resulting of the modelling of the data of the DOTAP measurement alone could be wrongly interpreted as a lipid double layer since the graphene layer and the lipid headgroup region have similar SLD value and thickness. Lima et al. as well highlight the importance of consecutive measurements to avoid misinterpretation in their report about the investigation of the lipid formation on graphene with ellipsometry [137]. For graphene, recent measurements also suggest the formation of a lipid monolayer, based on quartz crystal microbalance experiments [122]. The electrical characterization of the lipid graphene interface also points towards the formation of a lipid monolayer which mediates the capacitive coupling of the graphene electrolyte interface only weakly. This corresponds to the results of the XRR measurements as well as to the assumptions from the spreading experiments. Resolving the structure of lipids on graphene is a prerequisite for the future application of lipid decorated graphene SGFET biosensors. In this line, the influence of differently charged lipid layers on graphene transistors, especially on their ion sensitivity, were thoroughly discussed. The ion sensitivity upon lipid adsorption is modeled by the screening of surface charges. Furthermore, it was demonstrated that graphene transistors can be used to in-situ monitor the formation of lipid layers in real time and with high temporal resolution. Together with recent developments in the fabrication of nanoscale graphene transistors, this technology has

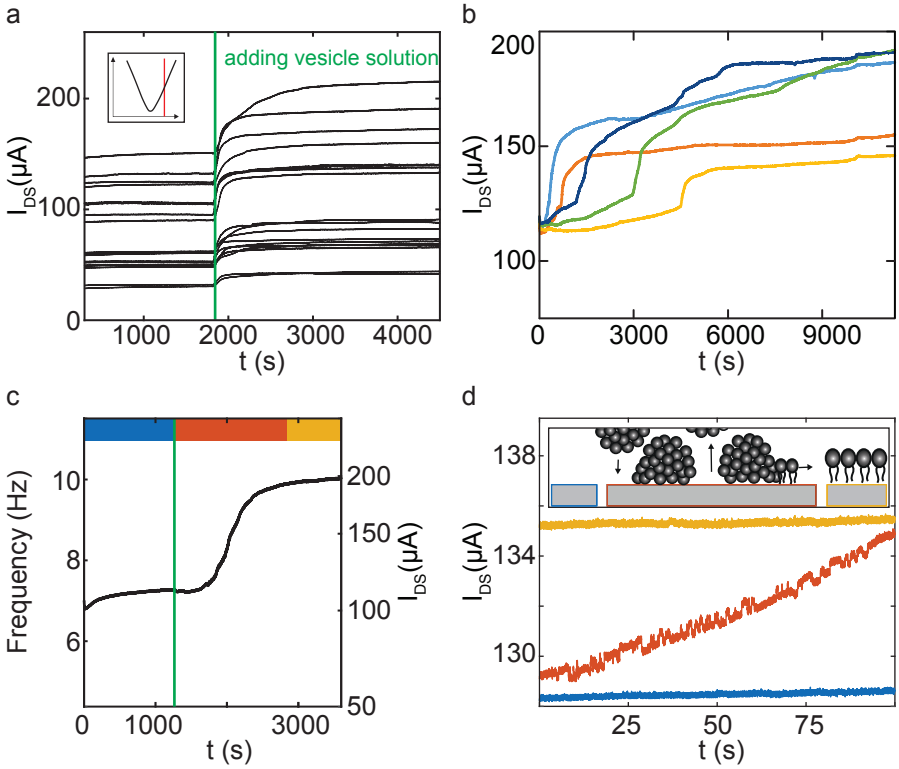

FIGURE 5.12: FUSOGENICITY OF DOTAP VESICLES. ADAPTED FROM [119].
a I_{DS} recording (U_{DS} = 100 mV, U_{GS} = 400 mV as indicated in the inset) of several transistors in parallel to analyze lipid layer formation from freshly extruded vesicles. The time point of adding lipid solution is indicated by green vertical line. **b** Parallel I_{DS} recording (U_{DS} = 100 mV, U_{GS} = 300 mV) of lipid layer formation with sonicated lipids stored for several weeks. Lipids were added at t = 0 s. **c** I_{DS} recording of lipid layer formation (U_{DS} = 100 mV, U_{GS} = 300 mV) with sonicated lipids stored for several weeks. The time point of adding lipid solution is indicated by the green vertical line. Time before (blue), during (red) and after lipid layer formation (yellow) is indicated. **d** Close-up of I_{DS} recordings from (c) before (blue), during (red) and after lipid layer formation (yellow). Curves were shifted vertically to allow for a better comparison.

a high potential for studying single vesicle adsorption and desorption. Furthermore, the diagnostics of exosomes, i.e. vesicles secreted by all cells and found in body fluids [168] holds great potential. Although the importance of exosomes is known, e.g., for non-invasive diagnostics of cancer [169], new tools to study them must be established. Graphene SGFETs can make valuable contribution in this field.

Layer description	**Thickness** (Å)	**Roughness** (Å)	**SLD** (10^{-6} Å^{-2})
Measurement 1: Si with 200 nm thick layer of SiO_2			
Si	-	4.07	19.8
SiO_2	2000	4.05	18.7
Measurement 2: after graphene transfer			
Si	-	4.05	19.8
SiO_2	2000	4.00	18.7
Graphene layer	12.59	1.05	8.15
Measurement 3: DOTAP monolayer			
Si	-	3.76	19.8
SiO_2	2000	4.53	18.7
Graphene layer	12.59	1.11	8.27
Lipid tail region	9.92	4.47	7.99
Lipid head region	10.54	2.71	9.93
Measurement 4: DOTAP/POPG monolayer			
Si	-	3.76	19.8
SiO_2	2000	4.71	18.7
Graphene layer	12.59	1.18	8.04
Lipid tail region	9.77	4.76	7.16
Lipid head region	14.84	4.96	10.26

Table 5.1: PARAMETERS FOR MODELLING THE REFLECTIVITY DATA.
Parameters used for modelling the reflectivity data of the bare SiO_2 substrate, after graphene transfer, the DOTAP monolayer and the DOTAP/POPG monolayer.

Part IV

A NEUTRON AND X-RAY REFLECTOMETRY STUDY OF THE INTERFACE BETWEEN ADHERING CELLS AND SOLID SURFACES

6

A NEUTRON AND X-RAY REFLECTOMETRY STUDY OF THE INTERFACE BETWEEN ADHERING CELLS AND SOLID SURFACES

6.1 INTRODUCTION

Cellular adhesion is a fundamental process of life, and no animal life would exist without the ability of cells to build a three-dimensional tissue. The composite membrane of the cell mediates the adhesion. In a simplified model, the composite membrane can be regarded as an organized layered arrangement of molecules. The primary structural confinement unit of the composite membrane is the lipid bilayer - the "natural" structure that membrane lipids form in an aqueous environment. Membrane proteins, embedded in this two-dimensional matrix, enable transport and signalling across the cell wall. On the intracellular side of this lipid bilayer, actin filaments form a cortex, ensuring flexibility and mechanical stability of the bilayer. Glycoproteins form the glycocalyx that covers the extracellular side of the cell membrane. Since the composite membrane, as well as the ECM, is built of molecules and proteins, the important structural features of cell adhesion are in the nanometer and even subnanometer scale. The ECM in animals is regulated by the cells embedded in it. The ECM molecules are mainly produced locally by the cells [33], they create their chemical and mechanical surrounding as well as shape the ECM by applying force [170].

Epithelial cells adhere to the basal membrane, a thin, planar layer composed of extracellular matrix proteins, which supports all epithelia, muscle cells, and nerve cells. The basal lamina is composed of a homogeneous, macromolecular network formed mainly by collagens of type IV. The specific adhesion of the epithelial cells on the basal membrane is controlled by lock-and-key forces formed between CAMs such as integrins exposed by the cell plasma membrane and specific ligands exposed by the basal membrane. They form specific links with the proteins of the basal membrane. On solid substrates, epithelial cells form their own basal membrane by protein deposition. Hence cell adhesion is modulated first, by nonspecific forces and the competition between short-range attraction lock-and-key forces and long-range repulsions mediated by glycoproteins of the glycocalyx.

In this context, the cell-substrate separation distance is an enduring matter of debate. For decades cell adhesion has been studied with

natural cells and biomimetic cell models adhering on solid substrates and, by using model systems like supported lipid membranes. When seeded on a substrate, specific cells like epithelial or nerve cells attach to it. This enables the use of a variety of structural analysis techniques to study living cells, e.g., at room or body temperature, and in an aqueous environment, as all of the techniques require a close contact of the cell to the substrate. It has been shown that cell adhesion can be understood as a first-order dewetting transition [75] regulated by a number of different factors like membrane elasticity [75, 77], receptor mobility [171], as well as a variety of short- and long-range nonspecific forces [75, 78, 79]. These nonspecific forces include attractive van der Waals and electrostatic interactions, repulsive undulation forces due to thermally excited flickering of the lipid protein bilayer and a manifold of polymer induced forces [75]. The polymers can apply strong repulsive forces between the adhering interfaces. Short range lock-and-key forces mediated by cell surface receptors are responsible for the specificity of the adhesion process [69, 75, 76]. Studies on thermally excited bending undulations of lipid vesicles show that the membrane switches between weak and strong adhesion states, suggesting that adhesion is determined by a double-well interfacial potential with minima at a short and a long distance (in the case of the lipid vesicle $h_{short} \approx 10\,nm$ and $h_{long} \approx 40\,nm$) [43, 81, 172, 173]. The wetting process results in the formation of adhesion domains, which allow cell adhesion at very low receptor densities. For immobile receptors, far less adhesion domains are observed [171]. It is assumed that they only can form if local clusters of receptors exist.

The majority of the structural studies on membranes on solid surfaces are single- or few-cell studies based on optical microscopy techniques [86, 89, 91, 92, 94–96, 101–103, 105], localizing the cleft thickness at around 10 - 100 nm. A more detailed introduction to the cell membrane, cell adhesion and analyzing techniques can be found earlier in this thesis in CHAPTER 2. Optical methods always encounter the problem that the real part of the refractive indexes of water and molecules hardly differ. Thus insight into hydration and hydration dynamics can only be provided using fluorescence. In the first instance, however, the wavelength λ of light in the visible range is large compared to the dimensions of lipid membranes and proteins, which are in nano- or subnanometer range and hence are difficult to resolve by optical microscopy.

X-ray reflectometry, for example, is better suited to analyze the structure of lipid bilayers at interfaces. However, also X-ray scattering is afflicted with the fact that the scattering length of water and polymers and proteins do not differ significantly hence leaving hydrated layers hardly visible. Furthermore, photochemical processes induced

by X-rays can cause beam damage and alter cell shape and behaviour. Neutron reflectometry is a powerful method for structural analysis of layered systems especially for soft matter systems [174, 175] with a resolution in the range in of a few nanometers, and under ideal experimental conditions even in the Å range. As neutrons interact with the nucleus of an atom, neutron scattering is sensitive to isotopic differences. For over 20 years neutron scattering has been intensively used to study model membranes and gained considerable expertise in this field. This is proven by the long list of publications, starting from structure determination of simple model systems like supported lipid bilayers composed of one kind of lipid [50], to more and more complex and realistic model membranes such as tethered SLBs [51]. Studies on the interaction of bilayers with peptides [55] or on layers with a realistic composure of lipids, extracted from bacteria [53], have also been presented. Furthermore, it has been shown that NR experiments with epithelial cells are possible [4].

In this chapter, the results of a neutron reflectometry investigation of epithelial cells that adhere to a SiO_2 surface are presented. The specular reflection of neutrons contains information about the SLD profile normal to the surface. NR lends itself to probing the buried interface between cells and a substrate. Neutrons, with a wavelength of a few Å, travel through silicon without large losses due to absorption. This helps us to study the solid/liquid interface efficiently. Furthermore, compared to X-rays, almost no photochemical processes are triggered. Still, the biggest potential of NR might lie in the sensitivity to isotopic differences. The huge difference between the SLDs of H_2O and D_2O enables determining the hydration and the water exchange of the different layers by contrast variation, i.e. varying the D_2O/H_2O ratio in the cell medium. Another important aspect is that the presented NR experiments probe an area of around $4\,\text{cm} \cdot 8\,\text{cm}$, i.e. of around 10^7 cells. A measurement averages over the dynamics and the structure of the cell layer. The earlier mentioned experiments with optical microscopy mostly are single- or few-cell studies. Epithelial cells behave differently when isolated than in their native confluent environment. Besides higher statistics, this makes a good case for performing measurements on a confluent layer rather than doing single-cell experiments.

We aim to answer the following questions:

Is it possible to gain further insight on cell adhesion by exploiting the unique properties of neutron reflectometry? Can the distance of the composite membrane to the substrate and the SLD profile, the hydration and the water exchange in the region between the substrate and a confluent layer of adherent cells be resolved? Are the

results in agreement with the theory of cell adhesion?

In the following, the results of NR measurements in a total of six different contrasts are presented. The maximal number of varied contrasts on the same cell layer was five. The successful execution of contrast variation measurement on living cells demands specific requirements on the design of the sample environment. The development of a sample chamber providing all necessary features was indispensable. Its design is shown in SECTION 6.3. By varying the contrast of the cell medium, we found an approximate model that fits the data within the framework of cell adhesion presented in more detail in CHAPTER 2. The results are interpreted as the average cell substrate density profile from a large ensemble of living cells. A three-layer interfacial organization is suggested. It consists of a very dense, 70 – 120 Å thick, protein film bound to the silicon surface interface, followed by a highly hydrated 180 – 280 Å thick layer. The third, several hundred Å thick layer is attributed to the less hydrated composite membrane. It further is suggested that the bottom dense protein layer is formed by the cells to generate a bioanalogue tissue film. Contrast variation allows us to resolve the hydration and the water exchange in the layers. A living cell is much more complex and especially more dynamic than a model system. In this respect data analysis involves approximations which will be explained in detail in the next sections.

6.2 NEUTRON INSTRUMENTS

In this thesis, neutron reflectometry experiments were performed on the following three instruments:

REFSANS

A horizontal time-of-flight reflectometer operated by the Helmholtz Zentrum Geesthacht at the Heinz Maier-Leibnitz Zentrum in Munich (Germany) [176]. It was designed for specular reflectometry and grazing incidence neutron scattering studies. The horizontal geometry allows probing the liquid/air interface. The sample chamber and the measurement procedure was developed on REFSANS. Successful contrast variation measurements were performed. In the experiments, the incident wavelength spectrum ranged from λ = 2 - 10 Å with a wavelength spread $\Delta\lambda/\lambda$ = 0.05. Four different angles were measured (θ = 0.3°, 0.6°, 1.2° and 2.4°). The slit settings were chosen so that the sample surface was not over-illuminated at each incidence angle. Data and modelling are shown in SECTION 6.5.

MARIA

A vertical reflectometer operated by the Jülich Centre for Neutron Science (JCNS) at the Heinz Maier-Leibnitz Zentrum in Garching (Germany) [177]. It is optimised for layer thicknesses between 3 - 300 Å and lateral structure dimensions from the nm to the µm range. A complete set of five different contrasts and corresponding references was measured. Measurements on MARIA were performed using two different wavelengths: 12 Å for the low-q region and 6 Å for the higher-q region up to 0.1 $Å^{-1}$, with a wavelength spread $\Delta\lambda/\lambda = 0.1$. The slit settings were chosen so that the sample surface was not over-illuminated at each incidence angle. Shorter measurement times resulting from higher neutron flux proved to be advantageous. Data and modelling are shown in SECTION 6.5.

D17

A vertical reflectometer at the Institute Laue-Langevin in Grenoble (France) [178]. It is suitable for the study of surface structures in solids and solid/liquid interfaces and membranes. It can operate in time-of-flight and monochromatic mode. A sample chamber equipped with a lensless holographic inline microscope was tested successfully. In SECTION 6.7, this sample chamber will be presented in more detail.

6.3 SAMPLE CHAMBER AND MEASUREMENT PROCEDURE

6.3.1 *Concept of sample chamber for controlled cell environment*

Experiments with living cells require careful handling and a very specific sample environment. In particular eukaryotic cells demand controlled environment concerning sterility, temperature, and nutrition. As the experimental halls in a reactor usually do not provide a cell culture laboratory, the sample chamber has to meet a number of requirements to enable the performance of reliable scattering experiments. Most of the neutron experiments within the scope of this thesis were performed at the Forschungs-Neutronenquelle Heinz Maier-Leibnitz (FRM II) in Garching. The proximity of the FRM II - it is in half hour distance by underground or car from the chair of soft matter physics at the LMU - made it possible to prepare the sample chamber at our cell culture laboratory. In this thesis, a suited approach has been developed and successfully been tested during several beam times at different neutron reflectometers. The concept is presented in the following. When working with living cells, two aspects have to be taken into special consideration:

1. The **temperature** needs to be kept at a constant level at all times, i.e. from seeding to final reflectometry experiments. For eukaryotic cells it should be kept at body temperature (37 °C).

2. **Sterility** has to be ensured all the time to avoid contamination of the cells. Contamination will lead to cell death or alteration.

In a cell culture laboratory, correct and constant temperature, as well as sterility, is a standard condition unlike during transport to the reactor guide hall and the measurement itself. Our experience shows that if possible the seeding, growing, and feeding of the cells should be done in the same laboratory to ensure a smooth workflow. FIGURE 6.1 sketches the sample chamber that was used for the experiments on REFSANS and on MARIA. To ensure constant temperature when mounted on the instrument, we used a heated water bath connected to the sample chamber. During the transport from the cell culture laboratory to the instrument, the sample chamber was placed in an isolating box and kept warm with heating elements. To guarantee sterility, it is proposed to seed the cells and to perform all the medium exchanges necessary prior to the measurement in the cell culture laboratory under sterile conditions (refer to APPENDIX C.1 for the protocols). This ensures highest possible sterility and minimizes the risk of contamination. To reduce the risk of contamination while exchanging liquid during an experiment in the reactor hall, it is necessary to work with sterile packed tubing, connectors, and syringes. The syringes were pre-filled with cell medium under sterile conditions and glued to the connectors. Note that as the sample chamber is a closed, CO_2 free system the cell medium has to be chosen accordingly. With the sample chambers used for the experiments on REFSANS and MARIA, around 4 cm · 8 cm of the Si interface were accessible for the cells to adhere.

6.3.2 *Measurement procedure*

Minimizing the time span between the cell culture laboratory and the installation on the instrument was identified to be a highly critical point when measuring living cells. As the installation and alignment of the sample chamber can be time-consuming, first a sample chamber identical in construction but filled with cell medium only was installed on the instrument. This chamber was used for preparing the heating system and pre-alignment of the instrument. Especially in the case when the sample chamber is filled with cell medium dissolved in 100 % H_2O, i.e. where no critical edge can be observed, the alignment can be challenging. Since sample chambers identical in construction were used, pre-aligning the instrument reduced the alignment time

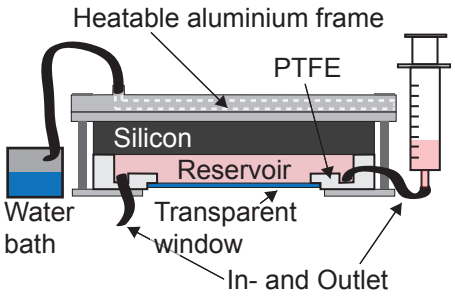

FIGURE 6.1: SAMPLE CHAMBER FOR NEUTRON REFLECTOMETRY MEASUREMENTS ON LIVING CELLS.
Sketch of the sample chamber that was used for the experiments on REFSANS and on MARIA. The PTFE piece and the silicon wafer are clamped together by an aluminium frame. One of the frame sides has a channel that allows cycling of heated water from a water bath. An O-ring inserted in the PTFE ensures watertightness. In- and outlets allow for exchanging the cell medium in the reservoir. Optical access is granted by a transparent window that is glued to the PTFE.

after changing the sample chamber drastically. The heating system was installed, and the temperature of the Si measured. The temperature of the water bath was set so that the Si block has a temperature of 37 °C. This temperature was monitored during all measurements. After successful installation and alignment of the sample chamber, a measurement was started. The measurement of the medium only was used as a reference. After starting the measurement, the sample chamber containing living cells was transported from the cell culture laboratory to the instrument. The reference measurement was stopped, and the sample chamber containing the living cells immediately was installed on the instrument after arrival. The part of the aluminium frame that is connected to the water bath is demountable, so the sample chamber can immediately be connected to the pre-heated system. Several samples were prepared according to the protocol shown in APPENDIX C.1, as the risk of contamination cannot be excluded completely and the sample has to be ready when the beam time starts. As the behaviour and growth of living cells cannot be predicted completely, it is advantageous to have several samples to choose from.The sample chamber is designed in a way that fluid exchange is possible without taking the chamber off the instrument, so exchanging the cell medium is possible without the need of realigning afterwards.

6.4 EPITHELIAL CELLS

6.4.1 *Overview*

Epithelial cells form sheets, the so-called called epithelia. They cover the inner and outer surface of the body and control fluid and molecular flow throughout tissues [33]. The epithelium as a whole is a

selective permeability barrier. The epithelial permeability barrier results not only from the properties of the epithelial cells but also from the formation of intercellular junctions. Epithelial cells adhere to the basal lamina, a thin, planar layer composed of extracellular matrix proteins. Epithelial integrity and adhesion to the basal lamina are linked to diseases such as sepsis, acute respiratory distress syndrome, atherosclerosis, and tumor progression [4].

6.4.2 *Cell line*

MDCK cells (Madin Darby Canine Kidney; ECACC 84121903) were chosen for the presented NR experiments. They have the advantage of rapid cell growth and are well suited to use in advanced (e.g. confocal) microscopic techniques. The MDCK cell lines are widely used as epithelial models as they form well defined tight junctions. Once they have reached confluence it will be very difficult to detach them. If allowed to reach confluence on conventional tissue culture plastics MDCK monolayers exhibit "doming"; where the cells become polarised and actively transport solutes through the epithelial monolayer to the plastic below. Their ability for strong adhesion allowed for transporting the attached cells to the reactor guide hall without detaching. A cell layer that does not change its structure significantly over time when reaching confluence, which is a requirement for recording NR data as cell viability naturally will continue in the sample chamber. MDCK cells continue cell division once they have reached confluence, only a reduction of cell size can be observed. Mitotic arrest is achieved once the cell area reaches a certain threshold [179]. Measurements were performed on a confluent cell layer as the intensity of the reflected signal is lower for lower cell surface densities [180]. An optical micrograph of a cell layer growing to full confluence in a sample chamber used for REFSANS and MARIA experiments is shown in FIGURE 6.2.

6.5 NEUTRON REFLECTOMETRY EXPERIMENTS FOR THE STUDY OF CELLULAR ADHESION

6.5.1 *Neutron reflectometry and contrast variation*

Neutrons are ideal to probe buried interfaces. As they only interact weakly with matter, they have the ability to penetrate deeply into many materials, such as silicon. In particular in neutron reflectivity experiments where the neutron beam penetrates through a solid support and then encounters a solid/liquid interface, structural studies of various types of interfacial layers have been performed, see CHAPTER 3 for a more detailed introduction. The coherence length of the neutrons is around 0.5 µm–1 µm, roughly one order of magnitude

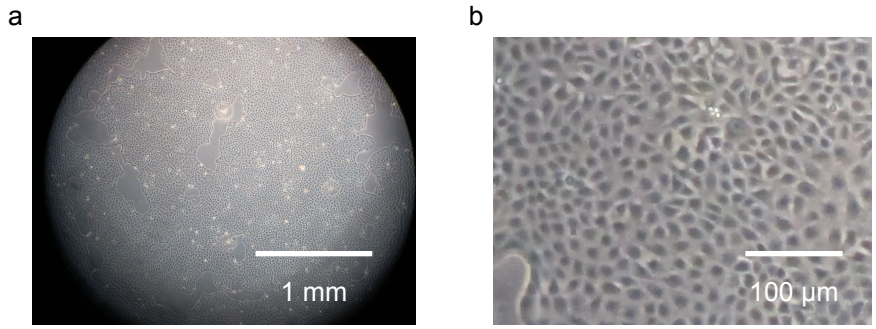

FIGURE 6.2: PICTURE OF A CELL LAYER IN THE SAMPLE CHAMBER.
Image of a layer of MDCK cells growing to confluence in the sample chamber used for experiments on REFSANS and MARIA.

shorter than a cell length.

The variation of reflectivity as a function of momentum transfer $R(q)$ is related to the square modulus of the one-dimensional Fourier transform of the SLD profile $\rho(z)$ through the relation $R(q) = (16\pi^2/q^2)$ $|\rho(z)|^2$. Recovery of the SLD profile from $R(q)$ is performed by model fitting using layer models. Variation of the scattering contrast, e.g., hydrogen-deuterium substitution in the solvent heavily reduces the ambiguity from the loss of phase information (that is characteristic of all scattering experiments) of the final obtained modelling system parameters.

In the following two sections, experiments in six different cell medium contrasts are presented. These are:

- 90 % D_2O and 10 % H_2O (CM90) on REFSANS
- 75 % D_2O and 25 % H_2O (CM75) on REFSANS and MARIA
- 50 % D_2O and 50 % H_2O (CM50) on REFSANS and MARIA
- 30 % D_2O and 70 % H_2O (CM30) on MARIA
- 15 % D_2O and 85 % H_2O (CM15) on MARIA
- 0 % D_2O and 100 % H_2O (CM0) on REFSANS and MARIA

Reference measurements on cell medium only were recorded for CM75 on both instruments. On MARIA, reference measurements for CM50, CM30, CM15 and CM0 were recorded.

6.5.2 *Neutron reflectometry data*

The specular reflectivity of the cell layer in all five contrasts recorded on MARIA is shown in FIGURE 6.3 A. The fits for the modeled reflectivities are also shown. The data recorded on REFSANS is shown in FIGURE 6.3 B. Again, the fits of the modeled reflectivities are displayed. The intensities are shifted vertically for clarity. Modelling will be described in detail in the following. As explained in more detail in CHAPTER 3, the critical angle of total reflection can be observed for CM_{90}, CM_{75} and CM_{50} and disappears, as expected, starting from CM_{30}, since $SLD_{CM_{30}} < SLD_{Si}$. The shifting of the angle of total reflection shows that the medium exchange was successful in the sense that it affects the cell-substrate interface in the expected way.

FIGURE 6.4 A-F shows the reflected intensities of the cell layer of the experiments on MARIA compared to the reference measurement for each measured contrast. For CM_{75} only small differences can be observed, even when displayed in more detail as in FIGURE 6.4 B. The same was observed for measurements in CM_{75} on REFSANS, as can be seen in FIGURE 6.4 G and H. For all other contrasts a distinct difference between the reference and the cell data can be observed. This shows that the changes on the solid/liquid interface by adhering cells do not originate from incubating cell medium only, indicating the sensitivity of the instrument towards cell adhesion.

6.5.3 *Modelling*

The data recorded on MARIA were chosen first for developing the layer model since the signal to noise ratio is better than for the data recorded on REFSANS, especially at low q values. The shorter measurement times, still with sufficiently high angular resolution, allowed for measuring in five contrasts, reference measurements were recorded for all contrasts.

Reflectivity curves cannot be directly converted into real space SLD profiles. In most cases, it is even possible to build a group of profiles which give the same reflectivity. The reason for this uncertainty is the lack of intensity at high q-values and that only the intensity and not the phase information of the specular reflectivity is measured [181]. For a highly inhomogeneous sample like a cell layer, intensity can only be recorded in a very limited q region. The analysis of the recorded data is done by adjusting all different parameters involved in the problem until a modeled reflectivity is obtained that fits to the measured reflectivity. In the case of such an inhomogeneous system like a large number of living, adhering cells on SiO_2 it is, therefore, essential to use a well-thought-out model as the base for the data

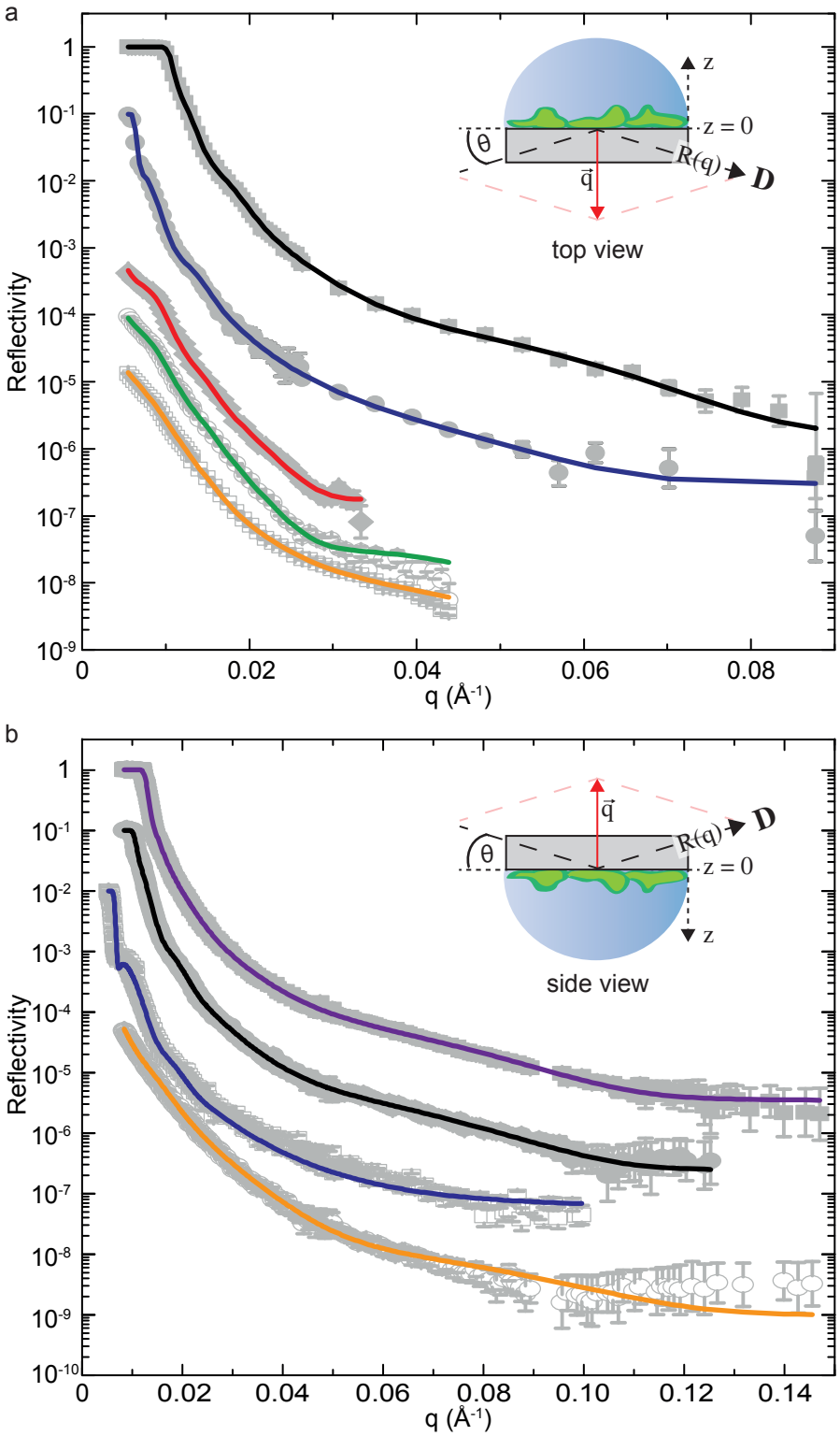

FIGURE 6.3: DATA AND FITS OF NR MEASUREMENTS ON CELL LAYER.
Neutron reflectometry data presented as normalized reflected intensities vs. momentum transfer q (grey symbols). Modeled reflectivity curves are shown as solid lines. The curves are shifted vertically for clarity. The insets shows the respective scattering geometry. **a** Reflectometry data of one cell layer recorded on MARIA in CM_{75} (squares, black), CM_{50} (circles, blue), CM_{30} (diamonds, red), CM_{15} (empty circles, green) and CM_0 (empty squares, orange). **b** Reflectometry data of the same cell layer recorded on REFSANS in CM_{90} (squares, purple), CM_{75} (circles, black), CM_{50} (empty squares, blue) and CM_0 (empty circles, orange).

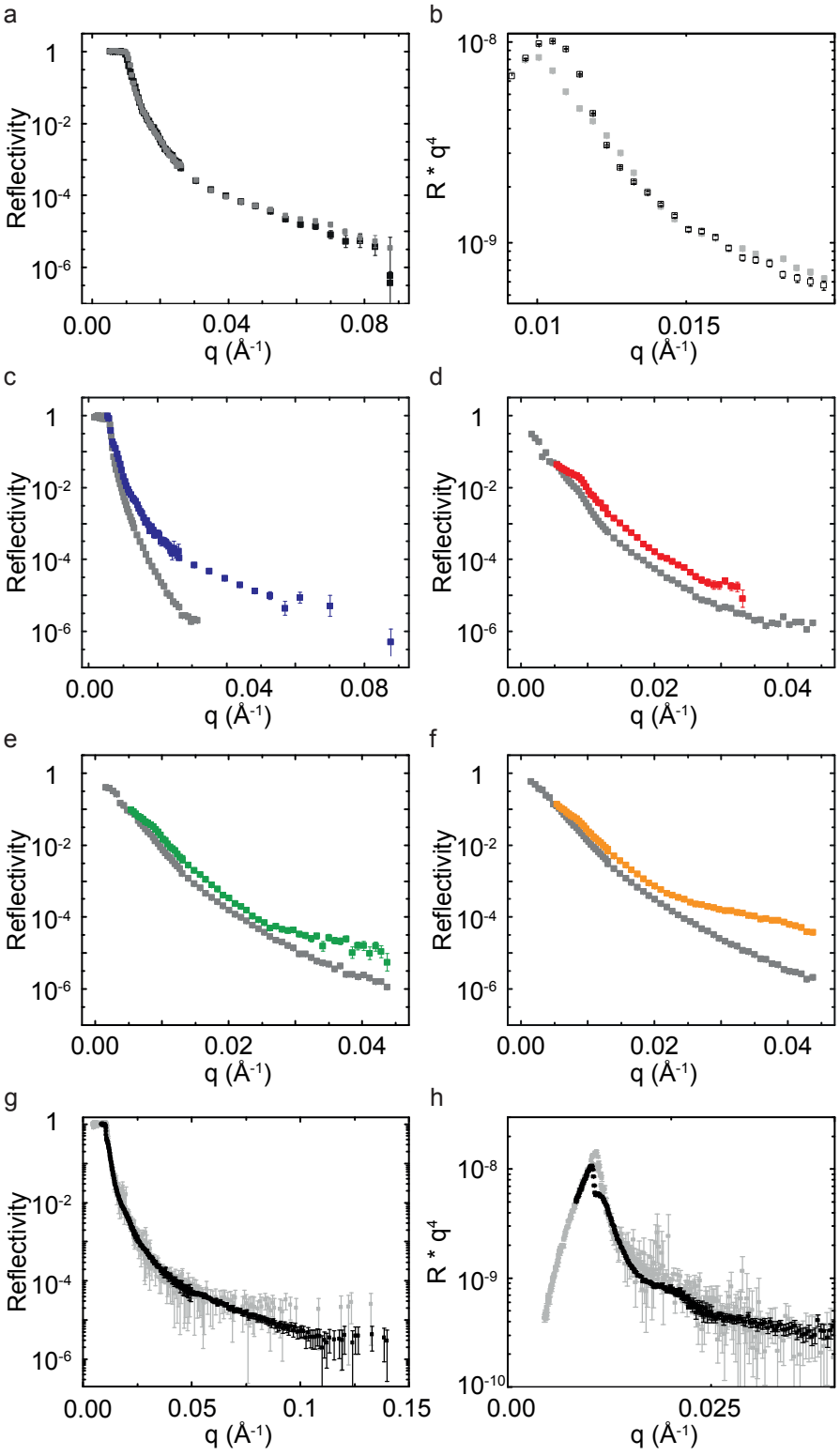

FIGURE 6.4: CELL DATA VS. REFERENCE DATA.
Neutron reflectometry data of the cell layer (shown in color) vs. reference measurements of only cell medium (grey symbols) recorded on MARIA in **a** CM_{75}, **b** shows a detailed view (the reflected intensity is divided by the Fresnel reflectivity q^{-4}), in **c** CM_{50}, **d** CM_{30}, **e** CM_{15} and **f** CM_0 and on REFSANS in **g** CM_{75}, **h** shows a detailed view (the reflected intensity is divided by the Fresnel reflectivity q^{-4}).

analysis. To avoid overparametrisation, a simple model with a low number of layers, i.e. parameters, is preferred.

The data were analyzed using MOTOFIT [111]. The program uses n numbers of discrete layers with constant SLD and thickness to describe the sample. At the interface of two adjacent layers, an error function takes the interfacial roughness into account. The program uses the modeled SLD profile to compute a reflectivity curve using the Abeles formalism [113], see CHAPTER 3 for more details. This reflectivity curve is then fitted to the data by variation of selected parameters. The modelling yields the values of the thickness, roughness and SLD value of each layer. First, the reflectivity curves of the cells in CM75 and CM50 recorded on MARIA were modeled. The minimal model that allowed reproducing the reflectivity of all data sets consists of three layers additional to the obligatory layers for fronting (substrate) and backing (bulk medium). It was iteratively applied to all reflectivity curves to identify a consistent structure model in accordance with the data. Subsequently, the three-layer model also was applied to the data recorded on REFSANS. The fits, shown in FIGURE 6.3 are all in good agreement with the experimental data. When the specular reflectivity is divided by the Fresnel reflectivity q^{-4}, the features of the specular reflectivity become much more distinct. The plots in FIGURE 6.5 A-E show the data recorded on MARIA and the fits in more detail, i.e. the reflected intensities are divided by the Fresnel reflectivity q^{-4}. All modelling parameters can be found in SECTION 6.5.4. FIGURE 6.6 A-D shows the data recorded on REFSANS and the fits in more detail, revealing that the model is also valid for larger q values.

The SLD profiles corresponding to the modelled reflectivity curves for the data obtained on MARIA and REFSANS are shown in FIGURE 6.5 F and FIGURE 6.6 E, respectively. The obtained SLD profiles all show similar characteristics. The native SiO_2 layer on the Si cannot be resolved. The SLDs of the four measurements differ only slightly in the first layer (Layer I) on the substrate , i.e. starting at 0 Å suggests that the layer is very little hydrated. The next layer (Layer II) is very hydrated, followed by a less hydrated layer (Layer III), following the same argumentation as before. The SLD values at high distances represent the SLD of the bulk. The average layer thickness and roughness of each layer, resulting from the presented SLD profiles, are presented in TABULAR 6.1. Note that for the CM50 REFSANS data the layer next to the substrate has the same SLD as the substrate itself and the modeling, therefore, is not sensitive to its thickness. The thickness of the first layer of the CM50 measurement, as depicted in the SLD profile, was set to the average thickness of the first layer of the other contrasts.

To further interpret the resulting SLD profiles, we assume the fol-

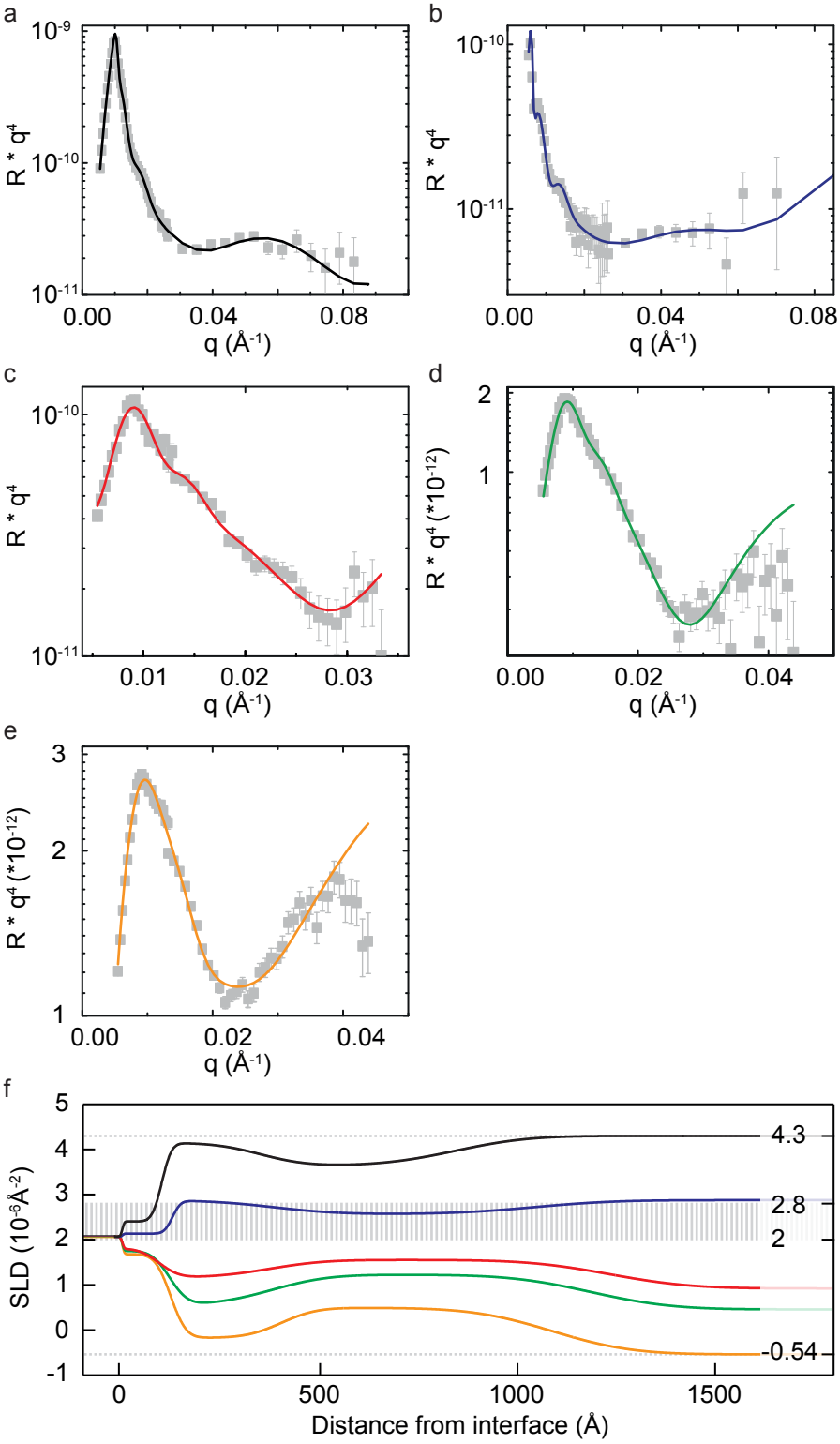

FIGURE 6.5: MARIA: DATA, FITS AND SLD PROFILES.
Reflectometry data (grey symbols) and modelled reflectivity curves (solid lines) for **a** CM_{75} (black), **b** CM_{50} (blue), **c** CM_{30} (red), **d** CM_{15} (green) and **e** CM_0 (orange). The reflectivity is divided by the Fresnel reflectivity (q^{-4}) for clarity. **f** Scattering length density profiles used to calculate the simulated intensities. Color code as in a - e. Dotted grey lines represent lower and upper values of the variation of the SLD introduced by exchanging the contrast. The range of $SLD_{Protein}(CM)$ is indicated by the striped grey area.

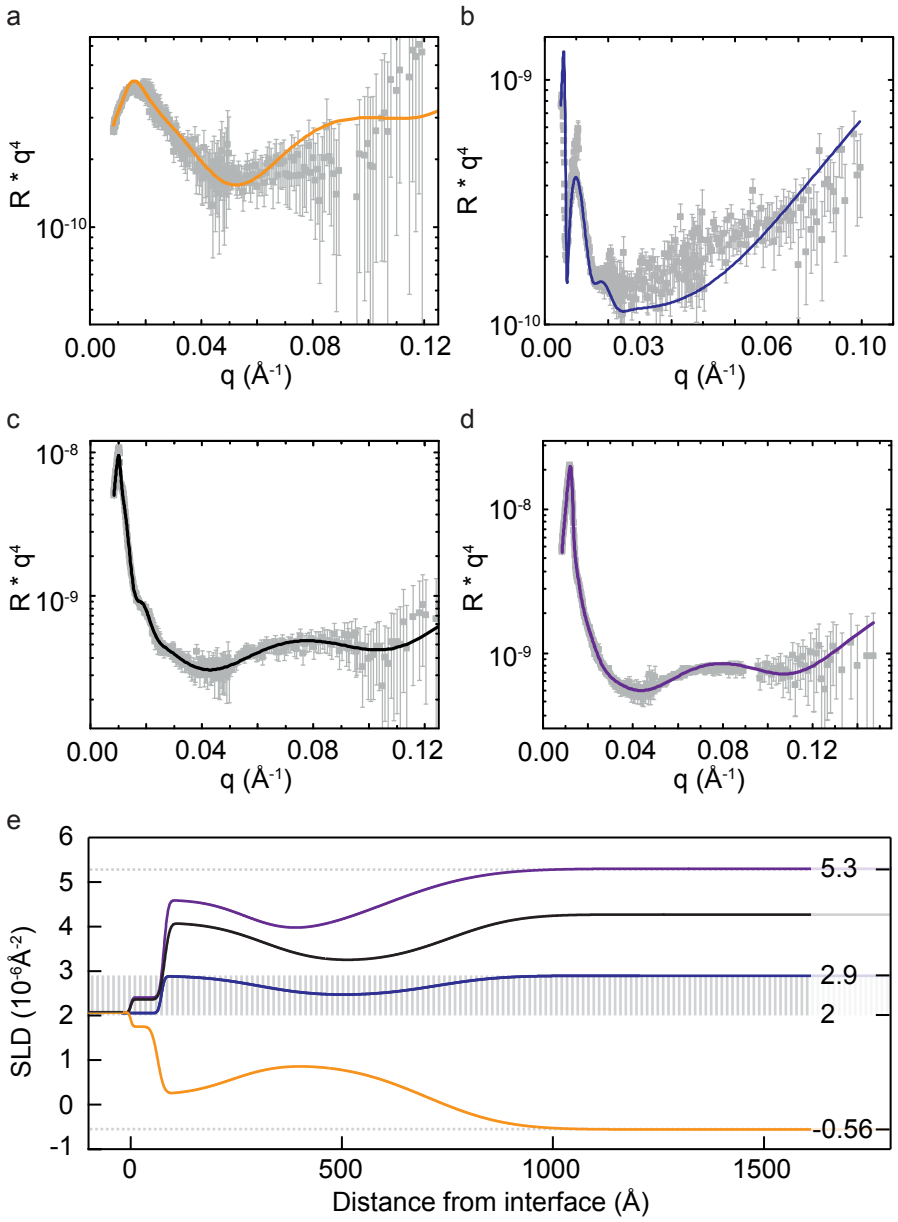

FIGURE 6.6: REFSANS: DATA, FITS AND SLD PROFILES.
Reflectometry data (grey symbols) and modelled reflectivity curves (solid lines) for **a** CM_0 (orange), **b** CM_{50} (blue), **c** CM_{75} (black) and **d** CM_{90} (purple). The reflectivity is divided by the Fresnel reflectivity (q^{-4}) for clarity. **e** Scattering length density profiles used to calculate the simulated intensities. Color code as in a - d. Dotted grey lines represent lower and upper values of the variation of the SLD introduced by exchanging the contrast. The range of $SLD_{Protein}$(CM) is indicated by the striped grey area.

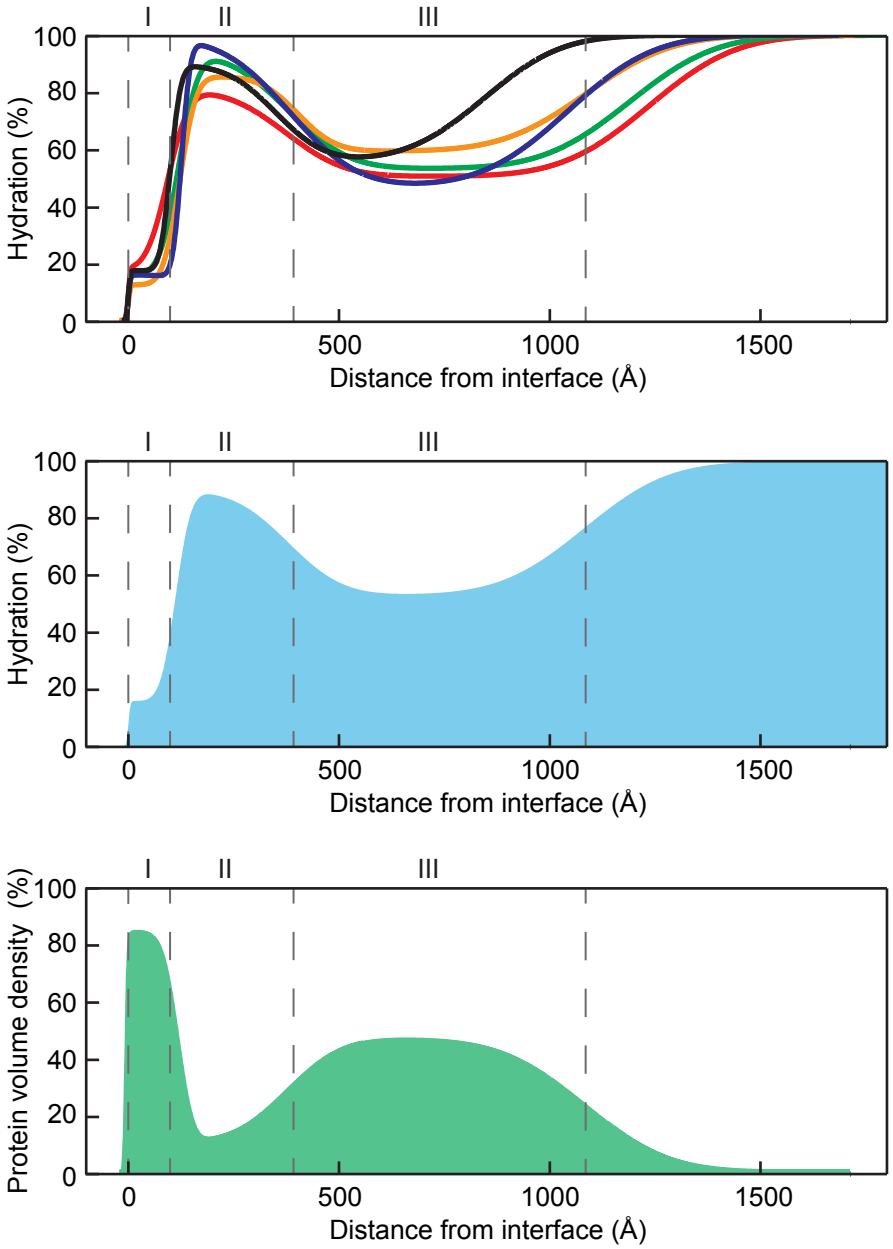

FIGURE 6.7: MARIA: HYDRATION AND PROTEIN VOLUME DENSITY VOLUME PROFILES. Hydration and protein volume density volume profiles calculated from the SLD profiles from the data recorded on MARIA. The overall hydration and protein volume density curves shown in light blue and green respectively are the average of the profiles calculated for each contrast and depicted in color.

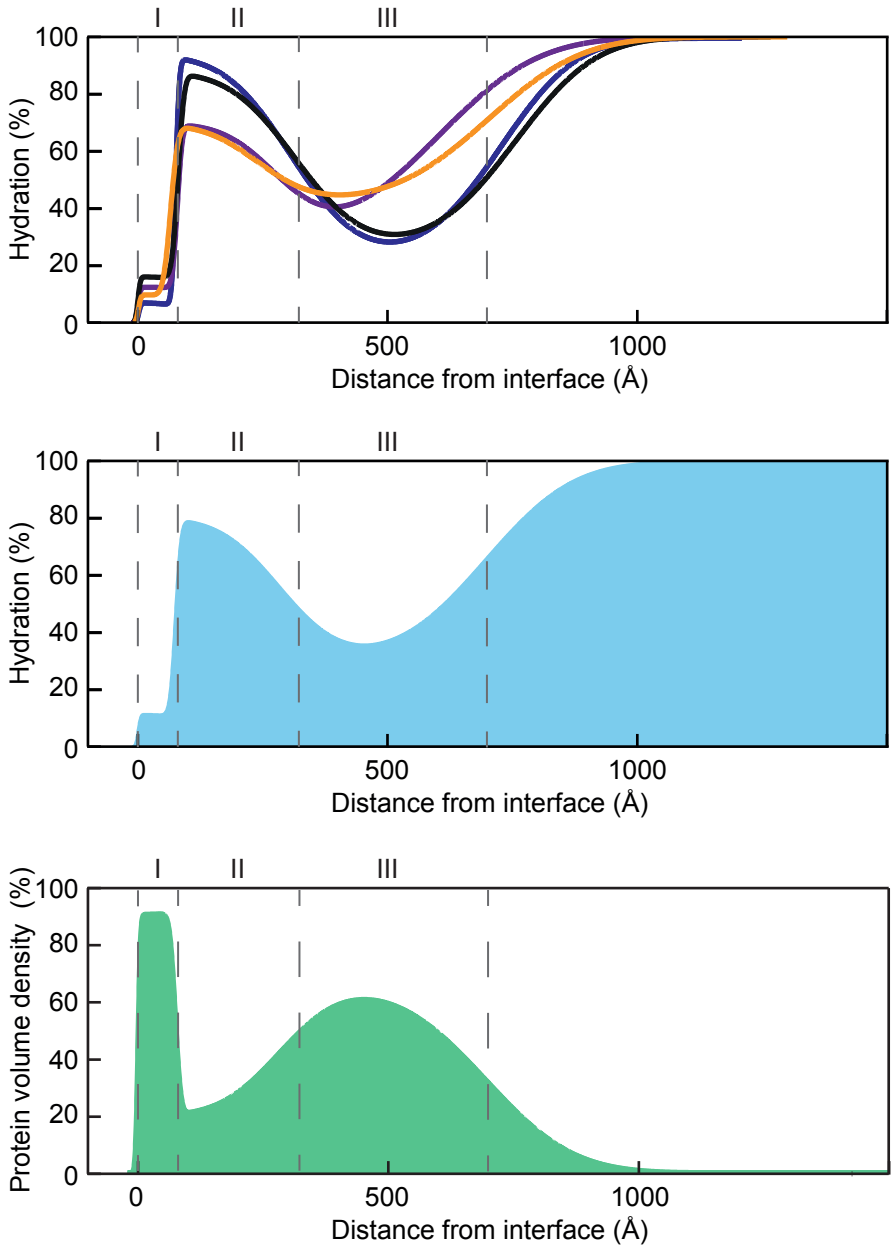

FIGURE 6.8: REFSANS: HYDRATION AND PROTEIN VOLUME DENSITY VOLUME PROFILES. Hydration and protein volume density volume profiles calculated from the SLD profiles from the data recorded on REFSANS. The overall hydration and protein volume density curves shown in light blue and green respectively are the average of the profiles calculated for each contrast and depicted in color.

lowing:

- Immediate medium exchange in highly hydrated layers.
- Proteins have a scattering length density that lies between those of H_2O and D_2O and the precise value depends on the extent of exchange of H and D between the biomolecule and the solvent [3, 5]. Consequently we assume a $SLD_{Protein}(CM)$ as a function of SLD_{Medium}, as also proposed by Efimova at al. [182].

It should be noted, that given the high number of different proteins involved in life, the assumed SLDs for the proteins are only rough approximations. The reliability of this approximation directly affects the hydration and protein volume density profiles. The range of SLD variation introduced to the system by exchanging the contrast and the range of $SLD_{Protein}$ are indicated in the SLD profiles in FIGURE 6.5 F and FIGURE 6.6 E. Hydration and protein volume density volumes can be calculated from the SLD profile to further investigate possible layer structures by [62]:

$$\text{Hydration} = (SLD_{fit} - SLD_{Protein}) \,/(SLD_{Cell\ medium} - SLD_{Protein}).$$

The average thickness, roughness, and hydration or protein volume density, calculated from the measurements of the different data sets recorded on MARIA and REFSANS are shown in FIGURE 6.7 and FIGURE 6.8, respectively. For the calculation of the hydration and protein volume density volumes shown in FIGURE 6.7 and FIGURE 6.8 the following values for $SLD_{Protein}(CM)$ were assumed for layer II and layer III:

$$\begin{aligned}
SLD_{Protein}(CM90) &= 2.9\,\text{Å}^{-1},\\
SLD_{Protein}(CM75) &= 2.8\,\text{Å}^{-1},\\
SLD_{Protein}(CM50) &= 2.3\,\text{Å}^{-1},\\
SLD_{Protein}(CM30) &= 2.2\,\text{Å}^{-1},\\
SLD_{Protein}(CM15) &= 2.1\,\text{Å}^{-1},\\
SLD_{Protein}(CM0) &= 2.0\,\text{Å}^{-1}.
\end{aligned}$$

Since layer I is little hydrated, it is not assumed that the labile hydrogens of the proteins exchange with higher D_2O concentration. As the cells were grown in H_2O, the $SLD_{Protein}$ was assumed to be $2.0\,\text{Å}^{-1}$ in layer I for all contrasts. The average values for the hydration of the three layers of both data sets are shown in TABULAR 6.1.

Considering that the presented work was performed with living cells and many factors influence their growing behaviour, the results of

MARIA	Thickness (Å)	Roughness (Å)	Hydration (%)
Layer I	112.3	28.6	16.1
Layer II	267.3	101.4	89.8
Layer III	702.4	156.7	53.3

REFSANS	Thickness (Å)	Roughness (Å)	Hydration (%)
Layer I	74.2	8.8	11.5
Layer II	210.1	94.5	80.2
Layer III	410.3	138	31.1

Table 6.1: AVERAGE LAYER THICKNESS, ROUGHNESS AND HYDRATION.

the analysis of the different data sets are very consistent. The effect of the longer measurement times on REFSANS and the thereby possibly caused alteration due to exposure to D_2O are likely to have had an impact on cell growth and adhesion.

So far, only one study on epithelial cells probed with NR was presented [4]. There, endothelial monolayers were studied under dynamic flow conditions. The data is modeled with a three-layer model, namely a layer of CAMs on the substrate, followed by a layer representing the plasma membrane; the last layer represents the inside of the cell. This is in contradiction to our interpretation. The structure of supported lipid bilayers on planar surfaces can be resolved by NR, as shown in numerous examples [58, 60, 183–185]. In particular the hydrophobic region of the lipid tails is a significant feature in the SLD profile of a bilayer, which is measurable due to the difference of its SLD to the SLD of the lipid heads or water. Resolving a lipid bilayer on rough or uneven surfaces is more challenging, as the SLD profile smears out and the differences in SLD become less prominent [186]. When the deformation of the bilayer is in the order of the thickness of the bilayer itself, resolving its structure with a layer model is questionable. It was shown that the cell membrane flickers due to thermal excitation. Bruinsma et al. showed in a study with biomimetic cell models that weakly adhering regions of the membrane have a fluctuation amplitude of about 20 nm [77]. For cells, it was assumed that, due to the strong coupling of the plasma membrane to the actin cortex, thermally induced undulation forces do not play a role. Zidovska et al. proved the contrary; they showed in studies with macrophages, that nucleated cell envelopes exhibit pronounced bending excitations

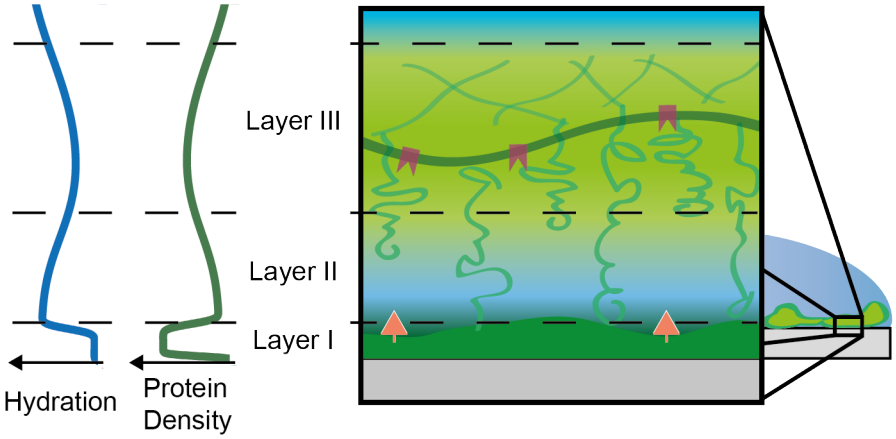

FIGURE 6.9: ILLUSTRATION OF THE INTERPRETATION OF THE RESULTS OF THE NR EXPERIMENTS WITH CELLS.
The substrate is coated with a dense protein layer (layer I), followed by a highly hydrated layer II. Layer III represents the composite membrane. At large distance from the substrate, the hydration transitions to 100 %. Average values for layer thickness and hydration resulting from the analysis of the data recorded on MARIA and REFSANS are shown in TABULAR 6.1.

of around 10 nm root mean square amplitude. Furthermore, in a living cell, approximately 50 % of the plasma membrane mass is protein [33]. This leads us to the assumption, that the lipid bilayer, i.e. the hydrophobic tail region, cannot be resolved in the presented experiments.

FIGURE 6.9 shows our interpretation of the resulting layer structure. A little hydrated, dense protein layer is located directly on the substrate (layer I). It has a thickness of around 112 Å for the cell layer measured on MARIA and around 74 Å for the cell layer measured on REFSANS. Comparing the data of the cell layer to the data of the reference measurements suggests that the cells form this layer to generate a bioanalogue tissue film. Since this bioanalogue film is supported by SiO_2, the receptor mobility is inhibited. The second layer is a highly hydrated 270 and 210 Å thick layer, respectively. Contrast variation reveals an effective water exchange in this layer. The less hydrated composite membrane is represented in layer III, where the protein density rises. The high hydration of layer II suggests that very few domains of close adhesion are formed. As discussed earlier, this is in agreement with results from studies with model systems and immobile receptors [171]. The modelled SLD values for the cell medium, i.e. the backing, are in accordance with the expected SLD values for the H_2O / D_2O mixture of the respective cell medium.

6.5.4 *Parameters for fitting*

Layer description	**Thickness** (Å)	**Roughness** (Å)	**SLD** (10^{-6} Å^{-2})
Measurement 1: 0 % D_2O and 100 % H_2O			
Si	-	4	2.07
Layer I	64.097	11.636	1.75
Layer II	175.55	84.992	0.226
Layer III	460.29	147.94	0.909
Backing	-	-	-0.557
Measurement 2: 50 % D_2O and 50 % H_2O			
Si	-	4	2.07
Layer I	74.233	6.0	2.07
Layer II	230.01	104.64	2.9
Layer III	420.64	118.94	2.455
Backing	-	-	2.904
Measurement 3: 75 % D_2O and 25 % H_2O			
Si	-	4	2.07
Layer I	80.069	9.689	2.366
Layer II	234.02	103.52	4.09
Layer III	440.8	126.1	3.2
Backing	-	-	4.270
Measurement 4: 90 % D_2O and 10 % H_2O			
Si	-	4	2.07
Layer I	78.533	7.941	2.408
Layer II	200.9	84.937	4.6
Layer III	319.44	158.94	3.692
Backing	-	-	5.3

Table 6.2: PARAMETERS FOR MODELLING NEUTRON REFLECTIVITY DATA MEASURED ON REFSANS.
Shown in chronological order.

Layer description	**Thickness** (Å)	**Roughness** (Å)	**SLD** (10^{-6} Å^{-2})
Measurement 1: 75 % D_2O and 25 % H_2O			
Si	-	4	2.07
Layer I	100.06	19.512	2.405
Layer II	249.99	90.817	4.145
Layer III	495	143.69	3.642
Backing	-	-	4.3
Measurement 2: 50 % D_2O and 50 % H_2O			
Si	-	4	2.07
Layer I	126.19	16.566	2.142
Layer II	256.66	124.99	2.874
Layer III	660.95	159.28	2.574
Backing	-	-	2.88
Measurement 3: 30 % D_2O and 70 % H_2O			
Si	-	4	2.07
Layer I	93.27	39.89	1.81
Layer II	280.87	109.71	1.164
Layer III	861.63	161.87	1.552
Backing	-	-	0.92
Measurement 4: 15 % D_2O and 85 % H_2O			
Si	-	4	2.07
Layer I	119.94	35.919	1.752
Layer II	259.93	111.94	0.557
Layer III	809.07	160.61	1.224
Backing	-	-	0.458
Measurement 5: 0 % D_2O and 100 % H_2O			
Si	-	4	2.07
Layer I	121.83	30.858	1.68
Layer II	280.55	69.775	-0.172
Layer III	685.31	157.82	0.491
Backing	-	-	-0.539

Table 6.3: Parameters for modelling neutron reflectivity data measured on MARIA.
Shown in chronological order.

6.5.5 *Discussion*

Performing neutron scattering experiments with living cells is very challenging. The sample environment has to be highly sophisticated and there is a general lack of infrastructure for working with cells in a neutron guide hall. The timing of the sample being ready and the start of the beam time creates problems. In addition, several sample chambers have to be prepared to ensure that a sample chamber containing a confluent layer of healthy cells is available at the beginning of each beam time. Events like an unexpected reactor shut-down or problems with the instrument often result in the end of the experiment. Even though the problem might be solved after a short time, the time frame where the sample can be measured in the desired state is not sufficiently long. The pioneering character of the measurements with living cells presented in this thesis was confirmed by the concerned questions about the samples from the radiation protection office at the FRM II, which seemingly had little experience with living sample experiments. Working alone on such a project, time and logistics were difficult to handle – several hundred kilometers travelled back and forth between laboratory and neutron instrument in one beam time, located 17 kilometers apart, tells its own tale. Furthermore, a polished silicon surface with very low roughness is a requirement for performing neutron reflectometry but a rather unusual interface for growing cells. When flushing the sample chamber without sufficient care, sometimes the whole confluent cell layer would detach like a skin from the surface, destroying the sample in the last preparation step before the experiment.

Nevertheless, successful experiments were performed as presented in this chapter. The findings contribute to the question of how cells adhere to a substrate. But already the differences in the resulting average layer thicknesses and hydration between the data recorded on MARIA and REFSANS indicate the complexity of the measured system. Many factors can influence the behaviour of the cells – e.g., their transport to the instrument, the time that they spend in the sample chamber, and temperature. During a beam time on D17 in the month of July, the temperatures were so high that the sample chamber rather would have had to be cooled to be at 37 °C.

Installing a cell culture laboratory in striking distance to the neutron reflectometer should be a precondition for continuing this project as well as that the beam time is organized in a way that the measurement can start when the cells have grown to full confluence. This perception was shared in private communication by Ann Junghans and Luka Pocivavsek, authors of the only published paper on NR with endothelial cells. The strict radiation protection laws in Germany and

the resulting restrictions on transporting material into and out of the guide hall in also speak in favour of the installation of a cell culture laboratory in the guide hall.

6.6 X-RAY REFLECTOMETRY EXPERIMENTS FOR THE STUDY OF CELLULAR ADHESION

It is in general very useful to have complementary information from XRR to NR [181], especially because of the larger accessible q region and the thereby gained defined structural information. A more detailed comparison of XRR to NR can be found in CHAPTER 3. In this thesis, a sample chamber was constructed following the concept presented in SECTION 6.3.1 for performing X-ray reflectometry measurements on cells. The chamber additionally was equipped with an inline holographic microscope and will be presented in more detail in the next section.

The here presented experiments were performed on the Mo-anode-based in-house reflectometer (see CHAPTER 4 for detailed description) as $\theta - 2\theta$ scans of sample and detector angle, background measurements with an offset for θ of $-0.05°$ and corrected for by subtraction. As described by Salah et al. [118], the effective beam height was corrected by

$$I_{corr} = I_{exp}\theta_{so}/\theta \quad . \tag{6.1}$$

The corrections were applied below the spill-over angle

$$\theta_{so} = \arcsin(d_{en}/l) \quad , \tag{6.2}$$

i.e. the angle for which the complete sample in the scattering plane is illuminated by the full beam height. d_en is the slit opening and l the length of the sample in the scattering plane. The intensity of all measurements was normalized to 1 and converted to momentum transfer by $q = 4\pi/\lambda sin(2\theta/2)$. An introduction to the theory of reflectometry can be found in CHAPTER 3.

All preparation steps that require sterility where carried out in an in-house cell culture laboratory. FIGURE 6.10 A and B shows the recorded specular reflectivity of a confluent cell layer and after detaching the cells with trypsin as well the reflectivity of a confluent cell layer recorded in a second experiment on Si with a 200 Å thick SiO_2 layer. The inset in FIGURE 6.10 A shows the scattering geometry for the XRR measurements. Trypsin is an enzyme that is commonly used in cell culture laboratories to detach adherent cells. After detaching the cells in the first experiment, the chamber was filled with pure cell medium. No significant differences in the reflectivity was observed comparing the reflectivity curves. Note that the SiO_2 layer causes Kiessig fringes.

In FIGURE 6.10 C the data of the second experiment and the modelling is shown. With one layer representing the 200 nm thick SiO_2 layer in H_2O the curve can be modeled with high accuracy. FIGURE 6.10 D shows the specular reflectivity of a cell layer attaching to quartz before and after treatment with trypsin. Again, no significant differences in the reflectivity curves can be observed. After performing the XRR measurement, the cell layer was imaged. Compared to a confluent cell layer on quartz prior to the exposure to the X-rays, as shown in FIGURE 6.10 E, a clear difference in morphology and cell density can be observed indicating beam damage. The image recorded after the measurement is shown in FIGURE 6.10 F. Taken together, the small difference between the reflectivity curves of all four presented XRR measurements and the little difference to the modeled curve of a bare SiO_2 interface with water, provide no further insight into cell adhesion. ΔSLD might be too small between the water and the composite membrane for X-rays to significantly change the reflected signal. Additionally, beam damage and free radicals induced by the X-rays might affect cell adhesion and even lead to apoptosis.

6.7 SAMPLE CHAMBERS FOR SIMULTANEOUS CELL IMAGING AND REFLECTOMETRY

During this thesis, a custom built X-ray and a custom built neutron sample chamber was equipped with a lensless holographic inline microscope in collaboration with the group from Philipp Paulitschke (Department für Physik, LMU, München). The correlation of scattering data and simultaneously recorded optical control can be advantageous, especially when working with such a delicate sample as living cells. The sample chamber, built as a closed system that provides enough nutrition, sterility and the correct temperature, equipped with the microscope, which allows permanent optical control during growth and experiment, is a very compact, transportable, easy-to-handle system. It redundantizes a cell culture laboratory and a free-standing light microscope after seeding the cells into the chamber. Furthermore, the microscopy technique is not prone to vibration. A good overview of lensless imaging and sensing can be found in the review of Ozcan et al. [187].

The holographic microscope consists of a charge-coupled device (CCD) chip and a laser. FIGURE 6.11 shows a schematic and its functionality. The laser light is scattered by the cell layer and recorded with the CCD chip. The images are reconstructed afterwards, more details about the reconstruction are provided in the master thesis of Tobias Pärr [188]. Recording multiple pictures at different distances to the cell layer showed to be advantageous. For this purpose, the CCD chip can be mounted on a lifting stage. The compactness and the fact that

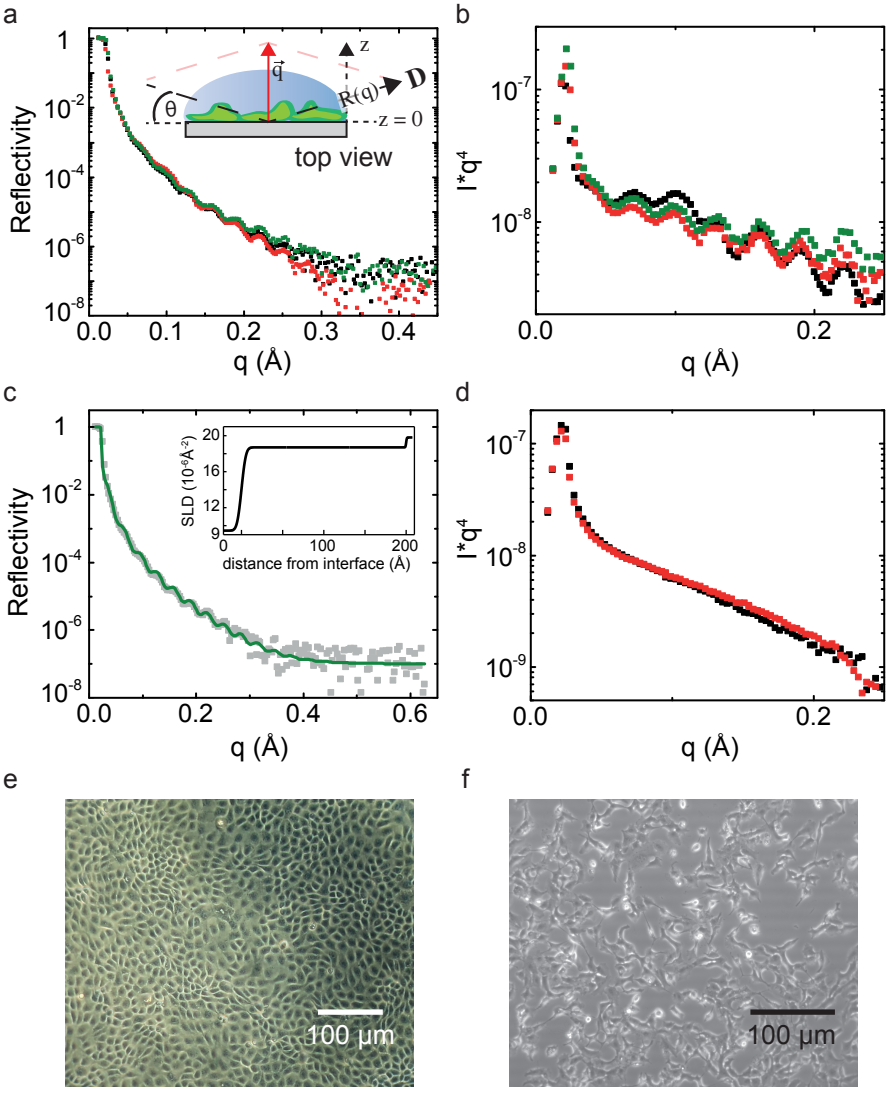

FIGURE 6.10: XRR ON A CONFLUENT LAYER OF MDCK CELLS.
a The recorded specular reflectivity of a confluent cell layer (black), after detaching the cells (red), and of a confluent cell layer recorded in a second experiment (green) on Si with a 200 Å thick SiO_2 layer. The scattering geometry is shown in the inset. **b** A more detailed view of the reflectivity shown in a, intensities are divided by the Fresnel reflectivity (q^{-4}). The fringes are caused by the SiO_2 layer. **c** The solid line shows the modelling of the data that is shown in green in a; the data now is shown in grey symbols. The inset shows the SLD profile used for calculating the reflectivity - a 200 Å thick SiO_2 layer is sufficient. **d** Specular reflectivity of a cell layer attaching to quartz (black) and after removing the cells with trypsin (red). **e** Image of a confluent cell layer on quartz in the sample chamber. **f** Image of a cell layer on quartz in the sample chamber after a XRR measurement.

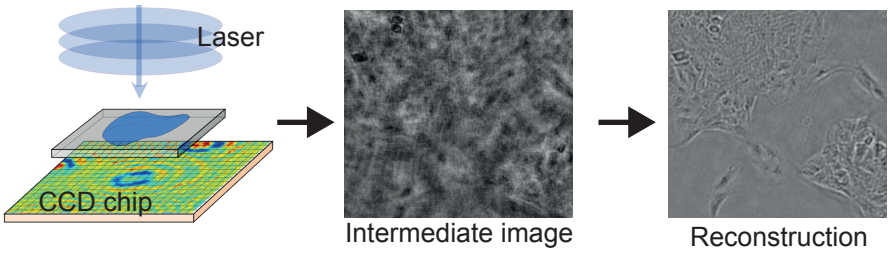

FIGURE 6.11: SCHEMATIC AND FUNCTIONALITY OF A LENSLESS HOLOGRAPHIC INLINE MICROSCOPE.
The laser light is scattered by the cell layer and recorded with the CCD chip. The final image can be reconstructed afterwards, an intermediate image and the final reconstruction is shown. The pictures were kindly provided by Tobias Pärr.

a lensless microscope requires no focusing allow the use during a reflectometry experiment, where the space on the instrument usually is limited, and the chamber is not accessible during a measurement.

As X-rays damage cells (see SECTION 6.6) monitoring the state of the cells might open the door for recording data just until the cell morphology starts to alter. FIGURE 6.12 A shows a picture and B a schematic of the chamber for experiments with adherent cell layers. It was developed in this thesis and is equipped with a holographic microscope. The temperature of the sample chamber can be kept at 37 °C with a heating resistor. The liquid reservoir is big enough to feed the cells for several days. The optics allow for monitoring the growth of the cells. As soon as the cell density is high enough, the chamber including the compact optics can easily be installed on the X-ray reflectometer. Due to the scattering geometry, a quartz die with the dimensions of 15 mm · 20 mm is used as a substrate. The thickness of the substrate of 1 mm and the resulting shorter minimal distance between CCD chip and solid/liquid interface compared to the neutron sample chamber allow for better reconstruction of the images. FIGURE 6.12 C shows the reconstructed image of a confluent layer of A549 cells.

Neutron scattering experiments can take up to days and as beam time usually is scarce, monitoring the cells during the experiment can save valuable beam time. Additionally, most neutron sample chambers are rather thick, because they are clamped together by an aluminium frame, and the substrate is usually a few centimeters thick due to reasons of scattering geometry. The resulting sample to objective distance makes it challenging to look at adherent cells even with a standard light microscope. Especially when only being a guest scientist, it can be difficult to find a microscope setup that fits the chamber and allows for detecting the cells. FIGURE 6.12 D shows the schematic of a sample chamber equipped with a lensless holographic inline mi-

croscope that was built in this thesis. In a beam time on D17 the lensless imaging system was successfully tested, and the state of the cellular layer monitored during the neutron experiment. This proves that the chamber can fulfil the task of monitoring samples during a neutron scattering experiment and the compatibility problem of sample chambers and optical microscopes. FIGURE 6.12 E shows a picture of the sample chamber while being mounted on the instrument. FIGURE 6.12 F shows the reconstructed image of a confluent cell layer in the sample chamber recorded without and with lifting stage, respectively.

6.8 CONCLUSION AND OUTLOOK

Cell adhesion is a central element in tissue mechanics, biological cell-cell signaling and cell motility. In this chapter, we present neutron reflectometry experiments which probe the adhesion of a confluent layer of epithelial cells to a solid substrate. We specifically exploit the fact that the contrast of the cell membrane and the surrounding medium can be varied by varying degree of deuteration of the buffer. This capability allows for a detailed analysis of the thickness, the density profile and in particular the hydration layer of the cleft between epithelial cell membrane and the substrate.

Since the needed infrastructure for working with cells in the neutron guide hall does not exist, we developed a cell culture sample chamber allowing to grow cells under proper cell culture conditions in order to assure valid conditions to perform neutron reflectivity measurements in-vitro. The cell chamber also enables perfusion with cell medium and hence allows for contrast variation in-situ by exchange of buffer with different H_2O-to-D_2O ratio. It includes optical control of the sample. Furthermore, the chamber was equipped with an inline holographic microscope. This sample chamber could have many applications when working with delicate samples. It is no longer a black box during a measurement and the state of the cells can be directly related to the scattering data. There is a lot of potential for correlating scattering data with the effect of drugs on cells or cell migration. The resolution limit of the inline holographic microscope might encourage other researchers in, e.g., the field of colloidal physics to use the concept to observe their samples during measurement in order to correlate the optical and the scattering signal.

The data was analyzed following the theory of cell adhesion. The contrast variation technique allowed us to reduce the ambiguity of data modelling and to determine the thickness and degree of hydration of the interface between the adherent cells and the substrate. Using the minimal model approach, we suggest a three-layer interfacial or-

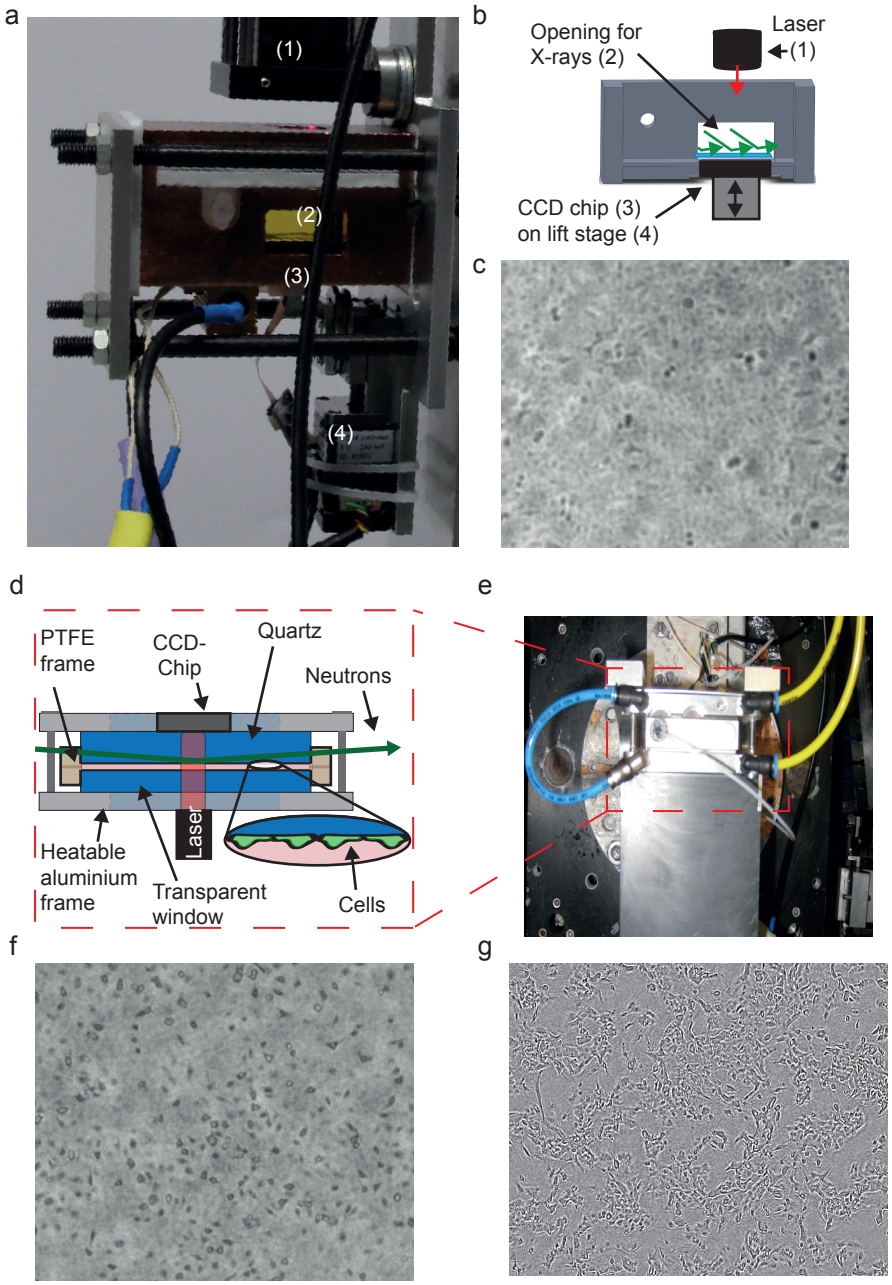

FIGURE 6.12: SAMPLE CHAMBERS WITH LENSELESS HOLOGRAPHIC INLINE MICROSCOPE AND RECONSTRUCTED IMAGES.

Sample chamber with lenseless holographic inline microscope for X-ray reflectometry measurements: **a** Picture; **b** Schematic of cross section; **c** Reconstructed image of a confluent layer of cells.

Sample chamber with lenseless holographic inline microscope for neutron reflectometry measurements: **d** Schematic; **e** Picture of the sample chamber mounted on D17; **f** Reconstructed image of the confluent layer recorded without lifting stage in the configuration shown in d and e; **g** Reconstructed images with lifting stage.

ganization consisting of a very dense, 70 - 120 Å thick, protein film bound to the silicon surface interface, followed by a highly hydrated 180 - 280 Å thick layer which is followed by a several hundred Å thick layer attributed to the less hydrated composite membrane. We further suggest that the bottom dense protein layer is formed by the cells to generate a bioanalogue tissue film. These results were achieved by exploring the unique properties of neutron scattering, which could hardly be realized with any other technique in this combination, i.e. the combination of structural analysis in the Å range and probing the hydration by contrast variation.

There still remain a lot of questions regarding cell adhesion and NR has a big potential to contribute to answering these questions. Systematically measuring the adhesion of proteins in the cell medium on the substrate could provide a full picture of the solid/liquid interface before seeding the cells. In this chapter it is shown that the probably simplest approach of exploring the sensitivity of neutrons for different isotopes, exchanging the D_2O content in the cell medium, allows for analyzing the structure and the hydration profile of the interface between the cell and the substrate. In combination with specific deuteration of molecules like hyaluronic acid or lipids involved in the process of adhesion, NR could contribute to a more detailed understanding of cell adhesion.

The low intensity of the neutrons at higher q values as well as cell alteration due to long measurement times remain unsolved issues. Using XRR might provide complementary information. Although the scattering contrast is worse, higher q ranges are accessible. XRR measurements performed on the molybdenum-anode-based in-house did not provide complementary data, this is attributed to beam damage in the sample. Reduced beam exposure times and higher photon energy, causing less photo effect, can reduce the beam damage. Therefore experiments on a synchrotron, where higher photon flux and tunable photon energy are available, might give more insight.

Part V

SUMMARY AND CONCLUSIVE REMARKS

7

SUMMARY AND CONCLUSIVE REMARKS

The experiments presented in this thesis revealed the structure of complex biological interfaces.

The lipid monolayer structure on graphene was determined using XRR. The structure function relationship was established. For the understanding of electrostatics as well as lipid kinetics, the understanding of the interface structure was decisive. The basis was laid for further complementary measurements of the structure and functionality of lipid-coated sensing devices. NR measurements could not be performed in the scope of this thesis, mainly due to size limits in the growth of the graphene patches. Nonetheless, graphene growth techniques are evolving fast and so is the production of deuterated molecules. Many phospholipids can be obtained with deuterium labeling of the tails or of specific regions in the head group [3]. The combination of NR with deuterated lipids and molecules have a high potential to lead to further insights into the surface structure of biofunctionalized graphene-based sensing devices. For instance, it is already possible to engineer systems which allow to study the insertion of molecules into membranes and to determine the structure as well as the dynamics of the interaction [5].

The unique properties of neutrons allowed to reveal a three-layered structure of the adhesion of epithelial cells on a solid interface. Sample chambers for NR as well as for XRR measurements were developed. Contrast variation measurements on different NR instruments were performed and the results correspond to the theoretical predictions. This is the foundation for more sophisticated measurements, for example using different surface passivations or surface treatments or even gene modification to tune cell adhesion. Specific deuteration has a great potential for giving a more detailed insight. Furthermore, the sample chambers were equipped with a holographic inline microscope and successfully tested. Unfortunately, XRR measurements could not provide more insight; this is attributed to the beam damage. The much shorter measurement times on synchrotrons could be the key for recording XRR data of a cell layer. One essential condition for more sophisticated reflectometry experiments would be to invest in manpower and infrastructure, such as a cell culture laboratory close to the instrument.

The two presented projects show that a prerequisite for

reliably revealing the structure of complex interfaces is to perform a set of reference measurements and actual measurements. It is therefore essential to have an easy access to the instrument. The reconstruction of the in-house reflectometer was crucial for successful data recording and analysis of the lipid structure on graphene. The proximity of the Research Neutron Source Heinz Maier-Leibnitz (FRM II) and the measurements in many different contrasts were decisive for the success of the NR measurements on cells. Both projects explored the boundaries of reflectometry, and it was shown that this technique can make a valuable contribution.

Reflectometry is evolving: Technical advances and developments of the sample environment allow for measuring increasingly complex systems with a resolution not currently achievable by other methods. New data-analysis approaches, such as rigorous and self-consistent modeling strategies and MD simulations [189] have increased the accuracy of data modeling and interpretation. Most importantly, the increased use of complementary characterization techniques has extended the variety of membrane applications which are studied and allowed the investigation of more complex systems [1]. Complementary information obtained from both, modeling and the use of other experimental techniques, maximize the information obtained from reflectometry data [3].

The interface between solids and biological membranes is a current topic, since the fluid mosaic model implied a randomness that is recognized not to be correct and therefore the need for a new membrane model has become necessary [2, 7]. The next generation of neutron scattering instruments and neutron sources will allow researchers to tackle new and old problems. Two out of four instruments for large-scale structures in construction at the European Spallation Source are reflectometers – a strong indication that reflectometry will remain highly significant for answering fundamental questions.

Part VI

APPENDIX

a

APPENDIX

A.1 LIPID PREPARATION

A.1.1 *Lipid solution preparation*

All lipids were purchased from AvantiPolar Lipids (Alabaster, Alabama, USA); Texas Red DHPE was purchased from ThermoFisher (Waltham, Massachusetts, USA). To prepare lipid vesicles, the desired amount of lipids dissolved in chloroform was put in a glass vial in desired mixture. The chloroform was then evaporated under nitrogen flow and the vial stored in vacuum overnight. The dried lipids then were suspended to 0.5 mg ml^{-1} in Dulbecco's PBS (Sigma Aldrich, Taufkirchen, Germany). Before use they were diluted with Dulbecco's PBS (1:20).

A.1.2 *Extrusion*

The suspension was passed 11 times through a polycarbonate filter with pores of a size of 100 nm, 200 nm or 1 µm (AVANTI) to produce unilamellar vesicles [190]. dynamic light scattering (DLS) measurements of extruded DOTAP vesicles can be found in **Appendix** a.1.7.

A.1.3 *Tip sonication*

The suspension was tip sonicated (Bandelin electronic Berlin, Berlin, Germany) for 10 minutes with 60 % of maximum power. Suspension was centrifuged for 3 minutes with 10 000 RCF and pipetted off afterwards to get rid of eventual metal swarf. DLS measurements of tip sonicated DOTAP vesicles can be found in **Appendix** a.1.7.

A.1.4 *Lipid deposition for X-ray reflectometry measurements*

After the measurement of the graphene layer, the vesicle solution (1 mg:20 ml) was injected into the chamber and incubated overnight, allowing the lipid vesicles to adhere to the surface. The vesicles were then ruptured by osmotic shock and afterwards flushed intensively with Dulbecco's PBS to remove lipid aggregates/eventual multilayer. To allow for self exchange of the POPG lipids into the DOTAP membrane, a POPG vesicle solution (1 mg:20 ml) was injected to the chamber where the DOTAP layer had formed and incubated overnight. The vesicles were then ruptured by osmotic shock and afterwards flushed

intensively with Dulbecco's PBS to remove lipid aggregates/eventual multilayer.

A.1.5 *Vesicle fusion*

Membrane formation was achieved by (1) immersion of the substrate in a vesicle-containing solution over night or (2) osmotic shock [191], where the lipid solution is exchanged with DI water after being exposed to the lipid solution for around one hour. After again around one hour, the sample chamber is flushed with PBS buffer to remove excess lipids. The sample shall not be exposed to air at any time, as contact with air destroys the lipid membrane. No difference in the quality of the lipid layer between the two techniques protocols was identified.

A.1.6 *Lipid spreading*

To prepare a stamp, the dried lipids were dissolved in isopropyl alcohol. A PDMS[1] stamp was prepared and a few µl of the lipid solution applied. The stamp dried overnight to evaporate the alcohol.

A.1.7 *DLS measurements of lipid vesicles*

DLS measurements (DTS 1070 cuvettes, Zeta Sizer nano ZS, Malvern Instruments, Malvern, UK) were performed to estimate the vesicle size after extrusion or tip sonication. TABLE A.1 shows the obtained results.

1 Polydimethylsiloxane

Preparation method	**Average diameter** (nm)
Tip sonication	
	87.38
	87.8
	88.72
Extrusion	
Pore size: 1 µm	
	601.4
	632.6
	614.1
Pore size: 200 nm	
	158
	162.1
	161.2
Pore size: 100 nm	
	170
	173.1
	171.6

Table A.1: DLS measurements: Average diameters of DOTAP vesicles measured with DLS.

b

APPENDIX

B.1 INTRODUCTION TO GRAPHENE SOLUTION-GATED FIELD-EFFECT TRANSISTORS

B.1.1 *Fabrication*

Benno Blaschke (Walter Schottky Institut und Physik-Department, Technische Universität München) fabricated the graphene SGFETs used in this work. The schematic of the fabrication process is shown in FIGURE b.1 A. Sapphire is chosen as the substrate material, as it is stable in an electrolyte environment. On the substrate a Ti/Au layer is evaporated, the Titanium layer is needed as an adhesion layer between the substrate and the gold. The metal layer then is structured by a lift-off process. In the next step, graphene is transferred as described in SECTION 5.2.2 and structured by oxygen plasma etching and optical lithography. Afterwards, a second metal layer is evaporated and also structured by a lift-off process. As the last step SU8 photoresist is deposited. The openings for the transistor are defined by structuring the photoresist with optical lithography. For the measurements the samples are mounted on a chip carrier, bonded and sealed. As a reservoir, a glass container is glued on top. The transistors used for the experiments described in this chapter had a channel length L = 10 µm and a width W = 20 µm, as shown in FIGURE b.1 B.

B.1.2 *Working principle*

In the following, a short overview of the working principle of a graphene SGFET is given. In a SGFET the current between drain and source contact is modulated by a reference electrode through an electrolyte. FIGURE b.1 C shows the cross section of a graphene SGFET and its wiring. The metal contacts are source and drain contact, respectively. The source-drain voltage U_{DS} is applied between the two contacts. An Ag/AgCl electrode is placed in the electrolyte. To gate the graphene a voltage between the electrode and the source contact is applied. The current I_{DS} flowing between source and drain contact is measured. FIGURE b.2 shows the band structure of graphene in contact with an electrolyte. The Fermi level in the graphene shifts, when a voltage U_{GS} is applied between the graphene and the electrolyte. If a positive gate voltage is applied (FIGURE b.2 A), the Fermi level lies in the conduction band, and electrons are charge carriers. The number of electrons declines when the applied voltage is reduced. The current

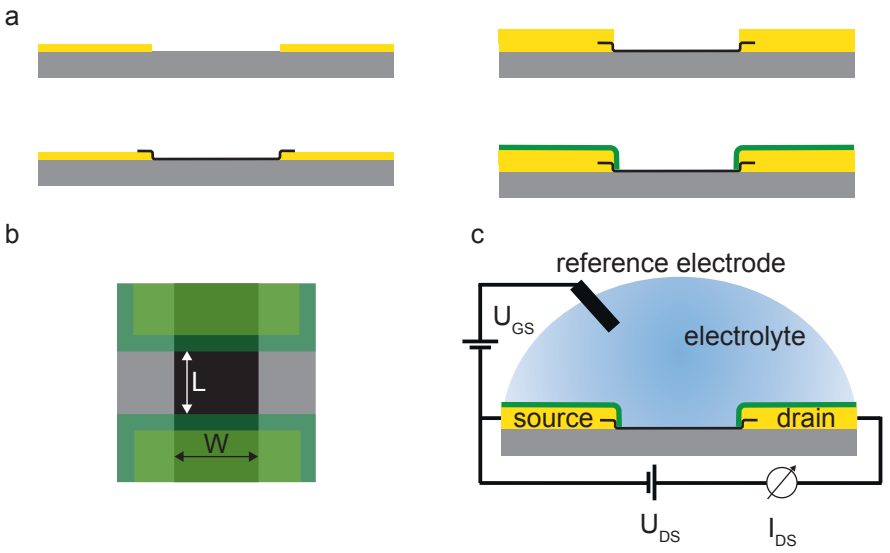

FIGURE B.1: SCHEMATIC OF A GRAPHENE SGFET. ADAPTED FROM [119].
a Production steps of the fabrication of a graphene SGFET shown in side view. Gold contacts (yellow) were deposited on sapphire substrate (grey). The graphene is transferred and structured before a second gold layer is evaporated. As last step, an insulating resist (green) is deposited and structured. **b** Schematic (top view) of a transistor with channel dimensions. Same color code as in (a). **c** Schematic wiring of a graphene SGFET.

I_{DS} decreases. When the Fermi level reaches the Dirac point, where valence and conducting band touch, the current reaches its minimum. This point also is referred to as the charge neutrality point U_{CNP}. For $U_{GS} < 0$ the Fermi level is in the valence band, and holes are induced as charge carriers. Again, I_{DS} increases with more negative U_{GS}, i.e. more holes are induced. A typical transistor curve, i.e. I_{DS} as a function of U_{GS} is shown in FIGURE b.3. The transconductance $g_m = \frac{\delta I_{DS}}{\delta U_{DS}}$ can be calculated from the curve.

B.1.3 *The ion sensitivity model*

Here a brief general overview of the model for the ion sensitivity is given. It is based on the work by Härtel et al. [193] and Heller et al. [194]. FIGURE b.4 shows the model for the ion sensitivity in the case of hole conduction, for low (grey) and high (red) ionic strength. Note that the inner and the outer Helmholtz plane are merged for simplicity. A charge in the graphene, a surface charge at the interface and the diffuse charge in the electrolyte are considered. The upper panels show the potential distribution at the interface. The lower panels show the charge density distribution; the surface charge is depicted in green. The potential U_{GS} is applied to the graphene with respect to the reference electrode. FIGURE b.4 A shows the case of a negative surface charge at the graphene electrolyte interface, where the poten-

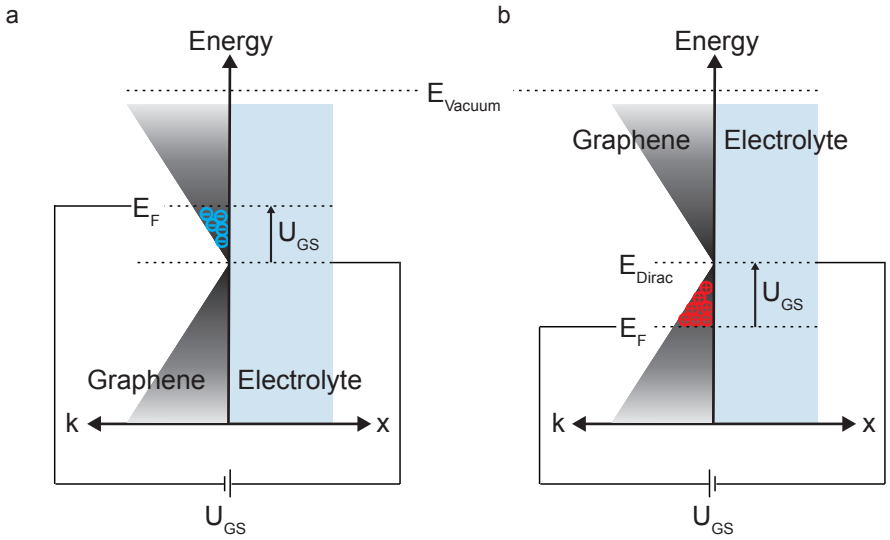

FIGURE B.2: BAND STRUCTURE OF GRAPHENE. ADAPTED FROM [192].
Schematic view of the band structure of graphene in contact with an electrolyte for **a** hole and **b** electron regime.

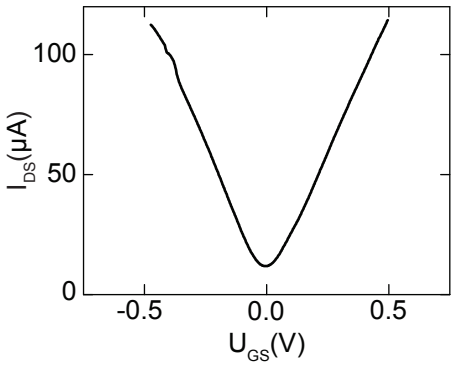

FIGURE B.3: TRANSISTOR CURVE OF GRAPHENE. ADAPTED FROM [119].
A typical transistor curve of graphene. The charge neutrality point U_{CNP}, i.e. the voltage where the current reaches its minimum was shifted to 0 V.

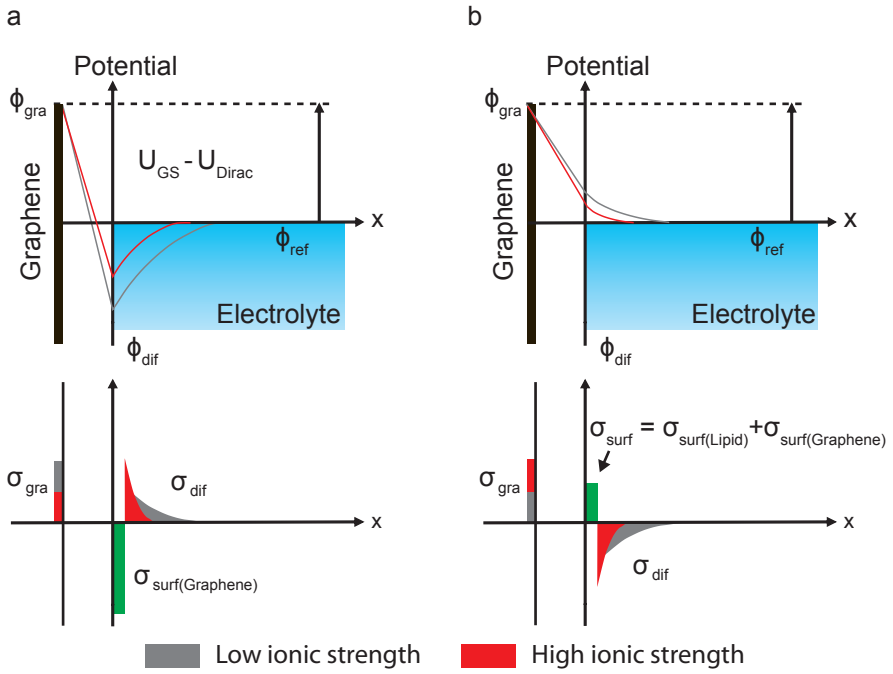

FIGURE B.4: THE ION SENSITIVITY MODEL. ADAPTED FROM [193].
Potential profiles (top) and charge distribution (bottom) at the graphene/electrolyte interface for **a** a negative surface charge in the hole conducion regime and **b** a positive surface charge in the hole conduction regime.

tial drops from ϕ_{gra} to a negative value ϕ_{dif} at the surface to then exponentially decay towards the potential of the reference electrode ϕ_{ref}. ϕ_{dif} becomes more positive for higher ionic strength because the diffuse charge layer is increased. With the potential difference $\Delta\phi = \phi_{gra} - \phi_{dif}$ being smaller, also the graphene charge lowers. This results in a lower current I_{DS}. For the electron regime, the current increases. The transfer curve is shifted towards more negative values of U_{GS}. FIGURE B.4 B shows the profiles after the formation of a cationic DOTAP lipid layer. The surface charge is overcompensated and becomes positive. In this case, the surface potential is lowered due to the increased ion concentration. The current increases in the hole regime and decreases in the electron regime, respectively. The transfer curve is shifted towards more positive voltages.

C

APPENDIX

C.1 SAMPLE PREPARATION

C.1.1 *Neutron reflectometry experiments*

Silicon and quartz blocks were cleaned in chloroform, acetone, ethanol and purified water in an ultrasonic bath for 10 minutes each step. To sterilize all components of the chamber, they were covered in 75 % ethanol for 1 hour under sterile conditions. Afterwards, they were flushed with sterile purified water and dried under sterile conditions. Prior to seeding of the cells, the mounted chamber was filled with medium and incubated for about 30 minutes.

C.1.2 *X-ray reflectometry experiments*

Dies were cleaned in chloroform, acetone, ethanol and purified water in an ultrasonic bath for 10 minutes each step. To sterilize all components of the chamber, they were covered in 75 % ethanol for 1 hour under sterile conditions. Afterwards, they were flushed with sterile purified water and dried under sterile conditions. Prior to seeding of the cells, the mounted chamber was filled with medium and incubated for about 30 minutes. All medium exchanges were performed under sterile conditions.

C.1.3 *Cell culture*

MDCK-II cell line was cultured in minimal essential medium (c-c-pro) containing 2mM L-glutamine and 10 % fetal calf serum at 37 °C and 5 % CO_2. Cells were trypsinated once they have reached a confluence of 80 % and were seeded either in a cell culture flask for further subculture or seeded in the neutron sample chamber at 50 % cell density in growth medium. After 24 hours they have reached full confluence and the medium was exchanged to Leibovitz's L15 medium with 2 mM L-glutamine and 10 % fetal calf serum. L15 was used as a powder to have the possibility to solve it in either only H_2O or a mixture of D_2O and H_2O. A toxicity curve was made and the highest possible D_2O/H_2O mixture without visible toxic effects was used for the experiments.

LIST OF FIGURES

LIST OF TABLES

BIBLIOGRAPHY

[1] H. P. Wacklin. "Neutron reflection from supported lipid membranes." In: *Current Opinion in Colloid & Interface Science* 15.6 (2010), 445–454.

[2] O. G. Mouritsen. *Life-as a matter of fat*. Springer, 2005.

[3] T. Nylander, R. A. Campbell, P. Vandoolaeghe, M. Cárdenas, P. Linse, and A. R. Rennie. "Neutron reflectometry to investigate the delivery of lipids and DNA to interfaces." In: *Biointerphases* 3.2 (2008), FB64–FB82.

[4] L. Pocivavsek, A. Junghans, N. Zebda, K. Birukov, and J. Majewski. "Tuning endothelial monolayer adhesion: a neutron reflectivity study." In: *American Journal of Physiology-Lung Cellular and Molecular Physiology* 306.1 (2013), pp. L1–L9.

[5] G. Fragneto and M. Rheinstädter. "Structural and dynamical studies from bio-mimetic systems: an overview." In: *Comptes Rendus Physique* 8.7 (2007), pp. 865–883.

[6] E. Sackmann. "Supported membranes: scientific and practical applications." In: *Science-AAAS-Weekly Paper Edition* 271.5245 (1996), pp. 43–48.

[7] G. Fragneto. "Neutrons and model membranes." In: *The European Physical Journal Special Topics* 213.1 (2012), pp. 327–342.

[8] *The Nobel Prize in Chemistry 2014*. `https://www.nobelprize.org/nobel_prizes/chemistry/laureates/2014/`. 26 March 2018.

[9] *The Nobel Prize in Physics 1914*. `https://www.nobelprize.org/nobel_prizes/physics/laureates/1914/`. 26 March 2018.

[10] *The Nobel Prize in Physics 1935*. `https://www.nobelprize.org/nobel_prizes/physics/laureates/1935/`. 26 March 2018.

[11] J. Penfold. "Neutron reflectivity and soft condensed matter." In: *Current Opinion in Colloid & Interface Science* 7.1 (2002), pp. 139–147.

[12] *The Nobel Prize in Physics 2010*. `https://www.nobelprize.org/nobel_prizes/physics/laureates/2010/`. 02 February 2018.

[13] A. J. Engler, M. A. Griffin, S. Sen, C. G. Bönnemann, H. L. Sweeney, and D. E. Discher. "Myotubes differentiate optimally on substrates with tissue-like stiffness." In: *pathological implications for soft or stiff microenvironments* 166.6 (2004), pp. 877–887.

[14] C.-M. Lo, H.-B. Wang, M. Dembo, and Y.-l. Wang. "Cell Movement Is Guided by the Rigidity of the Substrate." In: *Biophysical Journal* 79.1 (2000), pp. 144–152.

[15] Alexander D. Bershadsky, Nathalie Q. Balaban, and B. Geiger. "Adhesion-Dependent Cell Mechanosensitivity." In: *Annual Review of Cell and Developmental Biology* 19.1 (2003), pp. 677–695.

[16] E. Cukierman, R. Pankov, D. R. Stevens, and K. M. Yamada. "Taking Cell-Matrix Adhesions to the Third Dimension." In: *Science* 294.5547 (2001), pp. 1708–1712.

[17] D. E. Discher, P. Janmey, and Y.-l. Wang. "Tissue cells feel and respond to the stiffness of their substrate." In: *Science* 310.5751 (2005), pp. 1139–1143.

[18] D. E. Discher, D. J. Mooney, and P. W. Zandstra. "Growth factors, matrices, and forces combine and control stem cells." In: *Science* 324.5935 (2009), pp. 1673–1677.

[19] R. Bainer and V. Weaver. "Strength Under Tension." In: *science* 341.6149 (2013), pp. 965–966.

[20] D. E. Discher, L. Smith, S. Cho, M. Colasurdo, A. J. García, and S. Safran. "Matrix Mechanosensing: From Scaling Concepts in Omics Data to Mechanisms in the Nucleus, Cancer, and Regeneration." In: *Annual review of biophysics* 46.1 (2017).

[21] R. W. Tilghman, C. R. Cowan, J. D. Mih, Y. Koryakina, D. Gioeli, J. K. Slack-Davis, B. R. Blackman, D. J. Tschumperlin, and J. T. Parsons. "Matrix Rigidity Regulates Cancer Cell Growth and Cellular Phenotype." In: *PLoS ONE* 5.9 (2010), e12905.

[22] F. Rehfeldt, A. J. Engler, A. Eckhardt, F. Ahmed, and D. E. Discher. "Cell responses to the mechanochemical microenvironment—implications for regenerative medicine and drug delivery." In: *Advanced drug delivery reviews* 59.13 (2007), pp. 1329–1339.

[23] M. Caffrey and J. Wang. "Membrane-structure studies using x-ray standing waves." In: *Annual review of biophysics and biomolecular structure* 24.1 (1995), pp. 351–377.

[24] E. Gorter and F. Grendel. "On bimolecular layers of lipoids on the chromocytes of the blood." In: *Journal of Experimental Medicine* 41.4 (1925), pp. 439–443.

[25] S. J. Singer and G. L. Nicolson. "The fluid mosaic model of the structure of cell membranes." In: *Science* 175.4023 (1972), pp. 720–731.

[26] J. Israelachvili. *Light Transducing Membranes: Structure, Function and Evolution (DW Deamer, ed.)* Academic Press, 1978.

[27] E. Sackmann and R. Merkel. *Lehrbuch der Biophysik*. Wiley-VCH, 2010.

[28] D. Brüggemann, J. P. Frohnmayer, and J. P. Spatz. "Model systems for studying cell adhesion and biomimetic actin networks." In: *Beilstein journal of nanotechnology* 5 (2014), 1193–1202.

[29] M. Loose and P. Schwille. "Biomimetic membrane systems to study cellular organization." In: *Journal of structural biology* 168.1 (2009), 143–151.

[30] E. T. Castellana and P. S. Cremer. "Solid supported lipid bilayers: From biophysical studies to sensor design." In: *Surface Science Reports* 61.10 (2006), 429–444.

[31] M. Magliulo, A. Mallardi, M. Y. Mulla, S. Cotrone, B. R. Pistillo, P. Favia, I. Vikholm-Lundin, G. Palazzo, and L. Torsi. "Electrolyte-gated organic field-effect transistor sensors based on supported biotinylated phospholipid bilayer." In: *Advanced materials (Deerfield Beach, Fla.)* 25.14 (2013), 2090–2094.

[32] N. Kučerka, J. F. Nagle, J. N. Sachs, S. E. Feller, J. Pencer, A. Jackson, and J. Katsaras. "Lipid Bilayer Structure Determined by the Simultaneous Analysis of Neutron and X-Ray Scattering Data." In: *Biophysical Journal* 95.5 (2008), pp. 2356–2367.

[33] B. Alberts, D. Bray, J. Lewis, M. Raff, K. Roberts, and J. Watson. *Molecular Biology of the Cell*. Garland.

[34] J. Nissen, K. Jacobs, and J. O. Radler. "Interface dynamics of lipid membrane spreading on solid surfaces." In: *Physical review letters* 86.9 (2001), 1904–1907.

[35] J. F. Nagle and S. Tristram-Nagle. "Structure of lipid bilayers." In: *Biochimica et Biophysica Acta (BBA) - Reviews on Biomembranes* 1469.3 (2000), 159–195.

[36] D. Lingwood and K. Simons. "Lipid rafts as a membrane-organizing principle." In: *science* 327.5961 (2010), pp. 46–50.

[37] B. Sanii and A. N. Parikh. "Surface-energy dependent spreading of lipid monolayers and bilayers." In: *Soft matter* 3.8 (2007), p. 974.

[38] C. A. Keller and B. Kasemo. "Surface Specific Kinetics of Lipid Vesicle Adsorption Measured with a Quartz Crystal Microbalance." In: *Biophysical Journal* 75.3 (1998), 1397–1402.

[39] J. Penfold and R. K. Thomas. "Neutron reflectivity and small angle neutron scattering: An introduction and perspective on recent progress." In: *Current Opinion in Colloid & Interface Science* 19.3 (2014), pp. 198–206.

[40] T. G. Pomorski, T. Nylander, and M. Cárdenas. "Model cell membranes: Discerning lipid and protein contributions in shaping the cell." In: *Advances in Colloid and Interface Science* 205 (2014), pp. 207–220.

[41] M. K. Jain and R. C. Wagner. *Introduction to biological membranes*. Report. Wiley New York, 1988.

[42] M. L. Wagner and L. K. Tamm. "Tethered Polymer-Supported Planar Lipid Bilayers for Reconstitution of Integral Membrane Proteins: Silane-Polyethyleneglycol-Lipid as a Cushion and Covalent Linker." In: *Biophysical Journal* 79.3 (2000), pp. 1400–1414.

[43] E. Sackmann and M. Tanaka. "Supported membranes on soft polymer cushions: fabrication, characterization and applications." In: *Trends in biotechnology* 18.2 (2000), pp. 58–64.

[44] M. Tanaka and E. Sackmann. "Polymer-supported membranes as models of the cell surface." In: *Nature* 437.7059 (2005), p. 656.

[45] W. Knoll, C. Frank, C. Heibel, R. Naumann, A. Offenhäusser, J. Rühe, E. Schmidt, W. Shen, and A. Sinner. "Functional tethered lipid bilayers." In: *Reviews in Molecular Biotechnology* 74.3 (2000), pp. 137–158.

[46] Y.-H. M. Chan and S. G. Boxer. "Model membrane systems and their applications." In: *Current Opinion in Chemical Biology* 11.6 (2007), pp. 581–587.

[47] S. Garg, J. Rühe, K. Lüdtke, R. Jordan, and C. A. Naumann. "Domain registration in raft-mimicking lipid mixtures studied using polymer-tethered lipid bilayers." In: *Biophysical journal* 92.4 (2007), pp. 1263–1270.

[48] T. Charitat, E. Bellet-Amalric, G. Fragneto, and F. Graner. "Adsorbed and free lipid bilayers at the solid-liquid interface." In: *The European Physical Journal B-Condensed Matter and Complex Systems* 8.4 (1999), pp. 583–593.

[49] A. V. Hughes, J. R. Howse, A. Dabkowska, R. A. Jones, M. J. Lawrence, and S. J. Roser. "Floating lipid bilayers deposited on chemically grafted phosphatidylcholine surfaces." In: *Langmuir* 24.5 (2008), pp. 1989–1999.

[50] S. J. Johnson, T. M. Bayerl, D. C. McDermott, G. W. Adam, A. R. Rennie, R. K. Thomas, and E. Sackmann. "Structure of an adsorbed dimyristoylphosphatidylcholine bilayer measured with specular reflection of neutrons." In: *Biophysical journal* 59.2 (1991), pp. 289–294.

[51] S. Hertrich, F. Stetter, A. Rühm, T. Hugel, and B. Nickel. "Highly hydrated deformable polyethylene glycol-tethered lipid bilayers." In: *Langmuir : the ACS journal of surfaces and colloids* 30.31 (2014), 9442–9447.

[52] J. Daillant, E. Bellet-Amalric, A. Braslau, T. Charitat, G. Fragneto, F. Graner, S. Mora, F. Rieutord, and B. Stidder. "Structure and fluctuations of a single floating lipid bilayer." In: *Proceedings of the National Academy of Sciences of the United States of America* 102.33 (2005), pp. 11639–11644.

[53] F. Sebastiani, R. Harvey, S. Khanniche, J.-B. Artero, M. Haertlein, and G. Fragneto. "Diffraction studies on natural and model lipid bilayers." In: *The European Physical Journal Special Topics* 213.1 (2012), pp. 355–365.

[54] B. Demé, D. Hess, M. Tristl, L.-T. Lee, and E. Sackmann. "Binding of actin filaments to charged lipid monolayers: Film balance experiments combined with neutron reflectivity." In: *The European Physical Journal E* 2.2 (2000), pp. 125–136.

[55] G. Fragneto, E. Bellet-Amalric, T. Charitat, P. Dubos, F. Graner, and L. Perino-Galice. "Neutron and X-ray reflectivity studies at solid–liquid interfaces: the interaction of a peptide with model membranes." In: *Physica B: Condensed Matter* 276 (2000), pp. 501–502.

[56] D. Di Silvio, M. Maccarini, R. Parker, A. Mackie, G. Fragneto, and F. B. Bombelli. "The effect of the protein corona on the interaction between nanoparticles and lipid bilayers." In: *Journal of colloid and interface science* 504 (2017), pp. 741–750.

[57] A. Luchini, Y. Gerelli, G. Fragneto, T. Nylander, G. K. Pálsson, M.-S. Appavou, and L. Paduano. "Neutron Reflectometry reveals the interaction between functionalized SPIONs and the surface of lipid bilayers." In: *Colloids and Surfaces B: Biointerfaces* 151 (2017), pp. 76–87.

[58] A. Koutsioubas, M.-S. Appavou, and D. Lairez. "Time-Resolved Neutron Reflectivity during Supported Membrane Formation by Vesicle Fusion." In: *Langmuir* 33.40 (2017), pp. 10598–10605.

[59] H. P. Wacklin and R. K. Thomas. "Spontaneous Formation of Asymmetric Lipid Bilayers by Adsorption of Vesicles." In: *Langmuir* 23.14 (2007), pp. 7644–7651.

[60] S. Stanglmaier, S. Hertrich, K. Fritz, J.-F. Moulin, M. Haese-Seiller, J. Radler, and B. Nickel. "Asymmetric distribution of anionic phospholipids in supported lipid bilayers." In: *Langmuir* 28.29 (2012), pp. 10818–10821.

[61] A. de Ghellinck, C. Shen, G. Fragneto, and B. Klösgen. "Probing the position of resveratrol in lipid bilayers: A neutron reflectivity study." In: *Colloids and Surfaces B: Biointerfaces* 134 (2015), pp. 65–72.

[62] H. P. Wacklin, B. B. Bremec, M. Moulin, N. Rojko, M. Haertlein, T. Forsyth, G. Anderluh, and R. S. Norton. "Neutron reflection study of the interaction of the eukaryotic pore-forming actinoporin equinatoxin II with lipid membranes reveals intermediate states in pore formation." In: *Biochimica et Biophysica Acta (BBA)-Biomembranes* 1858.4 (2016), pp. 640–652.

[63] M. Schalke and M. Lösche. "Structural models of lipid surface monolayers from X-ray and neutron reflectivity measurements." In: *Advances in colloid and interface science* 88.1-2 (2000), pp. 243–274.

[64] G. L. Gaines. *Insoluble monolayers at liquid-gas interfaces*. Academic Press, 1966.

[65] L. K. Tamm and H. M. McConnell. "Supported phospholipid bilayers." In: *Biophysical journal* 47.1 (1985), pp. 105–113.

[66] J. Raedler, H. Strey, and E. Sackmann. "Phenomenology and Kinetics of Lipid Bilayer Spreading on Hydrophilic Surfaces." In: *Langmuir* 11.11 (1995), 4539–4548.

[67] A. R. Bausch, F. Ziemann, A. A. Boulbitch, K. Jacobson, and E. Sackmann. "Local Measurements of Viscoelastic Parameters of Adherent Cell Surfaces by Magnetic Bead Microrheometry." In: *Biophysical Journal* 75.4 (1998), pp. 2038–2049.

[68] A. S. Smith and E. Sackmann. "Progress in mimetic studies of cell adhesion and the mechanosensing." In: *ChemPhysChem* 10.1 (2009), pp. 66–78.

[69] P. Bongrand. "Ligand-receptor interactions." In: *Reports on Progress in Physics* 62.6 (1999), p. 921.

[70] A. Zidovska and E. Sackmann. "Brownian motion of nucleated cell envelopes impedes adhesion." In: *Physical review letters* 96.4 (2006), p. 048103.

[71] A. Pierres, A.-M. Benoliel, D. Touchard, and P. Bongrand. "How cells tiptoe on adhesive surfaces before sticking." In: *Biophysical journal* 94.10 (2008), pp. 4114–4122.

[72] E. Reister-Gottfried, K. Sengupta, B. Lorz, E. Sackmann, U. Seifert, and A.-S. Smith. "Dynamics of Specific Vesicle-Substrate Adhesion: From Local Events to Global Dynamics." In: *Physical Review Letters* 101.20 (2008), p. 208103.

[73] G. Bell. "Models for the specific adhesion of cells to cells." In: *Science* 200.4342 (1978), pp. 618–627.

[74] A.-S. Smith and U. Seifert. "Vesicles as a model for controlled (de-) adhesion of cells: a thermodynamic approach." In: *Soft Matter* 3.3 (2007), pp. 275–289.

[75] E. Sackmann and R. F. Bruinsma. "Cell adhesion as wetting transition?" In: *ChemPhysChem* 3.3 (2002), pp. 262–269.

[76] E. Sackmann and A.-S. Smith. "Physics of cell adhesion: some lessons from cell-mimetic systems." In: *Soft matter* 10.11 (2014), pp. 1644–1659.

[77] R. Bruinsma and E. Sackmann. "Bioadhesion and the dewetting transition." In: *Comptes Rendus de l'Académie des Sciences-Series IV-Physics-Astrophysics* 2.6 (2001), pp. 803–815.

[78] L. Fisher. "Force between biological surfaces." In: *Journal of the Chemical Society, Faraday Transactions* 89.15 (1993), pp. 2567–2582.

[79] J. N. Israelachvili and H. Wennerstroem. "Entropic forces between amphiphilic surfaces in liquids." In: *The Journal of Physical Chemistry* 96.2 (1992), pp. 520–531.

[80] D. Cuvelier, M. Théry, Y.-S. Chu, S. Dufour, J.-P. Thiéry, M. Bornens, P. Nassoy, and L. Mahadevan. "The Universal Dynamics of Cell Spreading." In: *Current Biology* 17.8 (2007), pp. 694–699.

[81] R. Bruinsma, A. Behrisch, and E. Sackmann. "Adhesive switching of membranes: experiment and theory." In: *Physical Review E* 61.4 (2000), p. 4253.

[82] S. Marx, J. Schilling, E. Sackmann, and R. Bruinsma. "Helfrich Repulsion and Dynamical Phase Separation of Multicomponent Lipid Bilayers." In: *Physical Review Letters* 88.13 (2002), p. 138102.

[83] J. Raedler and E. Sackmann. "On the measurement of weak repulsive and frictional colloidal forces by reflection interference contrast microscopy." In: *Langmuir* 8.3 (1992), pp. 848–853.

[84] J. Rädler and E. Sackmann. "Imaging optical thicknesses and separation distances of phospholipid vesicles at solid surfaces." In: *Journal de Physique II* 3.5 (1993), pp. 727–748.

[85] C. Monzel, S. F. Fenz, M. Giesen, R. Merkel, and K. Sengupta. "Mapping fluctuations in biomembranes adhered to micropatterns." In: *Soft Matter* 8.22 (2012), pp. 6128–6138.

[86] A. Curtis. "The mechanism of adhesion of cells to glass: a study by interference reflection microscopy." In: *The Journal of cell biology* 20.2 (1964), pp. 199–215.

[87] K.-F. Giebel, C. Bechinger, S. Herminghaus, M. Riedel, P. Leiderer, U. Weiland, and M. Bastmeyer. "Imaging of cell/substrate contacts of living cells with surface plasmon resonance microscopy." In: *Biophysical journal* 76.1 (1999), pp. 509–516.

[88] L. Limozin and K. Sengupta. "Quantitative reflection interference contrast microscopy (RICM) in soft matter and cell adhesion." In: *ChemPhysChem* 10.16 (2009), pp. 2752–2768.

[89] C. Izzard and L. R. Lochner. "Cell-to-substrate contacts in living fibroblasts: an interference reflexion study with an evaluation of the technique." In: *Journal of cell science* 21.1 (1976), pp. 129–159.

[90] D. Gingell and I. Todd. "Interference reflection microscopy. A quantitative theory for image interpretation and its application to cell-substratum separation measurement." In: *Biophysical Journal* 26.3 (1979), pp. 507–526.

[91] H. Verschueren. "Interference reflection microscopy in cell biology: methodology and applications." In: *Journal of Cell Science* 75.1 (1985), pp. 279–301.

[92] M. Schindl, E. Wallraff, B. Deubzer, W. Witke, G. Gerisch, and E. Sackmann. "Cell-substrate interactions and locomotion of Dictyostelium wild-type and mutants defective in three cytoskeletal proteins: a study using quantitative reflection interference contrast microscopy." In: *Biophysical Journal* 68.3 (1995), pp. 1177–1190.

[93] K. Klein, C. E. Rommel, V. C. Hirschfeld-Warneken, and J. P. Spatz. "Cell membrane topology analysis by RICM enables marker-free adhesion strength quantification." In: *Biointerphases* 8.1 (2013), p. 28.

[94] D. Braun and P. Fromherz. "Fluorescence interference-contrast microscopy of cell adhesion on oxidized silicon." In: *Applied Physics A: Materials Science & Processing* 65.4 (1997), pp. 341–348.

[95] D. Braun and P. Fromherz. "Fluorescence Interferometry of Neuronal Cell Adhesion on Microstructured Silicon." In: *Physical Review Letters* 81.23 (1998), pp. 5241–5244.

[96] R. Parthasarathy and J. T. Groves. "Optical techniques for imaging membrane topography." In: *Cell biochemistry and biophysics* 41.3 (2004), pp. 391–414.

[97] P. Fromherz, A. Offenhausser, T. Vetter, and J. Weis. "A neuron-silicon junction: a Retzius cell of the leech on an insulated-gate field-effect transistor." In: *Science* 252.5010 (1991), pp. 1290–1293.

[98] P. Fromherz and A. Stett. "Silicon-neuron junction: capacitive stimulation of an individual neuron on a silicon chip." In: *Physical Review Letters* 75.8 (1995), p. 1670.

[99] P. Fromherz. "Interfacing neurons and silicon by electrical induction." In: *Berichte der Bunsengesellschaft für physikalische Chemie* 100.7 (1996), pp. 1093–1102.

[100] P. Fromherz. "Electrical interfacing of nerve cells and semiconductor chips." In: *ChemPhysChem* 3.3 (2002), pp. 276–284.

[101] D. Axelrod. "Cell-substrate contacts illuminated by total internal reflection fluorescence." In: *The Journal of cell biology* 89.1 (1981), pp. 141–145.

[102] J. S. Burmeister, L. A. Olivier, W. M. Reichert, and G. A. Truskey. "Application of total internal reflection fluorescence microscopy to study cell adhesion to biomaterials." In: *Biomaterials* 19.4-5 (1998), pp. 307–325.

[103] D. K. Hoover, E.-J. Lee, and M. N. Yousaf. "Total internal reflection fluorescence microscopy of cell adhesion on patterned self-assembled monolayers on gold." In: *Langmuir* 25.5 (2009), pp. 2563–2566.

[104] M. J. Paszek, C. C. DuFort, M. G. Rubashkin, M. W. Davidson, K. S. Thorn, J. T. Liphardt, and V. M. Weaver. "Scanning angle interference microscopy reveals cell dynamics at the nanoscale." In: *Nature Methods* 9 (2012), p. 825.

[105] M. J. Paszek et al. "The cancer glycocalyx mechanically primes integrin-mediated growth and survival." In: *Nature* 511.7509 (2014), pp. 319–325.

[106] J. Als-Nielsen and D. McMorrow. *Elements of modern X-ray physics*. John Wiley & Sons, 2011.

[107] P. S. Pershan. "X-ray or neutron reflectivity: Limitations in the determination of interfacial profiles." In: *Phys. Rev. E* 50 (1994), 2369–2373.

[108] T. Skarzynski. "Collecting data in the home laboratory: evolution of X-ray sources, detectors and working practices." In: *Acta Crystallographica Section D: Biological Crystallography* 69.7 (2013), pp. 1283–1288.

[109] B. E. Warren. *X-ray Diffraction*. Courier Corporation, 1969.

[110] J. Penfold and R. Thomas. "The application of the specular reflection of neutrons to the study of surfaces and interfaces." In: *Journal of Physics: Condensed Matter* 2.6 (1990), p. 1369.

[111] A. Nelson. "Co-refinement of multiple-contrast neutron/X-ray reflectivity data using MOTOFIT." In: *J. Appl. Crystallogr.* 39.2 (2006), 273–276.

[112] L. Nevot and P. Croce. "Caractérisation des surfaces par réflexion rasante de rayons X. Application à l'étude du polissage de quelques verres silicates." In: *Revue de Physique appliquée* 15.3 (1980), pp. 761–779.

[113] O. Heavens. "Optical properties of thin films." In: *Reports on Progress in Physics* 23.1 (1960), p. 1.

[114] H. Kiessig. "Interferenz von Röntgenstrahlen an dünnen Schichten." In: *Annalen der Physik* 402.7 (1931), pp. 769–788.

[115] L. G. Parratt. "Surface Studies of Solids by Total Reflection of X-Rays." In: *Physical Review* 95/2 (1954), 359–369.

[116] M. Ober. "A Line-collimated Small-Angle X-ray Scattering Setup: Construction, Calibration and Applications." PhD thesis. 2017.

[117] C. Dirscherl. "Structural and Dynamic Changes in Light-Switchable Lipid Membranes: A Combined X-Ray and UV-Vis Study." Master Thesis. 2016.

[118] F. Salah, B. Harzallah, and A. van der Lee. "Data reduction practice in X-ray reflectometry." In: *Journal of Applied Crystallography* 40.5 (2007), 813–819.

[119] B. M. Blaschke, P. Böhm, S. Drieschner, B. Nickel, and J. A. Garrido. "Lipid monolayer formation and lipid exchange monitored by a graphene field-effect transistor." In: *Langmuir* (2018).

[120] P. K. Ang, M. Jaiswal, C. H. Y. X. Lim, Y. Wang, J. Sankaran, A. Li, C. T. Lim, T. Wohland, O. Barbaros, and K. P. Loh. "A bioelectronic platform using a graphene-lipid bilayer interface." In: *ACS Nano* 4.12 (2010), 7387–7394.

[121] Y. Y. Wang, T. D. Pham, K. Zand, J. Li, and P. J. Burke. "Charging the quantum capacitance of graphene with a single biological ion channel." In: *ACS Nano* 8.5 (2014), 4228–4238.

[122] S. R. Tabaei, W. B. Ng, S.-J. Cho, and N.-J. Cho. "Controlling the Formation of Phospholipid Monolayer, Bilayer, and Intact Vesicle Layer on Graphene." In: *ACS applied materials & interfaces* 8.18 (2016), 11875–11880.

[123] M. Hirtz, A. Oikonomou, T. Georgiou, H. Fuchs, and A. Vijayaraghavan. "Multiplexed biomimetic lipid membranes on graphene by dip-pen nanolithography." In: *Nature communications* 4 (2013), p. 2591.

[124] J. Kim, L. J. Cote, F. Kim, and J. Huang. "Visualizing graphene based sheets by fluorescence quenching microscopy." In: *Journal of the American Chemical Society* 132.1 (2010), 260–267.

[125] R. S. Swathi and K. L. Sebastian. "Resonance energy transfer from a dye molecule to graphene." In: *The Journal of chemical physics* 129.5 (2008), p. 054703.

[126] R. P. Richter, R. Bérat, and A. R. Brisson. "Formation of solid-supported lipid bilayers: an integrated view." In: *Langmuir : the ACS journal of surfaces and colloids* 22.8 (2006), 3497–3505.

[127] Y. H. Soung, S. Ford, V. Zhang, and J. Chung. "Exosomes in Cancer Diagnostics." In: *Cancers* 9.1 (2017).

[128] A. K. Geim. "Graphene prehistory." In: *Physica Scripta* 2012.T146 (2012), p. 014003.

[129] P. R. Wallace. "The band theory of graphite." In: *Physical Review* 71.9 (1947), p. 622.

[130] R. R. Nair, P. Blake, A. N. Grigorenko, K. S. Novoselov, T. J. Booth, T. Stauber, N. M. Peres, and A. K. Geim. "Fine structure constant defines visual transparency of graphene." In: *Science* 320.5881 (2008), pp. 1308–1308.

[131] A. C. Ferrari et al. "Science and technology roadmap for graphene, related two-dimensional crystals, and hybrid systems." In: *Nanoscale* 7.11 (2015), pp. 4598–4810.

[132] M. J. Allen, V. C. Tung, and R. B. Kaner. "Honeycomb carbon: a review of graphene." In: *Chemical reviews* 110.1 (2009), pp. 132–145.

[133] K. S. Novoselov, A. K. Geim, S. V. Morozov, D. Jiang, M. I. Katsnelson, I. V. Grigorieva, S. V. Dubonos, and A. A. Firsov. "Two-dimensional gas of massless Dirac fermions in graphene." In: *Nature* 438 (2005), p. 197.

[134] S. Bae, H. Kim, Y. Lee, X. Xu, J.-S. Park, Y. Zheng, J. Balakrishnan, T. Lei, H. R. Kim, and Y. I. Song. "Roll-to-roll production of 30-inch graphene films for transparent electrodes." In: *Nature nanotechnology* 5.8 (2010), p. 574.

[135] B. M. Blaschke, M. Lottner, S. Drieschner, A. B. Calia, K. Stoiber, L. Rousseau, G. Lissourges, and J. A. Garrido. "Flexible graphene transistors for recording cell action potentials." In: *2D Materials* 3.2 (2016), p. 25007.

[136] X. Li, L. Colombo, and R. S. Ruoff. "Synthesis of graphene films on copper foils by chemical vapor deposition." In: *Advanced Materials* 28.29 (2016), pp. 6247–6252.

[137] L. M. C. Lima, W. Fu, L. Jiang, A. Kros, and G. F. Schneider. "Graphene-stabilized lipid monolayer heterostructures: A novel biomembrane superstructure." In: *Nanoscale* 8.44 (2016), 18646–18653.

[138] Y. Dan, Y. Lu, N. J. Kybert, Z. Luo, and A. T. C. Johnson. "Intrinsic response of graphene vapor sensors." In: *Nano letters* 9.4 (2009), 1472–1475.

[139] C. Reich, M. B. Hochrein, B. Krause, and B. Nickel. "A microfluidic setup for studies of solid-liquid interfaces using x-ray reflectivity and fluorescence microscopy." In: *Review of Scientific Instruments* 76.9 (2005), p. 095103.

[140] W. Li, J. K. Chung, Y. K. Lee, and J. T. Groves. "Graphene-Templated Supported Lipid Bilayer Nanochannels." In: *Nano Letters* 16.8 (2016), 5022–5026.

[141] G. Hong, Y. Han, T. M. Schutzius, Y. Wang, Y. Pan, M. Hu, J. Jie, C. S. Sharma, U. Müller, and D. Poulikakos. "On the Mechanism of Hydrophilicity of Graphene." In: *Nano letters* 16.7 (2016), 4447–4453.

[142] S. Gritsch, P. Nollert, F. Jähnig, and E. Sackmann. "Impedance Spectroscopy of Porin and Gramicidin Pores Reconstituted into Supported Lipid Bilayers on Indium- Tin-Oxide Electrodes." In: *Langmuir* 14.11 (1998), pp. 3118–3125.

[143] R. Naumann, T. Baumgart, P. Gräber, A. Jonczyk, A. Offenhäusser, and W. Knoll. "Proton transport through a peptide-tethered bilayer lipid membrane by the H+-ATP synthase from chloroplasts measured by impedance spectroscopy." In: *Biosensors and bioelectronics* 17.1-2 (2002), pp. 25–34.

[144] J. R. MacDonald. *Impedance spectroscopy*. Wiley New York etc, 1987.

[145] S. Drieschner, A. Guimerà, R. G. Cortadella, D. Viana, E. Makrygiannis, B. M. Blaschke, J. Vieten, and J. A. Garrido. "Frequency response of electrolyte-gated graphene electrodes and transistors." In: *Journal of Physics D: Applied Physics* 50.9 (2017), p. 095304.

[146] M. Dankerl et al. "Graphene Solution-Gated Field-Effect Transistor Array for Sensing Applications." In: *Advanced Functional Materials* 20.18 (2010), pp. 3117–3124.

[147] H. Ji, X. Zhao, Z. Qiao, J. Jung, Y. Zhu, Y. Lu, L. L. Zhang, A. H. MacDonald, and R. S. Ruoff. "Capacitance of carbon-based electrical double-layer capacitors." In: *Nature Communications* 5 (2014), p. 3317.

[148] G. Wiegand, N. Arribas-Layton, H. Hillebrandt, E. Sackmann, and P. Wagner. "Electrical Properties of Supported Lipid Bilayer Membranes." In: *The Journal of Physical Chemistry B* 106.16 (2002), 4245–4254.

[149] T. Schubert, G. Steinhoff, H.-G. v. Ribbeck, M. Stutzmannn, M. Eickhoff, and M. Tanaka. "Gallium nitride electrodes for membrane-based electrochemical biosensors." In: *The European physical journal. E, Soft matter* 30.2 (2009), 233–238.

[150] L. H. Hess, M. Seifert, and J. A. Garrido. "Graphene Transistors for Bioelectronics." In: *Proceedings of the IEEE* 101.7 (2013), 1780–1792.

[151] W. Fu et al. "Electrolyte gate dependent high-frequency measurement of graphene field-effect transistor for sensing applications." In: *Applied Physics Letters* 104.1 (2014), p. 013102.

[152] W. Fu, L. Feng, D. Mayer, G. Panaitov, D. Kireev, A. Offenhäusser, and H.-J. Krause. "Electrolyte-Gated Graphene Ambipolar Frequency Multipliers for Biochemical Sensing." In: *Nano Letters* (2016).

[153] X. Wang, L. Zhi, and K. Müllen. "Transparent, Conductive Graphene Electrodes for Dye-Sensitized Solar Cells." In: *Nano Letters* 8.1 (2008), 323–327.

[154] P. Blake et al. "Graphene-based liquid crystal device." In: *Nano letters* 8.6 (2008), 1704–1708.

[155] S. J. Park, O. S. Kwon, S. H. Lee, H. S. Song, T. H. Park, and J. Jang. "Ultrasensitive flexible graphene based field-effect transistor (FET)-type bioelectronic nose." In: *Nano letters* 12.10 (2012), 5082–5090.

[156] T. Cohen-Karni, Q. Qing, Q. Li, Y. Fang, and C. M. Lieber. "Graphene and nanowire transistors for cellular interfaces and electrical recording." In: *Nano letters* 10.3 (2010), 1098–1102.

[157] L. H. Hess, M. Jansen, V. Maybeck, M. V. Hauf, M. Seifert, M. Stutzmann, I. D. Sharp, A. Offenhäusser, and J. A. Garrido. "Graphene Transistor Arrays for Recording Action Potentials from Electrogenic Cells." In: *Advanced Materials* 23.43 (2011), 5045–5049.

[158] F. Veliev, Z. Han, D. Kalita, A. Briançon-Marjollet, V. Bouchiat, and C. Delacour. "Recording Spikes Activity in Cultured Hippocampal Neurons Using Flexible or Transparent Graphene Transistors." In: *Frontiers in neuroscience* 11 (2017), p. 466.

[159] B. M. Blaschke et al. "Mapping brain activity with flexible graphene micro-transistors." In: *2D Materials* 4.2 (2017), p. 025040.

[160] C. Hébert et al. "Flexible Graphene Solution-Gated Field-Effect Transistors: Efficient Transducers for Micro-Electrocorticography." In: *Advanced Functional Materials* 453 (2017), p. 1703976.

[161] L. H. Hess, A. Lyuleeva, B. M. Blaschke, M. Sachsenhauser, M. Seifert, J. A. Garrido, and F. Deubel. "Graphene Transistors with Multifunctional Polymer Brushes for Biosensing Applications." In: *ACS Applied Materials & Interfaces* 6.12 (2014), 9705–9710.

[162] J. Ping, R. Vishnubhotla, A. Vrudhula, and A. T. C. Johnson. "Scalable Production of High-Sensitivity, Label-Free DNA Biosensors Based on Back-Gated Graphene Field Effect Transistors." In: *ACS Nano* 10.9 (2016), 8700–8704.

[163] N. Gao, T. Gao, X. Yang, X. Dai, W. Zhou, A. Zhang, and C. M. Lieber. "Specific detection of biomolecules in physiological solutions using graphene transistor biosensors." In: *Proceedings of the National Academy of Sciences of the United States of America* 113.51 (2016), 14633–14638.

[164] P. S. Cremer and S. G. Boxer. "Formation and Spreading of Lipid Bilayers on Planar Glass Supports." In: *The Journal of Physical Chemistry B* 103.13 (1999), 2554–2559.

[165] L. H. Klausen, T. Fuhs, and M. Dong. "Mapping surface charge density of lipid bilayers by quantitative surface conductivity microscopy." In: *Nature Communications* 7 (2016), p. 12447.

[166] G. Cevc. "Membrane electrostatics." In: *Biochimica et biophysica acta* 1031.3 (1990), 311–382.

[167] N.-J. Cho, L. Y. Hwang, J. J. R. Solandt, and C. W. Frank. "Comparison of Extruded and Sonicated Vesicles for Planar Bilayer Self-Assembly." In: *Materials (Basel, Switzerland)* 6.8 (2013), 3294–3308.

[168] A. V. Vlassov, S. Magdaleno, R. Setterquist, and R. Conrad. "Exosomes: Current knowledge of their composition, biological functions, and diagnostic and therapeutic potentials." In: *Biochimica et biophysica acta* 1820.7 (2012), 940–948.

[169] S. A. Melo et al. "Glypican-1 identifies cancer exosomes and detects early pancreatic cancer." In: *Nature* 523.7559 (2015), 177–182.

[170] R. Merkel, N. Kirchgeßner, C. M. Cesa, and B. Hoffmann. "Cell force microscopy on elastic layers of finite thickness." In: *Biophysical journal* 93.9 (2007), pp. 3314–3323.

[171] A.-S. Smith, K. Sengupta, S. Goennenwein, U. Seifert, and E. Sackmann. "Force-induced growth of adhesion domains is controlled by receptor mobility." In: *Proceedings of the National Academy of Sciences* 105.19 (2008), pp. 6906–6911.

[172] Z. Guttenberg, A. Bausch, B. Hu, R. Bruinsma, L. Moroder, and E. Sackmann. "Measuring ligand- receptor unbinding forces with magnetic beads: molecular leverage." In: *Langmuir* 16.23 (2000), pp. 8984–8993.

[173] G. Wiegand, K. R. Neumaier, and E. Sackmann. "Microinterferometry: three-dimensional reconstruction of surface microtopography for thin-film and wetting studies by reflection interference contrast microscopy (RICM)." In: *Applied optics* 37.29 (1998), pp. 6892–6905.

[174] G. Fragneto-Cusani. "Neutron reflectivity at the solid/liquid interface: examples of applications in biophysics." In: *Journal of Physics: Condensed Matter* 13.21 (2001), p. 4973.

[175] A. Junghans, E. B. Watkins, R. D. Barker, S. Singh, M. J. Waltman, H. L. Smith, L. Pocivavsek, and J. Majewski. "Analysis of biosurfaces by neutron reflectometry: From simple to complex interfaces." In: *Biointerphases* 10.1 (2015), p. 019014.

[176] J.-F. Moulin and M. Haese. "REFSANS: Reflectometer and evanescent wave small angle neutron spectrometer." In: *Journal of large-scale research facilities JLSRF* 1 (2015), p. 9.

[177] S. Mattauch, A. Koutsioubas, and S. Pütter. "MARIA: Magnetic reflectometer with high incident angle." In: *Journal of large-scale research facilities JLSRF* 1 (2015), p. 8.

[178] R. Cubitt and G. Fragneto. "D17: the new reflectometer at the ILL." In: *Applied Physics A* 74.1 (2002), s329–s331.

[179] A. Puliafito, L. Hufnagel, P. Neveu, S. Streichan, A. Sigal, D. K. Fygenson, and B. I. Shraiman. "Collective and single cell behavior in epithelial contact inhibition." In: *Proceedings of the National Academy of Sciences* 109.3 (2012), pp. 739–744.

[180] H. L. Smith, J. Hickey, M. S. Jablin, A. Trujillo, J. P. Freyer, and J. Majewski. "Mouse fibroblast cell adhesion studied by neutron reflectometry." In: *Biophys. J.* 98.5 (2010), pp. 793–9.

[181] J. Daillant and G. Gibaud. *X-ray and neutron reflectivity : principles and applications*. Springer.

[182] Y. Efimova, A. Van Well, U. Hanefeld, B. Wierczinski, and W. Bouwman. "On the neutron scattering length density of proteins in H2O/D2O." In: *Physica B: Condensed Matter* 350.1-3 (2004), E877–E880.

[183] Y. Gerelli, L. Porcar, and G. Fragneto. "Lipid Rearrangement in DSPC/DMPC Bilayers: A Neutron Reflectometry Study." In: *Langmuir* 28.45 (2012), pp. 15922–15928.

[184] M. Huth, S. Hertrich, G. Mezo, E. Madarasz, and B. Nickel. "Neural Stem Cell Spreading on Lipid Based Artificial Cell Surfaces, Characterized by Combined X-ray and Neutron Reflectometry." In: *Materials* 3.11 (2010), pp. 4994–5006.

[185] F. Rehfeldt, R. Steitz, S. P. Armes, R. von Klitzing, A. P. Gast, and M. Tanaka. "Reversible Activation of Diblock Copolymer Monolayers at the Interface by pH Modulation, 2:- Membrane Interactions at the Solid/Liquid Interface." In: *The Journal of Physical Chemistry B* 110.18 (2006), pp. 9177–9182.

[186] H. L. Smith, M. S. Jablin, A. Vidyasagar, J. Saiz, E. Watkins, R. Toomey, A. J. Hurd, and J. Majewski. "Model lipid membranes on a tunable polymer cushion." In: *Physical review letters* 102.22 (2009), p. 228102.

[187] A. Ozcan and E. McLeod. "Lensless imaging and sensing." In: *Annual review of biomedical engineering* 18 (2016), pp. 77–102.

[188] T. Pärr. "In Situ Timelapse Reconstruction-Free Monitoring of Confluence with a Lensfree, Ultra Small, Low Cost Microscopic Setup." Master Thesis. 2016.

[189] F. Heinrich and M. Lösche. "Zooming in on disordered systems: Neutron reflection studies of proteins associated with fluid membranes." In: *Biochimica et Biophysica Acta (BBA) - Biomembranes* 1838.9 (2014), pp. 2341–2349.

[190] R. C. MacDonald, R. I. MacDonald, B. P. M. Menco, K. Takeshita, N. K. Subbarao, and L.-r. Hu. "Small-volume extrusion apparatus for preparation of large, unilamellar vesicles." In: *Biochimica et Biophysica Acta (BBA) - Biomembranes* 1061.2 (1991), 297–303.

[191] F. S. Cohen, M. H. Akabas, and A. Finkelstein. "Osmotic swelling of phospholipid vesicles causes them to fuse with a planar phospholipid bilayer membrane." In: *Science* (1982), 458–460.

[192] L. H. Hess. "Graphene Transistors for Biosensing and Bioelectronics." Dissertation. 2014.

[193] A. Härtl, J. A. Garrido, S. Nowy, R. Zimmermann, C. Werner, D. Horinek, R. Netz, and M. Stutzmann. "The Ion Sensitivity of Surface Conductive Single Crystalline Diamond." In: *Journal of the American Chemical Society* 129.5 (2007), pp. 1287–1292.

[194] I. Heller, S. Chatoor, J. Männik, M. A. G. Zevenbergen, C. Dekker, and S. G. Lemay. "Influence of Electrolyte Composition on Liquid-Gated Carbon Nanotube and Graphene Transistors." In: *Journal of the American Chemical Society* 132.48 (2010), pp. 17149–17156.

DANKSAGUNG

Bert Nickel, ich danke Dir für die Betreuung meiner Promotion und deine Unterstützung in diesen sehr lehrreichen Jahren! Ich denke gerne zurück an fröhliche Gruppenbesprechungen, Strahlzeiten, in denen auch um drei Uhr nachts noch herzlich gelacht wurde und gemeinsame Bemühungen, das Drehzentrum zu finden!

Joachim Rädler, ich habe so viele Jahre an deinem Lehrstuhl verbracht und deine lockere und herzliche Art ist sicher ein Hauptgrund dafür, dass die Stimmung hier so toll ist! Auch möchte ich Dir für die wichtige Unterstützung im Zell-Projekt danken.

Herr Sackmann, ich habe die Zusammenarbeit mit Ihnen sehr genossen! Sie sind nicht nur fachlich, sondern vor allem menschlich ein Vorbild und eine Inspiration.

Jan Lipfert, danke, dass Du die Zweitbetreuung meiner Arbeit übernommen hast. Deine Unterstützung und deine positiven Impulse in den richtigen Momenten haben mir immer ein gutes Gefühl und Sicherheit vermittelt.

Viele Leute waren an meinen Projekten beteiligt. Für die wunderbare Graphen-Kooperation und die interessanten Diskussionen möchte ich mich herzlich bei Benno Blaschke (gerne denke ich an die Datenschutzdiskussionen auf der Bank bei einem Espresso) und Jose Garrido bedanken. Gregor Cevc, Sie haben mir Ihren wertvollen Tipps und Ihrer Hilfsbereitschaft viel zu meinem Verständnis von Lipiden beigetragen! Ohne Alexandros Koutsioumpas und Jean-François Moulin mit seinem Team wäre die Durchführung der Neutronenmessungen nicht möglich gewesen. Danke für Eure Unterstützung! Josi Hirte, Tobi Pärr und Philipp Paulitschke, danke für die Kooperation und Unterstützung, oft in letzter Sekunde, beim Ausstatten der Messkammern mit dem Holographie-Mikroskop. Philipp, Dir auch vielen Dank für die vielen Ratschläge! Der Werkstatt, vor allem Christian Neubert und Andi Krill, möchte ich für die sofortige Anfertigung jedes dringenden Sonderwunsches danken und Stephan Manus, der immer für alles die Lösung parat hat und uns vor starken Stromschlägen bewahrt, für seine Unterstützung und die vielen interessanten und lehrreichen Gespräche. Gerlinde Schwake, Charlott Leu, Susi Kempter und Philipp Altpeter, man will sich nicht vorstellen, wie es ohne eure Kompetenz, Geduld und Hilfsbereitschaft ausschauen würde! Margarete Meixner, Margarita Rüter-Stimpfl, Mandy Häusler und Mar-

tina Edenhofer möchte ich für die herzliche und exzellente Beratung danken, die einen das Sekretariat immer mit einem Lächeln verlassen lässt.

Den Kollegen vom Lehrstuhl Gaub, der Ag Lipfert und Ag Braun vielen Dank für das Weiterhelfen bei vielen Problemen und letzteren natürlich auch für den guten Espresso aus der güldenen Maschine!

Dem Center for NanoScience (CeNS) und dem Exzellenzcluster Nanosystems Initiative Munich (NIM) danke ich für das breite Angebot für wissenschaftlichen Austausch - vor allem die Konferenz in Venedig war so schön! Ein herzliches Dankeschön stellvertretend an Susanne Hennig, Claudia Leonhardt und Peter Sonntag für die Koordination. Christoph Hohmann, Dir vielen Dank für deine tollen Graphiken!

Simon Noever! Die unendliche und liebevolle Geduld, mit der Du mich an deinem Wissen teilhaben hast lassen, macht mich immer noch sprachlos. Du hast mir den Einstieg ins Streubusiness so angenehm und einfach gemacht, wie er nur sein kann! Du bist ein Vorbild und Freund und ich verdanke Dir so viel!

Stefan F. Fischer, es war ein großes Glück für mich, dass wir einen Großteil der Zeit meiner Promotion Kollegen waren. Danke, dass Du so oft deine Noise-Cancelling-Kopfhörer abgenommen hast, um mir exzellente Ratschläge zu erteilen, für deine Programme und Macros, die vielen Kaffeepausen und die Lockerheit, die du vermittelst. Du bist in meinen Stullenkreis aufgenommen!

Ida, für deine wichtige Unterstützung und Einführung in die Welt der Neutronen vielen, vielen tack!

Janina! Danke, dass Du immer ein offenes Ohr für meine Sorgen und Fragen hast! Die unzähligen geschälten Orangen und all die Karotten haben mir jeden Tag im Büro versüßt und mich vor Hungerlöchern und Vitaminmangel bewahrt. Außerdem möchte ich Dir als Hauptverantwortliche für meinen geschärften Blick, meine Beweglichkeit und dafür, dass ich (fast) einen Handstand kann, danken!

Danke an das coolste und gesündeste Büro von allen – Simone, Alex, Ricarda, Amelie und Janina und den verflossenen Ellie, Sonja und Felix! Die gute und lustige Stimmung hier lässt einen jeden Tag gerne in die Arbeit kommen!

Ein großer Dank geht an meine Arbeitsgruppe mit Clemens Liewald, Janina Römer, Tina Ober, Cornelia Sattler, Dimitri Berger, Henrik

Hecht und Jasmin Moazzami-Fallah für die tolle Atmosphäre und die Hilfsbereitschaft! Auch möchte ich wirklich allen an unserem Lehrstuhl, angefangen bei den Grandes-Dames Caro, Svenja, Sonja, Tina, Verena und Samira, danken! Die Stimmung hier ist wirklich einzigartig, es wird einem immer sofort geholfen und man kann auf die Unterstützung von jedem zählen.

Sonja, Tina, Zhenya, Matthias, Lorenz, Manu – mit Euch als Kollegen ist sichergestellt, dass man körperlich fit bleibt! Felix, danke für die Motivation zum Klimmzugtraining.

Heinrich Grabmayr, Robert Grummt und Jo Wöhrstein, vielen Dank für Eure Unterstützung und die Möglichkeit, bei DEOXY mit dabei zu sein! Was ich zusammen mit Euch, Philipp Nickels, Ryan Sherrad, Nora Kassner und Kevin Kaiser bereits erlebt habe, macht die Vorfreude auf das, was jetzt kommt, nur noch größer!

Kathi, Alexandra, Ricarda, David, Jürgen, Timon, Amelie, Tina und Gerlinde! Wie gerne erinnere ich mich an gemeinsame Unternehmungen zurück! Ich hoffe, es bietet sich noch oft Gelegenheit, mit Euch durch die Welt zu strawanzeln!

Linda und Franzi, wenn man Euch hinter sich weiß, muss man sich wirklich vor nichts und niemandem fürchten! Danke!

Janina, Stefan, Tina, Oberlehrer Winterl und natürlich meinem Bro, Euch einen herzlichen Dank fürs Korrekturlesen!

Uli und Flo, bei allen wissenschaftlichen Erkenntnissen und Errungenschaften - Eure Freundschaft ist mit Abstand der größte Gewinn des Projekts Physik!

Ein großer Dank an all meine Freunde, die immer für mich da sind und das Leben so lebenswert machen! Schoeppe, danke fürs zur Hand gehen im Reaktor sogar um Mitternacht. Jensen, deine Unterstützung und das Selbstbewusstsein im richtigen Moment waren wichtig! Prof. Aurel, die interessante Abwechslung und die tiefgreifenden Diskussionen beim Businesslunch habe ich immer sehr genossen! Liebste Danielli, danke für alles die ganze Zeit!!!

Cara Sandra, grazie per il grande sostegno, il quale ha reso tutto molto più facile e più bello!

Meiner tollen Familie ohne die überhauptsnix möglich wäre!